

SOLIDIFICATION OF HOT-DIP GALVANIZED COATINGS

SOLIDIFICATION OF HOT-DIP GALVANIZED COATINGS

By
Shirin Kaboli

A Thesis
Submitted to the School of Graduate Studies
In Partial Fulfilment of the Requirements
For the Degree of
Master of Applied Science

McMaster University

© Copyright by Shirin Kaboli, August 2010

MASTER OF APPLIED SCIENCE (2010)
(Materials Science and Engineering)

McMaster University
Hamilton, Ontario

TITLE: Solidification of Hot-Dip Galvanized Coatings

AUTHOR: Shirin Kaboli, B. E. (University of Tehran)

SUPERVISOR: Dr. Joseph. R. McDermid

NUMBER OF PAGES: xvii, 159

ABSTRACT

Continuous hot-dip galvanizing is a common industrial process in which a steel sheet is immersed in a molten zinc alloy bath. After solidification, a thin zinc-rich layer is formed on the steel surface which protects the substrate in corrosive environments. Small amounts of antimony are sometimes added to the galvanizing bath to reduce zinc viscosity and ease the gas jet wiping operation. One of the side effects of antimony addition to the zinc alloy bath is the formation of very large zinc grains. One of the problems associated with coatings containing large zinc grains are relatively poor paint adhesion and detrimental mechanical properties. In this study, a galvanizing simulator was used to investigate the influence of important process variables such as bath composition, steel surface roughness and cooling conditions on the solidification of zinc coatings. The coating surface and cross-sectional microstructures were characterized via optical microscopy and Scanning Electron Microscopy (SEM). In addition, the zinc grain orientation distribution was investigated using Electron Backscattered Diffraction (EBSD). Furthermore, Scanning Auger Microscopy (SAM) was carried out on the coating surface to study the distribution of alloying elements and bath impurities in intermetallic phases. The results showed that the presence of small amounts of antimony in the zinc alloy bath enhanced the grain growth in preferred crystallographic orientations on both substrates. It was also found that the substrate surface roughness had a strong influence on the coating crystallographic texture such that zinc grains had a strong basal preferred orientation on smooth substrates while exhibiting prismatic or pyramidal orientations on

rough substrates. Finally, zinc crystals were smaller for the slow-cooled coatings while zinc grains had almost the same diameter for the intermediate and fast-cooled coatings on both the smooth and rough substrates. Factors affecting the solidified microstructure, crystallographic orientation of zinc grains and phase assemblage will be discussed.

Acknowledgements

The completion of the following M. A. Sc. thesis would not have been possible without the collaboration of great number of people both within and outside of the department of Materials Science and Engineering at McMaster University. It is a pleasure to convey my gratitude to all of them herein.

First and foremost, I would like to express my sincere gratitude to my supervisor Dr. Joseph R. McDermid to whom I owe the two years of scientific as well as personal improvement. His scientific guidance, support, contribution and persistent patience through every stage of the present research are gratefully appreciated. I would like to acknowledge him for offering me the trust and liberty in conducting parts of this project on my own which has facilitated many invaluable experiences during the course of this study.

I would like to thank Dr. Sumanth Shankar, Professor Nikolas Provatas and Dr. Jeff Hoyt for their constructive involvement and comments on the problems I faced during this research. I have been inspired by their suggestions, encouragement and guidance without which this thesis would not have been successfully completed.

I would also like to acknowledge John Thomson and Marianna Budiman for helping me to perform the hot-dip galvanizing experiments at Teck Cominco Company. My gratitude is also extended to Dr. Jim Britten and Victoria Jarvis at X-ray laboratory, Chris Butcher, Steve Koprach and other staff at Canadian Center for Electron Microscopy

(CCEM), John Rodda and Doug Culley at Materials laboratories, Jim McLaren, JP Talon and Mark MacKenzie at mechanical machine shop and finally Dimitri Karpuzov as well as Shihong Xu at Scanning Auger Microscopy (SAM) laboratory at the University of Alberta for their technical and instrumental assistance.

I am also much indebted to Erika Bellhouse, Kavitha Ranganathan, Samaneh Alibeigi and other members of my research group who provided friendly and scientifically productive atmosphere for my research as well as valuable support and assistance.

My special gratitude goes to Shahrzad Hosseini, Nooshin Tajik, Sherri Hadian and the rest of my friends who have always supported me in every possible way. Their precious friendship and kindness will forever be remembered in my heart.

My parents and brothers deserve my deepest appreciation for their on-going support throughout my life. Particularly, I would like to thank my younger brother, Reza Kaboli, for his encouragement, scientific guidance and helpful suggestions throughout this project.

Finally, I would like to thank US Steel Canada, Xstrata Zinc, the Natural Sciences and Engineering Research Council of Canada (NSERC) and the members of the McMaster Steel Research Center for their financial support.

TABLE OF CONTENTS

CHAPTER 1. INTRODUCTION	1
CHAPTER 2. LITERATURE REVIEW	6
2.1. Spangle Description	6
2.2. Spangle Formation	7
2.3. Spangle Morphology	13
2.4. Spangle Shape and Crystallography	17
2.5. Spangle Reflectivity and Roughness	22
2.6. Spangle Nucleation and Growth Mechanisms	23
2.7. Effect of Process Variables on Spangles Size	26
2.8. Coating Crystallographic Texture	29
2.9. Effects of Antimony on Zinc Coatings	32
2.10. Intermetallic Compounds	33
2.11. Depressions and Cracks	35
CHAPTER 3. EXPERIMENTAL PROCEDURE	37
3.1. Materials	37
3.2. McMaster Galvanizing Simulator	39
3.3. Coating Weight	42
3.4. Surface Roughness Measurements	42
3.5. Metallography	43
3.5.1. Coating Surfaces	43

3.5.2. Coating Cross-sections	44
3.6. Characterization Techniques.....	45
3.7. Grain Size Measurements	46
CHAPTER 4. RESULTS	47
4.1. 0 wt% Sb Alloy	47
4.1.1. Coating Surface Microstructure.....	47
4.1.2. Coating Cross-section Microstructure	51
4.1.3. Coating Intermetallics.....	56
4.1.4. Coating Crystallographic Texture	60
4.2. 0.01 wt% Sb Alloy	66
4.2.1. Coating Surface Microstructure.....	66
4.2.2. Coating Cross-section Microstructure	72
4.2.3. Coating Intermetallics.....	75
4.2.4. Coating Crystallographic Texture	83
4.3. 0.03 wt% Sb Alloy	90
4.3.1. Coating Surface Microstructure.....	90
4.3.2. Coating Cross-section Microstructure	95
4.3.3. Coating Intermetallics.....	96
4.3.4. Coating Crystallographic Texture	100
4.4. 0.1 wt% Sb Alloy	106
4.4.1. Coating Surface Microstructure.....	106
4.4.2. Coating Cross-section Microstructure	110

4.4.3. Coating Intermetallics.....	110
4.4.4. Coating Crystallographic Texture	118
4.5. 0.2 wt% Sb Alloy	123
4.5.1. Coating Surface Microstructure.....	123
4.5.2. Coating Cross-section Microstructure	127
4.5.3. Coating Intermetallics.....	127
CHAPTER 5. DISCUSSION.....	128
5.1. Spangle Formation	128
5.2. Spangle Morphology and Appearance.....	131
5.3. Microstructural and Crystallographic Texture Evolution	134
5.4. Zinc Grain Size	140
5.5. Coating Intermetallic Phases.....	144
CHAPTER 6. CONCLUSIONS	146
REFERENCES	148
APPENDIX A.....	157

LIST OF FIGURES

CHAPTER 1.

Figure 1-1. Schematic of a typical continuous hot-dip galvanizing line (CGL) [Marder 2000] 2

Figure 1-2. Optical micrograph of the surface finish of a typical galvanized coating containing small amount of Pb [Marder 2000] 4

CHAPTER 2.

Figure 2-1. Optical micrograph of a typical zinc spangle on the surface of galvanized coating containing 0.2 wt% Pb [Fasoyinu 1990] 6

Figure 2-2. Schematic illustration of the solidification sequence for lead containing zinc layers: (a) rapid lateral expansion, (b) slow thickening process, (c) emergence of shiny sectors, and (d) eutectic Zn-Pb solidification [Strutzenberger 1998] 12

Figure 2-3. Optical micrograph of typical surface finish of galvanized steel exhibiting shiny, feathery, dimpled, ridged, orthogonal dendritic regions [Strutzenberger 1998] 13

Figure 2-4. Scanning electron microscopic (SEM) surface image of (a) shiny (b) feathery area [Strutzenberger 1998] 15

Figure 2-5. SEM surface image of (a) dimpled (b) ridged area [Strutzenberger 1998] 16

Figure 2-6. SEM surface image of orthogonal dendritic area [Strutzenberger 1998] 17

Figure 2-7. The plot of α as a function of β [Jin-Tang 2007] 18

Figure 2-8. (a) Optical micrograph of a hexagonal spangle (b) schematic of crystal orientation [Strutzenberger 1998] [Jin-Tang 2007] 19

Figure 2-9. (a) Optical micrograph of an octagon spangle (b) schematic of crystal orientation [Strutzenberger 1998] [Jin-Tang 2007] 20

Figure 2-10. (a) Optical micrograph of a rhombus spangle (b) schematic of crystal orientation [Strutzenberger 1998] [Jin-Tang 2007] 21

Figure 2-11. Zinc grain size as a function of solute concentration [Fasoyinu 1990] 28

Figure 2-12. ODG and texture of zinc coating compared to random distribution as a function of the inclination angle of the basal plane [Semoroz 2002-1] 30

Figure 2-13. (a) Texture coefficient as a function of Sb or (b) Pb content of galvanizing bath [Asgari 2007] 33

CHAPTER 3.

Figure 3-1. Coated steel panel 40

Figure 3-2. (a) Image and (b) schematic of McMaster Galvanizing Simulator (MGS)..... 41

Figure 3-3. Heat treatment cycle for dipping experiments 41

Figure 3-4. Surface roughness maps taken from (a) BR and (b) HR as-annealed steel..... 43

Figure 3-5. 3D model of surface roughness for (a) BR and (b) HR as-annealed steel 43

CHAPTER 4.

Figure 4-1. Optical micrographs of the as-cast coating surface containing 0 wt% Sb on BR steel cooled at (a) 10 °C/s (b) 1 °C/s (c) 0.1 °C/s and on HR steel cooled at (d) 10 °C/s (e) 1 °C/s (f) 0.1 °C/s 49

Figure 4-2. Optical micrographs of a single zinc grain on a coated (a) BR and (b) HR steel cooled at 0.1 °C/s 50

Figure 4-3. SEM-SEIs of the grain boundary openings on a coated (a) BR and (b) HR steel cooled at 10 °C/s..... 50

Figure 4-4. Grain size vs. cooling rate for the BR and HR steels..... 50

Figure 4-5. Optical micrograph of the coating cross-section on a BR steel substrate cooled at 10 °C/s..... 52

Figure 4-6. (a) SEM-SEI (b) Euler orientation colour map (c) pole figures and (d) {0002} pole plot of the coating cross-section on a BR steel substrate cooled at 10 °C/s 53

Figure 4-7. Al content as a function of coating thickness for coated BR steel substrate cooled at 10 °C/s 54

Figure 4-8. Optical micrograph of the coating cross-section on a HR steel substrate cooled at 10 °C/s..... 56

Figure 4-9. Al content as a function of coating thickness for coated HR steel substrate cooled at 10 °C/s 56

Figure 4-10. SEM-BEI of the coating surface on (a-b) BR and (c-d) HR steel substrate cooled at 0.1 °C/s 57

Figure 4-11. (a) SEM-SEI of the coated BR steel surface cooled at 0.1 °C/s containing round particles and (b) Zn (c) Fe and (d) Al SAM maps 59

Figure 4-12. (a) SEM-SEI of the coated BR steel surface cooled at 0.1 °C/s containing star-like particle and (b) Zn (c) Fe and (d) Al SAM maps..... 59

Figure 4-13. (a) Microstructural map (b) Euler orientation colour map (c) pole figures and (d) {0002} pole plot of a cooled BR substrate cooled at 10 °C/s 62

Figure 4-14. (a) Microstructural map (b) Euler orientation colour map (c) pole figures and (d) {0002} pole plot of a cooled BR substrate cooled at 0.1 °C/s 63

Figure 4-15. (a) Microstructural map (b) Euler orientation colour map (c) pole figures and (d) {0002} pole plot of a cooled HR substrate cooled at 10 °C/s..... 64

Figure 4-16. (a) Microstructural map (b) Euler orientation colour map (c) pole figures and (d) {0002} pole plot of a cooled HR substrate cooled at 0.1 °C/s..... 65

Figure 4-17. Low magnification optical micrographs of the as-cast coating surface containing 0.01 wt% Sb on BR steel cooled at (a) 10 °C/s (b) 1 °C/s (c) 0.1 °C/s and on HR steel cooled at (d) 10 °C/s (e) 1 °C/s (f) 0.1 °C/s 68

Figure 4-18. High magnification optical micrographs of the as-cast coating surface containing 0.01 wt% Sb on BR steel cooled at (a) 10 °C/s (b) 1 °C/s (c) 0.1 °C/s and on HR steel cooled at (d) 10 °C/s (e) 1 °C/s (f) 0.1 °C/s 69

Figure 4-19. Optical micrographs of the (a) shiny (b) dimpled (c) feathery (d) ridged and (e) orthogonal-dendritic morphologies on coated BR steel cooled at 0.1 °C/s..... 70

Figure 4-20. Optical micrographs of (a) bright and (b-c) dark regions on BR steel cooled at 0.1 °C/s..... 71

Figure 4-21. Grain size vs. cooling rate for the BR and HR steels..... 71

Figure 4-22. Optical micrograph of the coating cross-section on a BR substrate cooled at 10 °C/s..... 73

Figure 4-23. Al content as a function of coating thickness for coated HR steel substrate cooled at 10 °C/s 73

Figure 4-24. Optical micrograph of a coating cross-section cooled at 0.1 °C/s cooling rate on a BR substrate 73

Figure 4-25. Optical micrograph of a coating cross-section on a HR steel substrate cooled at 10 °C/s..... 74

Figure 4-26. SEM-BEIs of the intermetallics on (a) dendritic (b) grain boundary and (c-d) non-dendritic regions on coated BR steel cooled at 0.1 °C/s..... 76

Figure 4-27. SEM-BEIs of (a) light grey (b) white (c) dark grey and (d) black particles on the BR steel cooled at 0.1 °C/s..... 77

Figure 4-28. (a) SEM-SEI of a coated BR steel cooled at 0.1 °C/s containing an irregular particle and (b) Zn (c) Al and (d) Sb SAM maps (e-f) auger colour overlay images 79

Figure 4-29. (a) SEM-SEI of the coated BR steel cooled at 0.1 °C/s containing a star-like particle and (b) Zn (c) Sn (d) Fe (e) Cr (f) Al and (g) Pb SAM maps 80

Figure 4-30. (a) SEM-SEI of a coated BR steel cooled at 0.1 °C/s containing a Chinese-script particle and (b) Zn (c) Fe (d) Al and (e) Cr SAM maps 81

Figure 4-31. (a) TEM-dark field image of the white intermetallic particle and the corresponding (b) diffraction pattern 82

Figure 4-32. (a) Simulated {001} diffraction pattern (b) solution for the obtained diffraction pattern..... 83

Figure 4-33. (a) Microstructural map (b) Euler orientation colour map (c) pole figures and (d) {0002} pole plot of coating surface on BR steel cooled at 10 °C/s 85

Figure 4-34. (a) Microstructural map (b) Euler orientation colour map (c) pole figures and (d) {0002} pole plot of coating surface on BR steel cooled at 0.1 °C/s 86

Figure 4-35. (a) Microstructural map (b) Euler orientation colour map (c) pole figures and (d) {0002} pole plot of coating surface on HR steel cooled at 10 °C/s..... 87

Figure 4-36. (a) Microstructural map (b) Euler orientation colour map (c) pole figures and (d) {0002} pole plot of coating surface on HR steel cooled at 0.1 °C/s..... 88

Figure 4-37. (a) SEM-SEI (b) Euler orientation colour map and (c) pole figures of zinc grains on coated BR steel substrate cooled at 0.1 °C/s 89

Figure 4-38. Low magnification optical micrographs of the as-cast coating surface containing 0.03 wt% Sb on BR steel cooled at (a) 10 °C/s (b) 1 °C/s (c) 0.1 °C/s and on HR steel cooled at (d) 10 °C/s (e) 1 °C/s (f) 0.1 °C/s 92

Figure 4-39. High magnification optical micrographs of the as-cast coating surface containing 0.03 wt% Sb on BR steel cooled at (a) 10 °C/s (b) 1 °C/s (c) 0.1 °C/s and on HR steel cooled at (d) 10 °C/s (e) 1 °C/s (f) 0.1 °C/s 93

Figure 4-40. Optical micrographs of the (a) shiny (b) semi-shiny spangles on a coated BR surface and (c) semi-shiny (d) dull grains on a coated HR surface cooled at 10 °C/s..... 94

Figure 4-41. Grain size vs. cooling rate for the BR and HR steels..... 94

Figure 4-42. Optical micrographs of the coating cross-section at 10 °C/s cooling rate on (a) BR and (b) HR steel substrate 95

Figure 4-43. SEM-BEIs of the coating microstructure in the (a) dendritic (b) grain boundary and (c-d) non-dendritic region on coated BR steel cooled at 0.1 °C/s..... 97

Figure 4-44. (a) SEM-SEI of a coated BR surface cooled at 0.1 °C/s containing elongated particles and (b) Sb (c) Zn and (d) Al SAM maps 98

Figure 4-45. (a) SEM-SEI of the coated BR steel surface cooled at 0.1 °C/s containing round particles and (b) Zn (c) Cr (d) Pb (e) Sn (f) Fe and (g) Al SAM maps 99

Figure 4-46. (a) Microstructural map (b) Euler orientation colour map (c) pole figures and (d) {0002} pole plot of a coating on a BR steel cooled at 10 °C/s 102

Figure 4-47. (a) Microstructural map (b) Euler orientation colour map (c) pole figures and (d) {0002} pole plot of a coating surface on a BR steel cooled at 0.1 °C/s..... 103

Figure 4-48. (a) Microstructural map (b) Euler orientation colour map (c) pole figures and (d) {0002} pole plot of a coating surface section on a HR steel cooled at 10 °C/s 104

Figure 4-49. (a) Microstructural map (b) Euler orientation colour map (c) pole figures and (d) {0002} pole plot of a coating surface on a HR steel cooled at 0.1 °C/s 105

Figure 4-50. Low magnification optical micrographs of the as-cast coating surface containing 0.1 wt% Sb on BR steel cooled at (a) 10 °C/s (b) 1 °C/s (c) 0.1 °C/s and on HR steel cooled at (d) 10 °C/s (e) 1 °C/s (f) 0.1 °C/s..... 107

Figure 4-51. Optical micrographs of the as-cast coating surface containing 0.1 wt% Sb on BR steel cooled at (a) 10 °C/s (b) 1 °C/s (c) 0.1 °C/s and on HR steel cooled at (d) 10 °C/s (e) 1 °C/s (f) 0.1 °C/s 108

Figure 4-52. High magnification optical micrographs of the (a) dendritic and (b) non-dendritic regions on a coated BR steel cooled at 10 °C/s 109

Figure 4-53. Grain size vs. cooling rate for BR and HR steels..... 109

Figure 4-54. SEM-BEIs of the intermetallics on (a) dendritic (b) grain boundary and (c-d) non-dendritic regions on a coated BR steel cooled at 0.1 °C/s..... 111

Figure 4-55. (a) SEM-SEI of the shiny and dull regions on a coated BR steel surface cooled at 0.1 °C/s and (b) Zn (c) Al (d) Sb SAM maps and (e) Auger colour overlay image..... 113

Figure 4-56. (a-b) SEM-SEI of the shiny and dull regions on the sputtered coated BR steel surface cooled at 0.1 °C/s (c) Zn (d) Al (e) Sb and (f) Sn SAM maps 114

Figure 4-56. (Cont'd) (g-i) Auger colour overlay images 115

Figure 4-57. (a-d) SEM-SEIs of a precipitate (e) Zn and (f) Al SAM maps 116

Figure 4-57. (Cont'd) (g) Sb (h) Sn SAM maps and (i-j) Auger colour overlay images..... 117

Figure 4-58. (a-b) SEM-SEIs of a particle in a shiny region (c) Sn (d) Pb SAM maps and (e-f) Auger colour overlay images..... 118

Figure 4-59. (a) Microstructural map (b) Euler orientation colour map (c) pole figures and (d) {0002} pole plot of a coating surface section on a BR steel cooled at 10 °C/s 119

Figure 4-60. (a) Microstructural map (b) Euler orientation colour map (c) pole figures and (d) {0002} pole plot of a coating surface section on a BR steel cooled at 0.1 °C/s 120

Figure 4-61. (a) Microstructural map (b) Euler orientation colour map (c) pole figures and (d) {0002} pole plot of a coating surface section on a HR steel cooled at 10 °C/s 121

Figure 4-62. (a) Microstructural map (b) Euler orientation colour map (c) pole figures and (d) {0002} pole plot of a coating surface section on a HR steel cooled at 0.1 °C/s 122

Figure 4-63. Low magnification optical micrographs of the as-cast coating surface containing 0.2 wt% Sb on a BR steel cooled at (a) 10 °C/s (b) 1 °C/s (c) 0.1 °C/s and on a HR steel cooled at (d) 10 °C/s (e) 1 °C/s (f) 0.1 °C/s 124

Figure 4-64. Optical micrographs of the (a) shiny (b) feathery (c) dimpled (d) ridged and (e) orthogonal-dendritic morphologies on a coated BR steel cooled at 10 °C/s..... 125

Figure 4-65. Optical micrographs of the (a) dendritic and (b) non-dendritic regions cooled at 10 °C/s on a coated BR steel 126

Figure 4-66. Grain size vs. cooling rate for the BR and HR steels..... 126

Figure 4-67. AlSb intermetallic particles on coated BR steel cooled at 0.1 °C/s 127

Figure 4-68. (a) SEM-SEI of a shiny region after sputtering on the coated BR steel surface cooled at 10 °C/s (b) Sb (c) Zn and (d) Al SAM maps 128

Figure 4-69. (a) SEM-SEIs of a dull region after sputtering on the coated BR steel surface cooled at 10 °C/s ((b) Zn (c) Al (d) Fe and (e) Sb SAM maps 129

CHAPTER 5.

Figure 5-1. Schematic illustration of the solidification sequence for lead containing zinc spangles: (a) rapid lateral expansion, (b) slow thickening process, (c) emergence of shiny sectors, and (d) eutectic Zn-Pb solidification [Strutzenberger 1998] 133

Figure 5-2. Schematic of the nucleation and growth conditions on (a) BR and (b) HR steel substrate at 0 wt% Sb 135

Figure 5-3. Melt surface energy and solute segregation vs. Sb content 137

Figure 5-4. $f(\{0002\})$ vs. steel surface roughness and melt surface energy for (a) 10 °C/s..... 138

Figure 5-4. (Cont'd) $f(\{0002\})$ vs. steel surface roughness and melt surface energy for (b) 0.1 °C/s cooling rate..... 139

Figure 5-5. $f(\{0002\})$ vs. cooling rate and surface energy for (a) BR..... 139

Figure 5-5. (Cont'd) $f(\{0002\})$ vs. cooling rate and surface energy for (b) HR steels.... 140

Figure 5-6. Zinc grain size vs. steel surface roughness and melt surface energy for coatings cooled at (a) 10 (b) 1 and (c) 0.1 °C/s 142

Figure 5-7. Zinc grain size vs. cooling rate and melt surface energy for coatings on (a) BR and (b) HR steels..... 143

Figure 5-8. Zn-Al-Fe-Sb phase diagram..... 145

LIST OF TABLES

CHAPTER 2.

Table 2-1. Estimated segregation coefficients and surface tension for binary alloys [Fasoyinu 1990]25

Table 2-2. Characteristics of zinc crystals in zinc coatings and bulk alloys [Semoroz 2002-1]31

CHAPTER 3.

Table 3-1. Experimental matrix for galvanizing experiments37

Table 3-2. Chemical analysis of the steel substrates (wt%).....38

Table 3-3. Chemical analysis of the zinc baths (wt%).....39

CHAPTER 4.

Table 4-1. SAM point analysis of the different phases on coated BR steel cooled at 0.1 °C/s (at%).....60

Table 4-2. Area percentage of basal zinc grains inclined for 0-15° relative to the steel sheet65

Table 4-3. SAM point analysis of the different phases on coated BR steel cooled at 0.1 °C/s (at%).....81

Table 4-4. Area percentage of basal zinc grains inclined for 0-15° relative to the steel sheet89

Table 4-5. SAM point analysis of the different phases on coated BR steel cooled at 0.1 °C/s (at%).....100

Table 4-6. Area percentage of basal zinc grains inclined for 0-15° relative to the steel sheet105

Table 4-7. Area percentage of basal zinc grains inclined for 0-15° relative to the steel sheet122

Table 4-8. SAM point analysis of the different phases on coated BR steel cooled at 0.1 °C/s (at%).....129

CHAPTER 1. INTRODUCTION

Low carbon steel sheets have been used commonly for exposed applications in the automotive and construction industries. One of the main limitations of these steel sheets is their low corrosion resistance in humid environments. Thus, the corrosion protection of steel sheet is necessary, particularly for the steel panels used in the automotive industry due to the presence of de-icing salts on motorways during winter [Leory 1988]. Steel products can effectively be protected by zinc coatings. Zinc coatings provide two types of protection for the steel substrate: (i) a physical barrier between the steel and the corrosive atmosphere environment and (ii) sacrificial anodic protection with respect to iron. There are a number of processes for coating steel products with a protective zinc layer such as thermal spraying, electrodeposition and hot-dip galvanizing. Among these methods, the continuous hot-dip galvanizing process has been considered to be a cost effective way of coating steel products in large quantities [Marder 2000].

The continuous hot-dip galvanizing process is basically immersion of steel sheets in a molten zinc bath to form a zinc-rich protective layer on the steel surface. Industrially, pre-fabricated steel articles are galvanized using the batch hot-dip galvanizing process while steel sheets, wires and tubes are galvanized in the continuous hot-dip galvanizing process. It has been reported that 65-70 % of the overall mass of the world zinc production is consumed in the continuous hot dip galvanizing of steel sheets [Zhang 2001].

A schematic of a typical continuous hot-dip galvanizing line (CGL) is illustrated in Figure 1-1. In general, the continuous hot-dip galvanizing process is comprised of the following steps [Marder 2000] [Umeda 1975].

- (1) Pre-treatments: The steel strip undergoes a number of cleaning steps where surface oxides and contaminations are removed to ensure good wetting of the strip in the liquid zinc bath.
- (2) Annealing: The clean steel strip is heated to an annealing temperature at which the strip is held isothermally for a defined time. The annealing temperature and time is determined such that the desired microstructure of the steel strip is obtained.

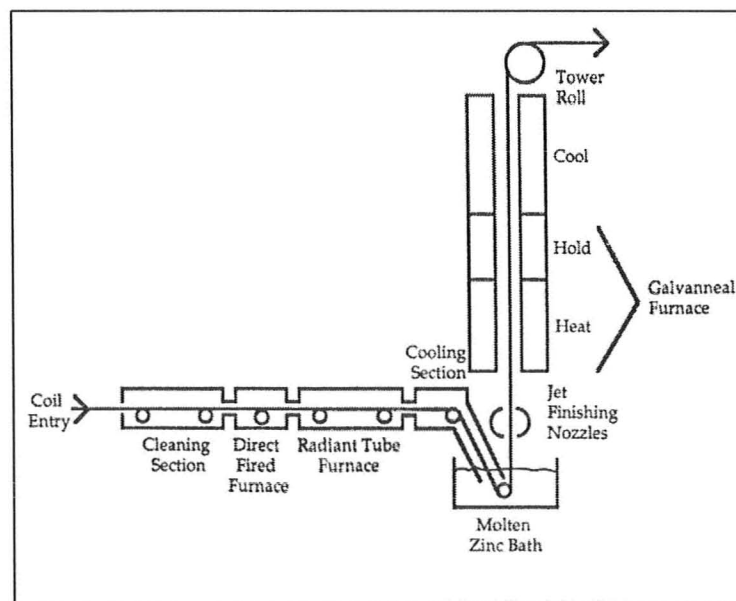


Figure 1-1. Schematic of a typical continuous hot-dip galvanizing line (CGL) [Marder 2000]

- (3) Cooling: The temperature of the molten zinc bath should not be affected by the steel strip heat content and thus, the steel strip is cooled down to bath temperature and held at this temperature for a defined time prior to immersion in the liquid zinc bath.
- (4) Dipping: The steel strip goes into the molten zinc bath and is held in the bath for a defined time to ensure good wetting of the steel surface with the liquid zinc.
- (5) Wiping: On exiting the liquid zinc bath, the strip is wiped with air or N₂ to remove excess liquid zinc. The desired zinc coating thickness is mainly controlled by the gas pressure distribution.
- (6) Galvannealing: For some applications, the steel strip is subjected to galvannealing heat-treatment right after the wiping section to form an Fe-Zn intermetallic coating.
- (7) Cooling: The steel strip is cooled in the ambient atmosphere. Normal industrial cooling rates are about 5-15 °C/s depending on the steel thickness, line speed, etc [Leory 1988].
- (8) Post-treatments: A number of subsequent processes are performed on the coating for different purposes such as temper-rolling, chromating, phosphating, etc.

Figure 1-2 displays an optical micrograph of the surface finish of a typical galvanized coating containing small concentration of Pb. Depending on the process

variables, the coating morphology and structure of the final zinc grains can be varied significantly. Generally, the crystallite diameter is about 1 mm which is above the threshold of human perception and, therefore, the grains are visible by the naked eye. This, in turn, is beneficial for construction applications in which decorative coating appearance is demanded. On the other hand, in some countries, galvanized steels are not accepted for exposed automotive applications in which the large size of zinc crystallites and surface irregularities such as grooves at grain boundaries deteriorate the paintability of zinc panels and results in the inferior appearance of the painted galvanized steels [Dutta 2004]. As a result, lower-cost galvanized steel sheets have been substituted by “featureless” galvanized steel sheets in exposed automotive applications. However, galvanizing customers always demand products with lower cost and better quality. Thus, producing microcrystalline galvanized steel sheets has become one of the main goals for the hot-dip galvanizing industry in these countries [McDermid 2000].

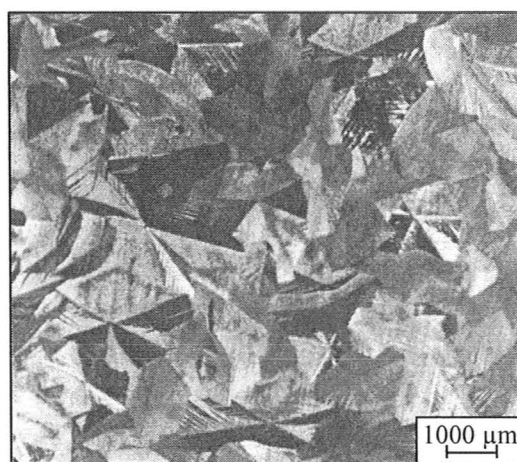


Figure 1-2. Optical micrograph of the surface finish of a typical galvanized coating containing small amount of Pb [Marder 2000]

Furthermore, galvanized steel sheets are evaluated based on their main properties such as weldability, corrosion resistance, surface reactivity, wear resistance, formability and cracking behavior [Szabo 2003]. Previous examinations have shown that the size and crystallographic orientation of zinc spangles, the uniformity of the coating structure and the distribution of solutes within the coating layer are the main factors that determine the final quality of galvanized steel sheets. The formation of zinc spangles as well as solute distribution across the coating occurs during coating solidification [Strutzenberger 1998] [Yasuda 2007]. So far, a number of investigations have been carried out on the solidification of hot-dip galvanized coatings [Cameron 1967] [Fasoyinu 1990] [Strutzenberger 1998]. However, solidification of these coatings is not yet well understood and, therefore, further study is essential to elucidate some of the remained questions concerning the solidification of hot-dip galvanized coatings.

In this study, a thorough literature survey on different aspects of the solidification of zinc coatings is presented in Chapter 2. Chapters 3 and 4 describe the detailed experimental work and results, respectively. Finally, the results are discussed in Chapter 5 and the overall conclusions of the study given in Chapter 6.

CHAPTER 2. LITERATURE REVIEW

2.1. Spangle Description

Zinc spangles are usually formed when small amounts of specific elements such as Pb, Sb or Bi are present in the molten zinc bath [Fasoyinu 1990] [Jin-Tang 2007] [Marder 2000]. By definition, spangles are the surface patterns on galvanized zinc coatings which consist of alternative shiny and dull areas [Cameron 1965]. An optical micrograph of a typical zinc spangle on the surface of galvanized steel is shown in Figure 2-1. Each spangle is essentially one single crystal of zinc that has a delineated internal dendritic structure [Fasoyinu 1993] [Jin-Tang 2007]. Generally, the nucleation site is positioned at the central point of each spangle from which the primary dendrite arms are radiated two dimensionally on the surface of the steel substrate [Cameron 1965]. Spangles can be a few millimetres to several centimeters in diameter and a few microns in thickness [Liu 2004] [Strutzenberger 1998]. It should be mentioned that zinc spangles and zinc grains commonly refer to the same crystallographic features on zinc coatings and are referred to interchangeably in the literature.

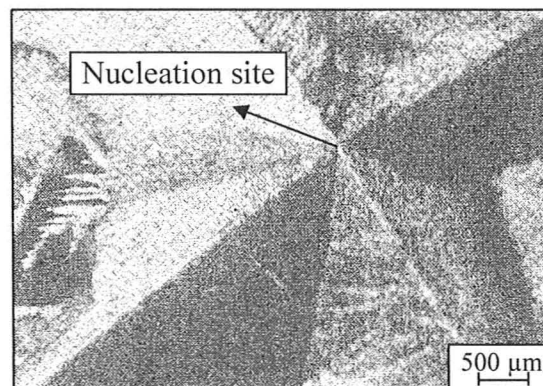


Figure 2-1. Optical micrograph of a typical zinc spangle on the surface of galvanized coating containing 0.2 wt% Pb [Fasoyinu 1990]

2.2. Spangle Formation

Solidification of zinc coatings essentially takes place under non-equilibrium conditions since the thin liquid layer is cooled rapidly. Under non-equilibrium conditions, the nucleation of close packed crystal planes with higher atomic density is favored due to their lower surface energy. As a result, lattice imperfections and preferred crystallographic orientations are formed during zinc coating solidification [Jordanovac 2004].

As was mentioned previously, a spangle is a monocrystalline zinc grain and thus, like any other crystallographic structures, spangle formation process involves (1) nucleation and (2) growth [Dutta 2005]. Each step is discussed separately herein.

(1) Nucleation

The driving force for heterogeneous nucleation, activation energy barrier against heterogeneous nucleation and the number of nuclei can be expressed using Equations 2-1(a-c) [Porter 1981].

$$\Delta G_r = -\frac{4}{3}\pi r^3 \frac{L_v \Delta T}{T_m} + 4\pi r^2 \sigma_{SL} \quad (\text{Equation 2-1(a)})$$

$$\Delta G_{het}^* = \left(\frac{16\pi\sigma_{SL}^3 T_m^2}{3L_v^2}\right) \left(\frac{1}{\Delta T^2}\right) \frac{(2 + \cos\theta)(1 - \cos\theta)^2}{4} \quad (\text{Equation 2-1(b)})$$

$$n^* = n_1 \exp\left(-\frac{\Delta G_{het}^*}{kT}\right) \quad (\text{Equation 2-1(c)})$$

Where

ΔG_r = change in Gibbs free energy for the formation of a nucleus with radius (r);

r = radius;

L_v = latent heat of fusion;

ΔT = thermal gradient;

T_m = melting point;

σ_{SL} = solid/liquid surface energy;

ΔG_{het}^* = activation energy barrier against heterogeneous nucleation;

θ = wetting angle;

n^* = number of nuclei;

n_1 = number of atoms in contact with the mould; and

k = Boltzmann's constant.

In order to study the nucleation mechanism of zinc spangles at the beginning of solidification, undercooling as well as the temperature gradient across the liquid zinc layer have been either measured experimentally or calculated theoretically.

The literature shows that a variety of data has been reported for the amount of undercooling within the galvanized layer. Cameron and Harvey observed 6 to 10 °C of undercooling while Kim and Patil reported 23 °C of undercooling in the liquid zinc film prior to solidification [Cameron 1967] [Kim 1985]. However, Fasoyinu and Weinberg argued that the previously reported data was not valid due to the errors associated with temperature measurements using an optical pyrometer. They proved that the actual amount of undercooling in either the bulk liquid zinc or across the galvanized layer was

less than 1 °C, which was consistent with the values reported by White [Fasoyinu 1990] [White 1971]. As a result of a relatively small undercooling in the liquid layer at the beginning of solidification, it was proposed that spangle nucleation occurred heterogeneously since a large undercooling would be necessary for homogeneous nucleation [Strutzenberger 1998].

Temperature gradients across the liquid zinc coating have been estimated theoretically and were found to be about 0.02 °C for a macroscopic cooling rate of 15 K/s [Strutzenberger 1998]. The negligible temperature difference between the steel/liquid zinc and liquid zinc/air interfaces implies that the nucleation of spangles is essentially independent of temperature gradient [Semoroz 2002-1]. In fact, Poulon-Quintin et al. proposed that nucleation is more likely a result of chemical affinities and/or geometric considerations [Poulon-Quintin 2004].

Regarding the heterogeneous nucleation of zinc spangles, nuclei could possibly be formed at the steel/liquid zinc interface, liquid zinc/air interface or within the liquid layer. It was proposed that solidification started at the steel/liquid zinc interface due to the presence of intermetallic compounds on the surface of the coating. The alloying elements and bath impurities were rejected from the solid/liquid interface and precipitated on the coating surface at the end of solidification [Poulon-Quintin 2004]. Also, the driving force for nucleation is higher on the rough solid surface of the steel substrate with higher surface energy and, therefore, nucleation is more favorable at the steel/liquid zinc interface [Liu 2004] [Semoroz 2001]. In addition, Cameron and Harvey agreed that at the beginning of solidification a thin zinc layer is formed on the surface of the steel while it is

covered by a thin liquid layer on the top. However, they also suggested that in the case of thinner substrates, thicker coatings and faster cooling rates, solidification starts on both interfaces [Cameron 1967].

On the other hand, Fasoyinu and Weinberg observed no progressive segregation trend from either interface and, therefore, concluded that nucleation occurred within the molten zinc layer [Fasoyinu 1989].

Thus, it can be concluded that spangle nucleation can possibly occur at either interface or within the liquid depending on the galvanizing process variables.

(2) Growth

As was mentioned previously, solidification of zinc spangles in molten liquid layer is essentially dendritic and dendrite arms tend to grow in the six $\langle 10\bar{1}0 \rangle$ fast growth directions lying in the basal plane of hexagonal Zn crystals [Cameron 1965]. Sometimes, growth directions deviate from these preferred crystallographic directions due to the effects of the substrate and liquid surface boundaries. Also according to Lindenmeyer, solute additions can alter dendrite growth directions [Semoroz 2000] [Lindenmeyer 1959].

Fasoyinu and Weinberg reported that the dendritic growth of zinc grains on steel substrates can be mathematically expressed using Equation 2-2 [Fasoyinu 1990] [Nash 1974].

$$V = 0.114 \left(\frac{\alpha_L \Delta S_f L}{\sigma_{SL} C_L} \right) \left(\frac{\Delta T C_L}{L} \right)^{2.65} \quad (\text{Equation 2-2})$$

Where

V = growth velocity;

α_L = thermal diffusivity of the liquid;

ΔS_f = entropy of fusion per unit volume; and

C_L = specific heat of liquid.

According to Strutzenberger and Faderl, the nucleus is formed on the surface of the steel and grows dendritically in the slightly undercooled melt along the steel/ liquid zinc interface since heat conduction is faster in the sideways direction versus through the nucleus [Strutzenberger 1998]. Thus, dendrite growth occurs rapidly in two dimensional space parallel to the surface of the steel until adjacent grains impinge on each other and the entire surface is covered with a very thin layer of zinc grains. This is the first step of solidification and it happens in less than one second (Figure 2-2(a)). In the second stage of solidification, slow thickening of zinc grains takes place which is mainly controlled by convection (Figure 2-2(b-d)). Once the spangles reach the liquid zinc/steel interface, solidification is finished.

Normally there is no eutectic structure present in galvanized coatings. However, it was reported that metastable phases can be formed during coating solidification since the complete rejection of solutes and impurities is impossible during rapid solidification (10^3 °C/s cooling rate) [Cameron 1965].

It should be mentioned that despite the three dimensional dendritic structure of spangles, spangle growth is considered to be two dimensional. This is because the first stage of solidification plays the major role in determining final shape, size and appearance of spangles [Poulon-Quintin 2004].

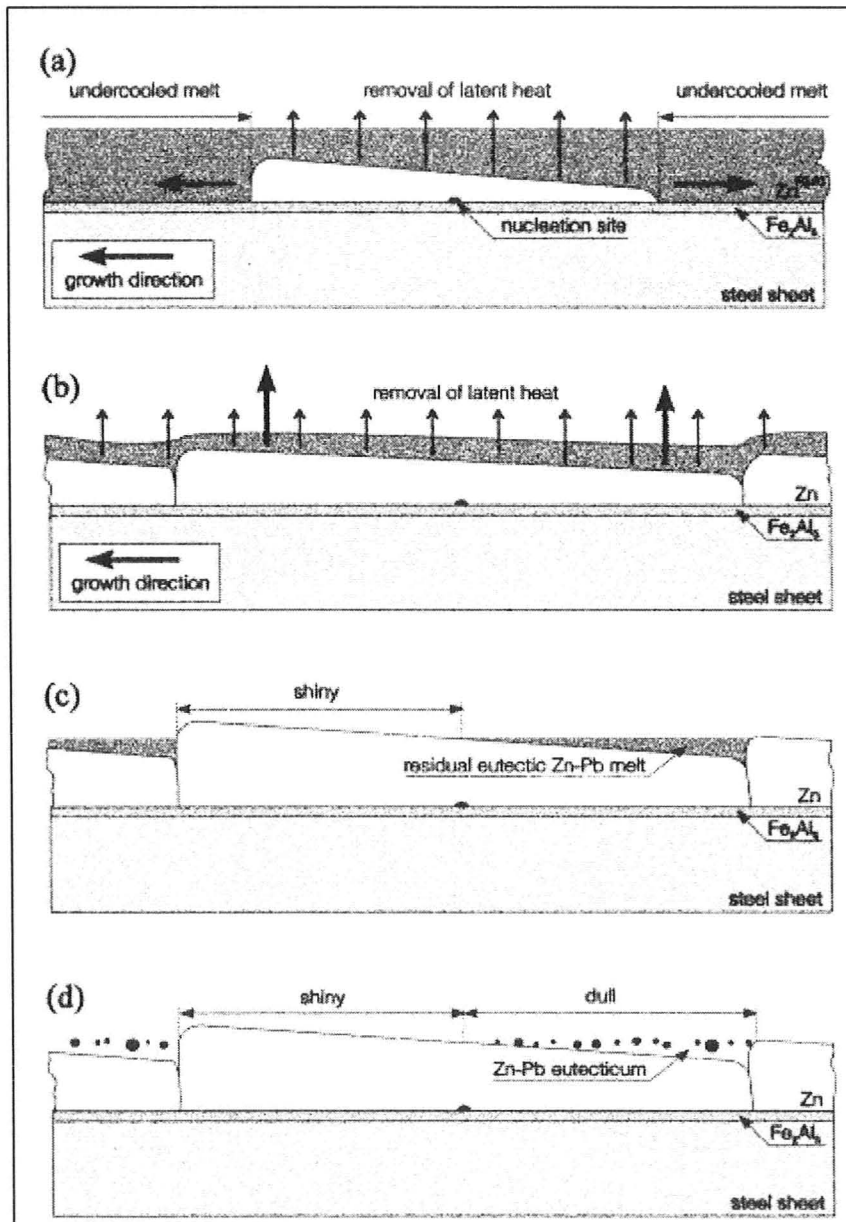


Figure 2-2. Schematic illustration of the solidification sequence for lead containing zinc layers: (a) rapid lateral expansion, (b) slow thickening process, (c) emergence of shiny sectors, and (d) eutectic Zn-Pb solidification [Strutzenberger 1998]

2.3. Spangle Morphology

The surface finish of galvanized coatings exhibit spangles with a variety of morphologies. Previous researchers have classified zinc spangles based on their appearance, size, dendrite orientation, amount of depression at grain boundaries and the presence of secondary or ternary dendritic arms [Chalmers 1964] [Zapponi 1999]. One of the most discrete classifications has been done by Strutzenberger and Faderl [Strutzenberger 1998]. Accordingly, spangles can be divided into shiny, feathery and dull categories macroscopically. In addition, dull areas can be subdivided into dimpled, ridged and orthogonal dendritic morphologies microscopically (Figure 2-3). The details of each class are described below.

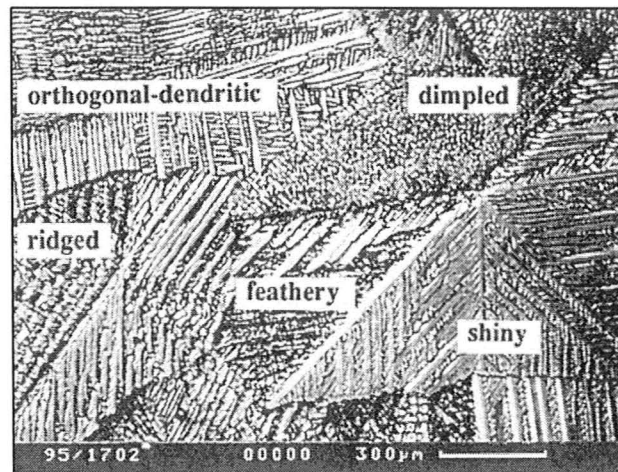


Figure 2-3. Optical micrograph of typical surface finish of galvanized steel exhibiting shiny, feathery, dimpled, ridged, orthogonal dendritic regions [Strutzenberger 1998]

- (1) Shiny or mirror-like: This class is usually assigned to highly reflective and bright areas on the zinc coating surface. Spangles exhibit delicate dendritic structure in these regions (Figure 2-4(a)). If the entire surface of one spangle is shiny, the spangle resembles a snowflake in which the primary dendritic arms are present in straight lines located in the six $\langle 10\bar{1}0 \rangle$ fast growth directions and the spangle has 6-fold symmetry [Jin-Tang 2007]. Also, these spangles have been reported to be zinc single crystals. Regarding crystallographic orientation, it was shown that shiny spangles have a preferred basal orientation which means that the basal plane of the hexagonal zinc crystal is parallel to the surface of the steel. Due to the decorative appearance and high corrosion resistance, this type of coating is highly desired by galvanizing customers [Biber 1998].

- (2) Feathery: This category represents spangles which are relatively reflective and consist of alternative bright and dull sectors (Figure 2-4(b)). Dendritic structures can be clearly observed in bright sectors while they are not as obvious in dull sectors. The presence of feathery areas was attributed to insufficient residual liquid being present at the end of coating solidification which could not cover all dendrite branches and resulted in the formation of lath-like pattern in these regions [Strutzenberger 1998]. Also, it was reported that there is a slight misorientation between adjacent sectors in feathery areas [Fasoyinu 1993]. However, Strutzenberger and Faderl reported that the difference in appearance of shiny and dull segments was not due to orientation differences. They proposed that if a portion of each spangle solidified towards the molten zinc/air interface, it

formed a shiny segment and if it solidified towards the steel/molten zinc interface, it formed a dull segment [Strutzenberger 1998].

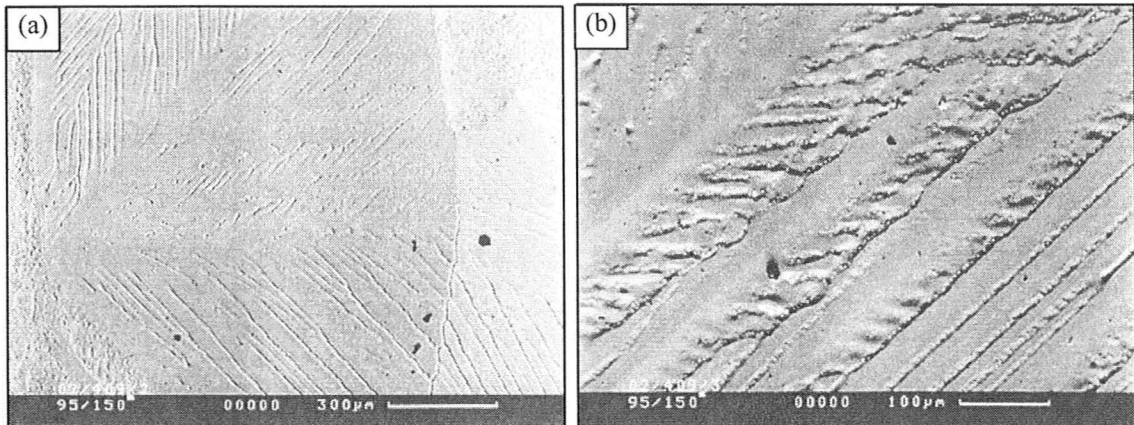


Figure 2-4. Scanning Electron Microscopic (SEM) surface image of (a) shiny (b) feathery area [Strutzenberger 1998]

- (3) Dull: Spangles belonging to this class are solute enriched and display low reflectivity [Dutta 2005]. These spangles are typically characterized by precipitated pure Pb or Sb particles on the coating surface [Singh 2003]. In most cases, spangles have pyramidal or prismatic crystallographic orientation in dull regions in which half of the inclined grain reaches the surface of the liquid first while the other half is still covered with residual liquid enriched in solutes or impurities. This liquid precipitates at the end of coating solidification and results in a dark appearance [Zapponi 1999]. In addition, the lower packing factor of the non-basal planes present in these regions results in a less reflective surface [Singh 2003]. Also, dull coatings are not acceptable among galvanizing users due to their dark appearance and lower corrosion resistance [Marder 2000]. In order to decrease dull areas on zinc coatings, delayed solidification should be prevented

since solidification of these areas occurs at the last stage of coating solidification. This can be done by applying either lower bath temperature or faster cooling rates to the coating to make the solidification period shorter [Hanna 1984].

Microscopic structures within dull spangles can also be divided into the following three classes [Strutzenberger 1998].

- i. Dimpled: This class has been also termed granular or honey-comb structure previously [Zapponi 1999]. In dimpled spangles, spherical pure Pb particles are distributed randomly over the uneven zinc surface (Figure 2-5(a)).
- ii. Ridged: Pure Pb particles distributed along straight lines exhibit a ridged morphology on the coating surface (Figure 2-5(b)).

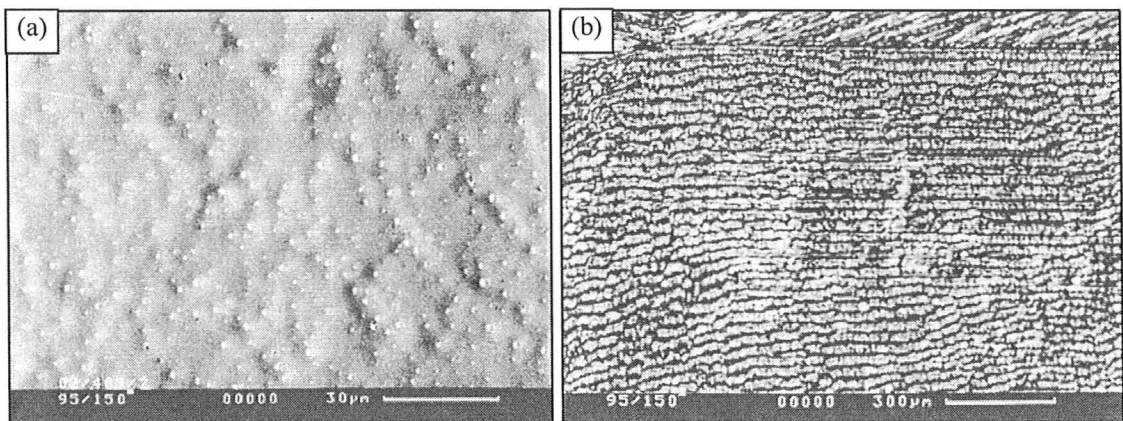


Figure 2-5. SEM surface image of (a) dimpled (b) ridged area [Strutzenberger 1998]

- iii. Orthogonal-dendritic: In this type of structure, secondary dendrite arms are formed perpendicular to the primary trunk with pure Pb particles formed in between the arms (Figure 2-6). Thus, the basal plane of the zinc crystal is perpendicular to the steel surface in the orthogonal-dendritic regions.

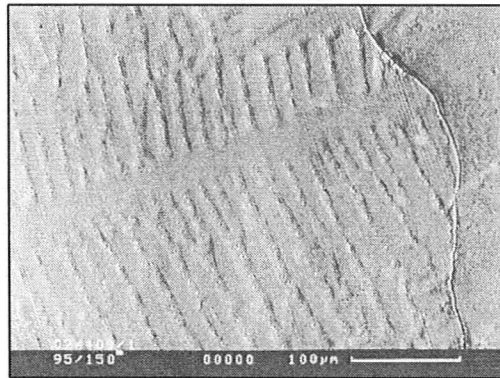


Figure 2-6. SEM surface image of orthogonal dendritic area [Strutzenberger 1998]

2.4. Spangle Shape and Crystallography

It has been reported that external process factors such as cooling rate during coating solidification and the surface condition of the steel substrate determine the crystallographic orientation of spangles [Chang 1994]. As was mentioned previously, each spangle is essentially a single crystal of zinc. However, it was also mentioned that the orientation of the spangle is not constant and gradually changes in different areas [Strutzenberger 1998]. Semoroz et al. observed 80 percent of the single crystal zinc grains and 20 percent of poly-crystalline grains with two or three orientation domains on a coating containing 0.2 wt% Al and 0.15 wt% Sb [Semoroz 2002-2]. Based on their study,

all these domains were formed from one nucleation site at the center of the grain and are crystallographically related to each other.

Depending on a spangle crystallographic orientation, it may appear in different shapes [Fasoyinu 1993]. Based on Jin-Tang et al.'s examinations, there is a correlation between the inclination angle of the zinc crystal basal plane with respect to the steel surface and the spangle geometry. They deduced an expression which relates the inclination angle of the basal plane (β) to the angle between primary dendritic arms (α) (Equation 2-3). Figure 2-7 shows that when the basal plane is inclined relative to the substrate surface, the angle between the dendrite arms increases and, as a result, the spangle shape changes [Jin-Tang 2007].

$$\alpha = 2 \arcsin \frac{1}{2 \cos \beta \sqrt{1 + \frac{1}{4} \tan^2 \beta}} \quad (\text{Equation 2-3})$$

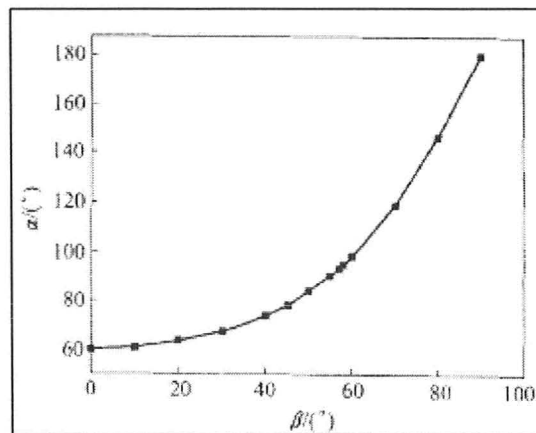


Figure 2-7. The plot of α as a function of β [Jin-Tang 2007]

Generally, spangle shape can be classified into the following three categories [Jin-Tang 2007]:

- (1) Hexagonal, ($\beta = 0^\circ$): A perfect hexagonal spangle is formed on the coating surface when the C-axis of the zinc crystal is within 5° of the normal to the steel surface and the angle between primary dendrite arms is approximately 60° (Figure 2-8(a)). In this case, the basal plane of the crystal is aligned more or less parallel to the steel surface and the (0001) peak has the highest X-ray diffraction (XRD) intensity (Figure 2-8(b)). Hexagonal spangles impinge the steel/molten zinc and molten zinc/air interfaces at small angles and, therefore, their growth kinetics are not affected by interfaces. Thus, this type of spangle has the maximum possible area (Waitlevertch 1976).

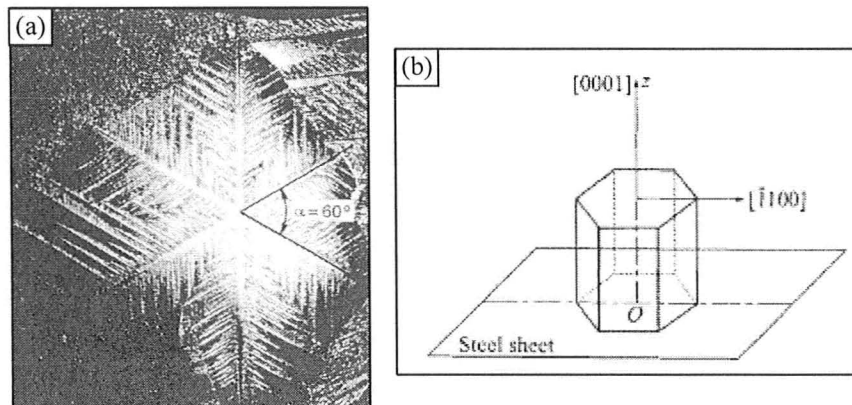


Figure 2-8. (a) Optical micrograph of a hexagonal spangle (b) schematic of crystal orientation [Strutzenberger 1998] [Jin-Tang 2007]

According to Cameron and Harvey straight lines which separate the shiny and dull regions in these spangles mostly lie in fast-growth $\langle 10\bar{1}0 \rangle$ directions and rarely in the $\langle 0001 \rangle$ direction [Cameron 1965]. It has also been reported that sometimes a feathery sector is formed between the shiny and dull segments. Also the spangle is symmetrical since the heat flow and, thus, dendrite growth velocity is equal for all six $\langle 10\bar{1}0 \rangle$ directions [Strutzenberger 1998].

- (2) Octagon/complicated ($0^\circ < \beta < 90^\circ$): In this class, the zinc crystal C-axis can be misaligned from 5° to 85° and the angle between primary dendrite arms lies in the 60° to 180° range (Figure 2-9(a)). The basal plane of zinc crystal is inclined with respect to the steel plane as shown in Figure 2-9(b). Thus, one of the pyramidal planes such as $\{10\bar{1}1\}$, $\{10\bar{1}2\}$, $\{10\bar{1}3\}$, $\{10\bar{1}4\}$ or prism planes such as $\{10\bar{1}0\}$ are aligned parallel to the steel surface.

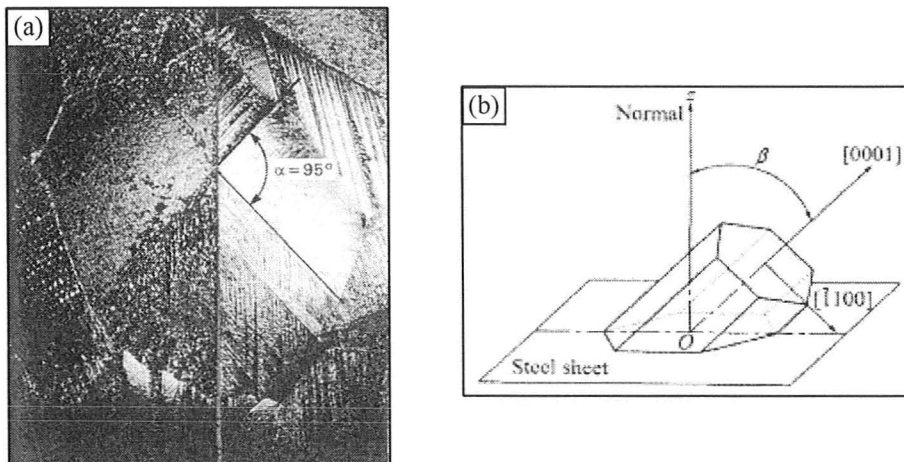


Figure 2-9. (a) Optical micrograph of an octagon spangle (b) schematic of crystal orientation [Strutzenberger 1998] [Jin-Tang 2007]

Also, as the inclination angle increases, the maximum heat flow direction does not coincide with the preferred crystallographic growth directions and, therefore, spangles appear in irregular shapes [Strutzenberger 1998].

- (3) Rhombus ($\beta = 90^\circ$): When the C-axis of the zinc crystal is aligned parallel to the steel plane and the angle between primary dendritic arms is 180° , the spangle displays a rhombus shape (Figure 2-10(a)). Figure 2-10(b) illustrates a schematic of a zinc crystal which was formed parallel to the steel plane and, therefore, the $(10\bar{1}0)$ peak has the highest XRD intensity. The four growth directions for primary dendrite arms belong to two $\langle 0001 \rangle$ and two $\langle 10\bar{1}0 \rangle$ directions. Due to the anisotropy of the solid-liquid interfacial energy on the (0001) plane (70 mJ/m^2) compared to the $(10\bar{1}0)$ plane (100 mJ/m^2), dendrite growth velocity is different in the $\langle 0001 \rangle$ and $\langle 10\bar{1}0 \rangle$ directions and, thus, the spangle becomes rhombus [Mackowiak 1979] [Jordanova 2004].

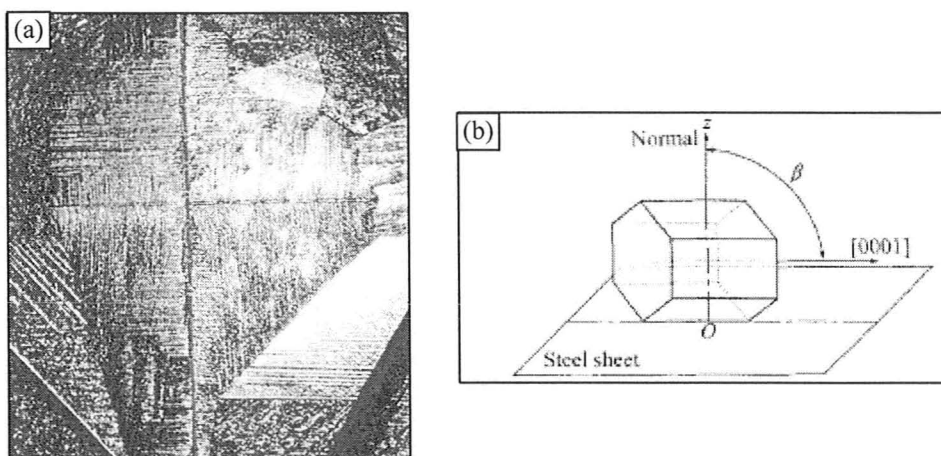


Figure 2-10. (a) Optical micrograph of a rhombus spangle (b) schematic of crystal orientation [Strutzenberger 1998] [Jin-Tang 2007]

It should be mentioned that the above geometrical shapes for spangles can display either a shiny or dull morphology. However, in dull areas, the spangle surface is covered by dimpled areas and their perimeter may not be as evident as it is for shiny spangles [Dutta 2005].

2.5. Spangle Reflectivity and Roughness

Surface reflectivity of a coating is related to the spangle surface roughness, which in turn depends on the nature and amount of alloying elements on the surface as well as the spangle crystallographic orientation [Fasoyinu 1990] [Strutzenberger 1998]. When spangles grow toward the molten zinc/air interface, shrinkage appears as depressions on the spangles surface at the end of solidification. As a result, these surfaces become rough and cannot reflect light completely. On the other hand, smooth spangles grow towards the steel/molten zinc interface and, therefore, the spangle surface is free of shrinkage depressions and is bright [Biber 1988]. Also, when any inclined grain reached the liquid surface, shiny areas are formed while the residual liquid becomes continuously enriched in Pb and other alloying elements or impurities. Finally precipitation occurs at the end of solidification and the corresponding region appears dull with low reflectivity due to the presence of precipitates on the surface. Hence, a grain inclined with respect to the steel plane may form dull and shiny areas [Semoroz 2002-2] [Strutzenberger 1998].

According to Helwig, surface reactivity is inversely related to the spangle appearance [Helwig 1981]. He reported that chromate film was more effective on coatings with basal crystallographic texture and bright appearance. Thus, it was

concluded that dull spangles have different surface composition compared to bright spangles [Biber 1988]. Also, Waitlevertch reported that dull spangles have more aluminum and Pb [Waitlevertch, 1976] [Faderl 1995]. Subsequently, Franks et al. reported that these areas also have more Sb as well [Franks 1976].

Surface topography of the galvanized coatings is important for external applications where smooth and reflective surface are demanded such as for exposed automotive body panels. Temper-rolling is one of the post-treatments which can flatten the coating surface to certain amount but it cannot remove grain boundary grooving [Fasoyinu 1993].

2.6. Spangle Nucleation and Growth Mechanisms

As was mentioned previously, spangles are typically a few millimeters to several centimeters in diameter and are visible to the naked eye. To explain the abnormal size of spangles, two approaches are applicable: nucleation and growth. So far, the following explanations have been proposed to describe the nucleation and growth of spangles during zinc coating solidification.

- Certain elements in molten zinc bath can segregate and physically block the available nucleation sites at the onset of solidification. Also, there are two energy barriers for nucleation: (i) the surface energy barrier between the solid and liquid interfaces during solidification and (ii) the chemical potential for zinc atom cluster formation without any solute. The sum of one physical barrier and two energy

barriers is termed the poisoning effect and can slow the nucleation rate. As a result, larger zinc spangles are formed [Liu 2004].

- According to Spittle and Brown, spangle forming elements increase the undercooling necessary for heterogeneous nucleation and, therefore, decrease the nucleation rate [Spittle 1991]. However, Fasoyinu and Weinberg proved that the actual undercooling in either the molten zinc layer or the bulk zinc is less than 1 °C and thus, it is unlikely that large undercooling would be responsible for the formation of large spangles [Fasoyinu 1990].
- Cameron et al. proposed that small Pb addition can dissolve nuclei on the steel surface by chemical reaction and, therefore, decrease the nucleation rate which results in larger grain structure [Cameron 1967].
- In alloy solidification, dendritic growth is due to either thermal or constitutional undercooling. Constitutional undercooling is due to solute segregation which can be quantified by the segregation coefficient. Fasoyinu and Weinberg showed that the segregation coefficient is very low for Sb, Bi, Pb and Sn (Table 2-1). However, Sn does not produce spangles by itself. Thus, spangle growth cannot be solely explained based on segregation [Fasoyinu 1990].
- It was reported that spangle producing solutes are soluble in liquid zinc and insoluble in solid zinc. Thus, they segregate in front of the solid-liquid interface and decrease the interfacial free energy. The surface energy of these elements is shown in Table 2-1 [Strutzenberger 1998]. Liu et al. calculated the segregation of

solute in the liquid zinc based on thermodynamic data and found that very small amount of these solutes can result in significant segregation of solute to the melt surface and consequently decrease the surface energy [Liu 2004]. This, in turn, increases the growth rate of the dendrite tip and, thus, the number of nuclei on the surface is decreased. Thus, the resultant microstructure consists of large spangles [Fasoyinu 1990].

Table 2-1. Estimated segregation coefficients and surface tension for binary alloys [Fasoyinu 1990]

Alloy $C_0 = 0.2$ (Wt Pct)	Estimated Segregation Coefficient k	$\frac{C_s}{C_0}$ k (Wt Pct)	Surface Tension of Alloying Element (Nm^{-1})
Zn-Al	0.20	1	0.860
Zn-Pb	<0.01	>20	0.470
Zn-Sb	<0.01	>20	0.395
Zn-Bi	<0.01	>20	0.375
Zn-Cd	0.05	4	0.590
Zn-Sn	<0.01	>20	0.566
Zn-Mg	0.05	4	0.583
Zn	—	—	0.760

- Applying phase field modeling methods to the solidification of hot-dipped galvanized coatings, Semoroz et al. reported that even though solid-liquid interfacial energy determines the dendrite growth directions, boundary conditions may alter these directions from that the interfacial energy imposes on a three dimensional system. In fact, boundaries determine the plane on which dendrites can grow and anisotropy finds the fast growth directions on this plane. They also found that the wetting angle at both the steel/molten zinc and molten zinc/air interfaces has to be equal to or greater than 90° . At this wetting condition, the

growth velocity decreases as the incidence angle increases and thus, Fasoyinu and Weinberg's hypothesis was proved to be invalid [Semoroz 2000].

In industry, spangle minimization is carried out more effectively using the "Heurtey" process or "atomized steam" process. In the first method, 0.5 μm zinc powder is blown against the surface of the galvanized layer during coating solidification and hence, the spangle nucleation rate is increased leading to the formation of spangles of 0.1-1.5 mm diameter. In the second process, zinc powder is substituted by high pressure steam which is blown on the surface of galvanized layer similarly. Using this method, final spangle size is about 0.1-2.5 mm [Fasoyinu 1990]. Furthermore, smaller spangles can be produced with fast cooling of the coating if it contains no Pb, Sb or Bi additions [Leory 1988].

2.7. Effect of Process Variables on Spangle Size

A number of galvanizing process variables have been reported to have influence on the final coating microstructure such as line speed, steel substrate thickness, coating thickness, zinc bath temperature, coating weight, etc [Hanna 1984]. Many examinations have been carried out to find the most important factors which are responsible for large spangle size. It was deduced that chemical composition of the molten zinc bath, steel surface condition and coating cooling conditions during solidification are the most effective and independent factors which govern spangle formation [Dutta 2005] [Fasoyinu 1990]. The influence of each parameter is discussed in detail below.

- Chemical composition of the molten zinc bath: Small amounts of various alloying elements have been introduced to the zinc bath for different purposes such as better zinc drainage, higher surface reactivity, improved uniformity and brightness. Also, some alloying elements can suppress the steel surface reactivity with the liquid zinc bath, particularly for those substrates containing P and Si [Chidambaram 1991] [Vourlias 2004] [Zervoudis 2005].

Liquid zinc bath should always be saturated with Fe to prevent iron dissolution in the zinc bath. The amount of Fe addition to the galvanizing baths is determined based on the solubility curves at each Al level [McDermid 2007]. Also, molten zinc reacts with the steel substrate and forms a series of Fe-Zn intermetallic compounds at the steel/molten zinc interface. These intermetallic phases are known to be brittle and detrimental to mechanical properties. To prevent the reaction between liquid zinc and steel substrate, small concentrations of Al are commonly added to the galvanizing baths to form a thin Fe₂Al₅ film at the steel/liquid zinc interface. This layer is known to hinder the formation of brittle Fe-Zn intermetallic compounds at the interface and increase the coating ductility.

Bath composition is mainly responsible for the formation of large zinc spangles in zinc coatings [Cameron 1967]. The presence of small quantities of Pb, Sb and Bi in the liquid zinc is known to produce large zinc spangles. Furthermore, zinc spangle size increases with increasing bath Pb, Sb or Bi content and levels off

beyond a critical concentration (Figure 2-11), [Fasoyinu 1990] [Pisdofidis 2007] [Vourlias 2004].

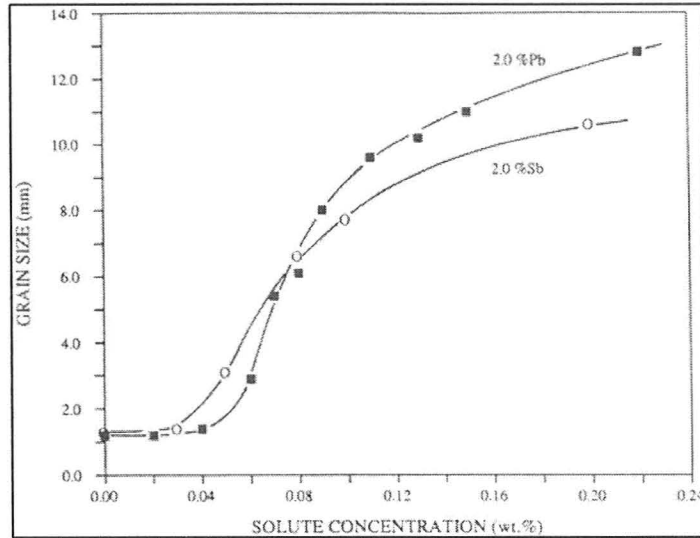


Figure 2-11. Zinc grain size as a function of solute concentration [Fasoyinu 1990]

In addition, Cameron and Harvey reported that when Sn is also present in the bath, extra large spangles are formed. This is because Sn increases the solidification temperature range and, therefore, dendrites have more time to grow before the temperature reaches the solidus [Cameron 1967]. Furthermore, experiments showed that individual additions of Sn, Cd and Mg do not form spangles [Fasoyinu 1990].

- Steel surface condition: Cleanliness and roughness of the steel surface directly affects the final quality of the coating [Garza 2007]. Sufficient pre-treatment cleaning of the steel sheet reduces blisters, bare spots, black spots and surface roughness of the final coating [Hanna 1984]. As mentioned previously, it has been proposed that nucleation happens heterogeneously on the surface of steel

substrate due to low undercooling present in the liquid zinc layer. As a result, the surface condition of the steel substrate is important in determining the number of effective nuclei. According to Sere et al. [Sere 1997], surface roughness affects the coating thickness, grain size and crystallographic texture. Steel surface roughness can directly be related to nucleation rate for zinc spangles. Keeping all parameters constant, Strutzenberger and Faderl observed smaller zinc grains on a coated aluminum killed (AK) steel compared to a coated interstitial free (IF) steel and attributed this difference to the higher surface roughness of the AK steel [Strutzenberger 1998]

- Cooling conditions during coating solidification: Dendrite growth velocity increases at higher undercooling and thus, the length of dendrite arms is determined by the amount of undercooling present in first step of solidification [Lindenmeyer 1959]. More importantly, cooling rate during the first stage of solidification controls the expansion rate of spangles in the lateral directions. Cameron and Harvey observed larger spangles for slow cooling of the zinc coating [Cameron 1967] [Gutenberg 1990].

2.8. Coating Crystallographic Texture

Once the nucleus is formed, competition between the maximum heat flow directions and the anisotropy of growth velocity determines the growth directions [Chalmers 1964]. Generally, hot-dip galvanized zinc coatings exhibit basal crystallographic texture. In other words, the C-axis of zinc crystals tends to be aligned at

small angles with respect to the steel surface. Using the EBSD technique, Semoroz et al. studied the Orientation Distribution of Grains (ODG) as well as the crystallographic texture of a coating containing 0.2 wt% Al and 0.15 wt% Sb. They categorized the values of inclination angle of the basal plane with respect to the steel sheet into four classes and counted the number of grains per orientation class over the total number of grains. The surface area of grains belonging to each class over the total surface area was defined as the crystallographic texture. ODG and crystallographic texture values are representative of the nuclei orientation and growth direction, respectively. The experimental results were compared with a random distribution and shown in Figure 2-12. Accordingly, both the ODG and crystallographic texture are preferably distributed in the (0001) basal class which implies that the nuclei are preferentially oriented with respect to the plane of the sheet and these basal nuclei are favorable for growth [Semoroz 2002-1].

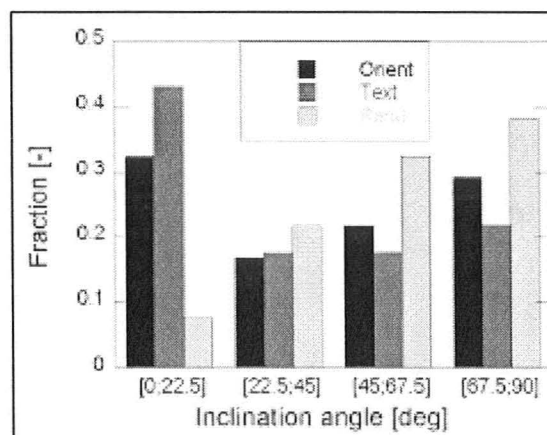


Figure 2-12. ODG and texture of zinc coating compared to random distribution as a function of the inclination angle of the basal plane [Semoroz 2002-1]

The ODG and texture values for zinc coatings and directionally solidified zinc bulk alloys are compared in Table 2-2. It can be concluded that nuclei orientation as well

as growth directions are independent of substrate and specific for zinc. However, growth is constrained by geometry and interfaces affect the crystallographic texture in coatings while in bulk solidification, growth is parallel to the maximum heat flow [Semoroz 2002-1].

Table 2-2. Characteristics of zinc crystals in zinc coatings and bulk alloys [Semoroz 2002-1]

	Coating	Bulk (Directional)
ODG	(0001) // surface	(0001) // surface
Dendritic growth directions	fast: $\langle 10\bar{1}0 \rangle$ -type slow: $\langle 0001 \rangle$ -type	fast: $\langle 10\bar{1}0 \rangle$ slow: $\langle 0001 \rangle$
Spatial growth direction	// surface	// thermal gradient
Texture induced by growth	(0001) // surface	(0001) \perp surface

In general, zinc coatings with dominant basal texture provide better corrosion resistance, paint adherence and mechanical properties due to the fact that (0001) planes are close packed and the binding energy of the surface atoms is higher. The surface of basal spangles is smooth, homogeneous and exhibits small alloying segregation on the surface [Chang 1995] [Rodnyansky 2000]. Also, deformation happens via slip rather than cracking or twinning. Thus, (0001) planes are more corrosion resistant [Scully 1990].

It was observed that coatings with basal texture have better paint adhesion whereas coatings with non-basal texture have poor adhesion [Ledheiser 1976]. According to Jaffrey, non-basal grains have rough surface and retain carbonaceous material on their surface and, therefore, have poor paint adhesion [Jaffrey 1980] [Chattopadhyay 2008].

Deformation in hexagonal close packed materials happens in different ways. Slip happens in basal plane and in the $\langle 11\bar{2}0 \rangle$ directions for bulk zinc at room temperature. Deformation can also occur via pyramidal slip, twinning or grain boundary separation [Shah 1996]. If there are not enough slip systems present, intergranular cracking (grain separation) or transgranular (cleavage) cracking occurs. Thus, coatings with non-basal texture crack more readily while coatings with basal texture tend to fail at high levels of strain [Jaffrey 1980] [Culcasi 2009] [Culcasi 1999].

2.9. Effects of Antimony on Zinc Coatings

It was mentioned that small amounts of various alloying elements can be added to the galvanizing zinc bath to improve the final coating quality. Pb has been one of the most widely used elements in the continuous galvanizing process [Konecny, 1972]. It was traditionally added to the molten zinc baths to produce a uniform coating with decorative appearance and better adhesion properties. Also, small concentrations of Pb can lower the surface tension of the liquid zinc bath and ease the gas-jet wiping process. As a result, galvanizers could decrease the bath temperature which in turn increases kettle lifetime and energy costs. In addition, Pb accumulated at the bottom of the bath and, therefore, it could float bottom dross and ease its removal (Zervoudis 2005). However, Pb particles exist on grain boundaries and enlarge the opening at these areas and increase the corrosion rate. Due to the environmental and health issues associated with Pb additions, this element has been removed from galvanizing baths and substituted by Sb. Sb additions have a similar influence on hot-dip galvanized zinc coatings. Additionally, unlike Pb, Sb

promotes the basal texture slightly and, therefore, increases the corrosion resistance of the coating (Figure 2-13 (a) and (b)) [Asgari 2007] [Sere 1999]. Sb interacts with Zn and forms different intermetallics such as AlSb, SbZn, Sb₂Zn₃ and Sb₃Zn₄ within the spangles rather than at grain boundaries [Shindo 1982] [Kabeya 1990]. However, coatings containing Sb are made up of extra large spangles which are not currently demanded by the galvanizing industry.

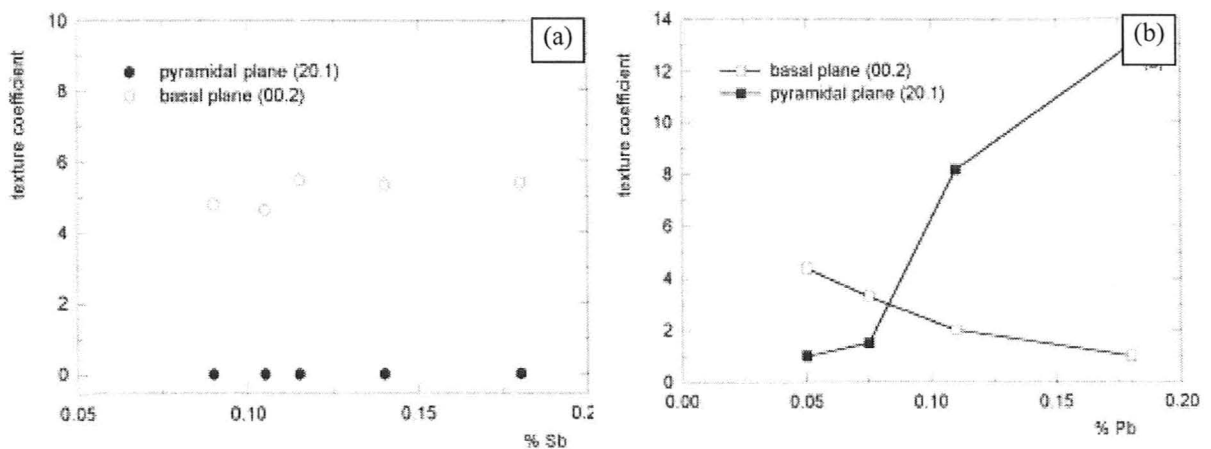


Figure 2-13. (a) Texture coefficient as a function of Sb or (b) Pb content of galvanizing bath [Asgari 2007]

2.10. Intermetallic Compounds

A number of alloying elements and impurities are present in the galvanizing baths which may be soluble in liquid zinc and insoluble in solid zinc. Thus, these solutes are rejected from the solid-liquid solidification front and form various precipitates on the coating surface at the end of solidification [Sere 1999]. On shiny spangles, these insoluble intermetallic compounds are present in interdendritic regions while primary arms are solute depleted. On the other hand, the intermetallic particles are distributed randomly over the entire surface of dull spangles. Observations showed that the average

concentration of solutes and impurities is higher on dull surfaces compared to shiny surfaces [Dutta 2005]. In dull areas, basal planes of zinc crystals have been found to be inclined to the steel sheet surface and as a result, the six $\langle 10\bar{1}0 \rangle$ fast growth directions do not lie in parallel to the steel surface. Thus, solutes and impurities are rejected towards the surface of the coating and form higher amounts of precipitates on the surface. In shiny regions, the zinc crystal basal planes are parallel to the surface and the six $\langle 10\bar{1}0 \rangle$ fast growth directions are within this plane. As a result, solutes and impurities are rejected towards grain boundaries and leave the surface relatively pure [Semoroz 2002-2].

When Al, Fe and Sb are present in the liquid zinc bath, a number of intermetallic compounds have been observed on the coating surface such as Fe_2Al_5 , FeAl_2 and FeAl_3 [Helwig 1981]. Furthermore, Auger maps showed equal atomic concentrations for Al and Sb on the surface which implies that the AlSb phase is also present in interdendritic areas, grain boundaries and dull spangles. SbZn , Sb_2Zn_3 and Sb_3Zn_4 were also detected on the coatings containing Sb.

It should be mentioned that even though the Al content of the liquid zinc bath is very small, it diffuses to the surface due to its high affinity for oxygen and forms a very thin and continuous (~ 5 nm) Al_2O_3 layer on the surface of the coating [Leory 1980] [Kilbane 1982] [Payling 1985]. It covers the surface of both shiny and dull spangles. The thickness of the alumina layer depends on the cooling rate during coating solidification and its composition is a function of bath composition. This layer was observed in the form of nodules as well as a continuous film [Furdanowicz 1999].

2.11. Depressions and Cracks

Examination of dull spangles showed the presence of small pits on the surface [Biber 1988]. Also, deep depressions are usually observed at the periphery of shiny or dull spangles where they impinge on adjacent spangles. It was proposed that solidification shrinkage is responsible for the formation of depressions. However, these large depressions increase with higher bath additions and, therefore, it was concluded that these depressions are not solely due to volume shrinkage. It was suggested that when a spangle is tilted, it pulls the liquid down at grain boundary region and results in very thin coating at these areas. The pull-over mechanism depends on the surface tension of the melt. This, in turn, is a function of surface oxidation and alloying elements present in the bath which can alter the melt surface tension [Fasoyinu 1993].

In addition to pits and depressions, cracks were also detected on the coating surface and within the coating mainly at the grain boundary regions. Crack formation was proposed to be the result of thermal expansion stresses due to coating contraction during solidification and residual thermal stresses due to the difference in the thermal expansion coefficients of the coating and substrate [Jordanova 1004].

Grain boundary cracks may be detrimental to mechanical or corrosion properties since mechanical stress and corrosive agents can potentially be accumulated in these regions. As a result, one should consider the presence of these cracks on the coating in application and find ways to minimize them. The amount of holes due to shrinkage is constant and cannot be minimized further, while the amount of shrinkage due to

expansion can be controlled. This can be done with determining the optimized gas flow rate during cooling of the coating. The higher is the cooling rate, the larger the cracks. According to Cameron et al. at fast cooling deep grooving occurs at the grain boundaries and are reduced by slow cooling while large spangles are formed [Cameron 1965].

Consequently, the main objectives of the current research are to experimentally explore the effect of some of the important process variables on the solidification and microstructural development of zinc coatings and subsequently refine the search for experimental conditions leading to optimal spangle size and structure in hot-dip galvanized coatings.

CHAPTER 3. EXPERIMENTAL PROCEDURE

Among various hot-dip galvanizing process variables, it has been reported that the final microstructure of the coating is mainly determined by the chemical composition of the molten zinc alloy bath, steel surface topography and cooling conditions during coating solidification [Dutta 2005] [Fasoyinu 1990]. In the present work, the influence of Sb additions to the molten zinc bath, surface roughness of the steel substrate and coating cooling rate on the microstructural development of zinc coatings during solidification have been investigated. Galvanizing experiments were carried out based on the experimental matrix shown in Table 3-1. Accordingly, five bath compositions, two steel substrates and three cooling rates were examined.

Table 3-1. Experimental matrix for galvanizing experiments

Zinc bath	Bath designation (wt%)	Steel type	Cooling rate (°C/s)
No. 1	Zn-0.2 Al-0 Sb	Bright-rolled steel (BR)	10
No. 2	Zn-0.2 Al-0.01 Sb	Hot-rolled steel (HR)	1
No. 3	Zn-0.2 Al-0.03 Sb		0.1
No. 4	Zn-0.2 Al-0.1 Sb		
No. 5	Zn-0.2 Al-0.2 Sb		

3.1. Materials

Two types of low carbon steel sheets were chosen for dipping experiments. The 0.90 mm thick bright-rolled steel (BR) produced using polished cold rolls and the 1.98 mm thick hot-rolled steel (HR) produced using normal grind rolls at high temperature were provided in the cold rolled and hot rolled conditions, respectively. Table 3-2 summarizes the result of chemical analysis that was performed on each type of steel

substrate using CS-444 Carbon/Sulphur determinator and Inductively Coupled Plasma (ICP).

Table 3-2. Chemical analysis of the steel substrates (wt%)

Steel type \ Element	C	Mn	Cu	Cr	Al	Ni	Sn
Bright-rolled steel (BR)	0.036	0.162	0.052	0.031	0.028	0.017	0.100
Hot-rolled steel (HR)	0.048	0.207	0.083	0.044	0.019	0.027	0.005

BR steel sheets and HR steel sheets were cut into 120 mm by 200 mm rectangular panels using a shear and a band saw, respectively. For all panels, cutting was performed in the way that the rolling direction of the sheet was parallel to the longitudinal axis of the panel. Also the bottom corners of each panel were cut to ensure safe movement inside the simulator column. Figure 3-1 shows a schematic of a standard panel. Once the panels were cut, surface cleaning was carried out using a 2% NaOH solution at 80 °C for 120 s which was followed by nylon brushing, ultrasonic cleaning in isoproponal for 5 minutes and drying in a warm air stream. No special storage was carried out for steel panels prior to dipping experiments.

Special high grade Zn ingots, Zn-5.13 wt% Al shots, high purity Fe chips and Sb beads were provided for making molten zinc alloy baths. The Fe and Sb were supplied by Sigma Aldrich Company.

Regarding the molten zinc alloy baths, the Al content of each bath was held constant at approximately 0.2 wt% dissolved Al, where all baths were Fe saturated. The Fe addition was calculated from Zn-Al-Fe solubility curves of McDermid et al.

[McDermid 2007]. Sb beads were added to the molten zinc alloy bath at each bath composition based on the experimental matrix (Table 3-1). To verify the bath composition prior to dipping experiments, chemical composition of each bath was analyzed using ICP and the results are shown in Table 3-3. In addition, the Zn-Al-Fe-Sb phase diagram was assessed using the FactSage 6.1 software.

Table 3-3. Chemical analysis of the zinc baths (wt%)

Zinc bath \ Element	Al	Sb	Fe
No. 1	0.204	-	0.014
No. 2	0.188	0.012	0.015
No. 3	0.198	0.033	0.014
No. 4	0.196	0.098	0.015
No. 5	0.196	0.193	0.014

3.2. McMaster Galvanizing Simulator

Based on the experimental matrix, hot-dip galvanizing simulations were conducted on each steel panel using the McMaster Galvanizing Simulator (MGS). The machine set up and schematic are illustrated in Figures 3-2(a) and (b), respectively. Also, Figure 3-3 shows the thermal cycle that was carried out for dipping experiments. Prior to insertion in MGS, the steel panel was wiped with acetone and a 0.5 mm K-type control thermocouple was welded to the top surface of the panel (Figure 3-1). Once it was prepared, the panel was inserted into the sample chamber such that the longitudinal axis of the panel was parallel to the rolling and dipping directions. The panel was heated to 750 °C and annealed at this temperature for 120 s in the infrared furnace. Next, the panel was cooled to the bath temperature of 460 °C and held isothermally for 10 s. After

annealing, dipping was performed for 4 s in each molten zinc alloy bath. The sample was withdrawn, wiped with N₂ gas and cooled to room temperature at 10, 1 or 0.1 °C/s cooling rate. All dipping experiments were carried out under a N₂-5%H₂ atmosphere and the dew point (pO₂) was kept constant at -30 °C. The coated area for all panels was 120 mm by 160 mm as is shown in Figure 3-1. For all the required characterization and analysis throughout this study, the middle area of 90 mm by 90 mm on each panel was sectioned. This area was the usable coated region where the temperature and coating weight were known to be uniform.

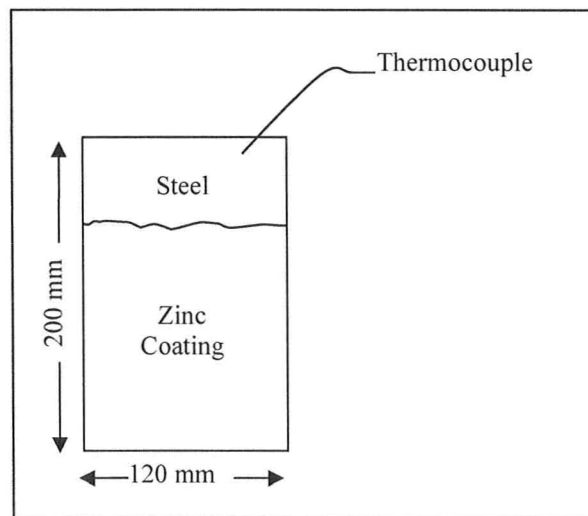


Figure 3-1. Coated steel panel

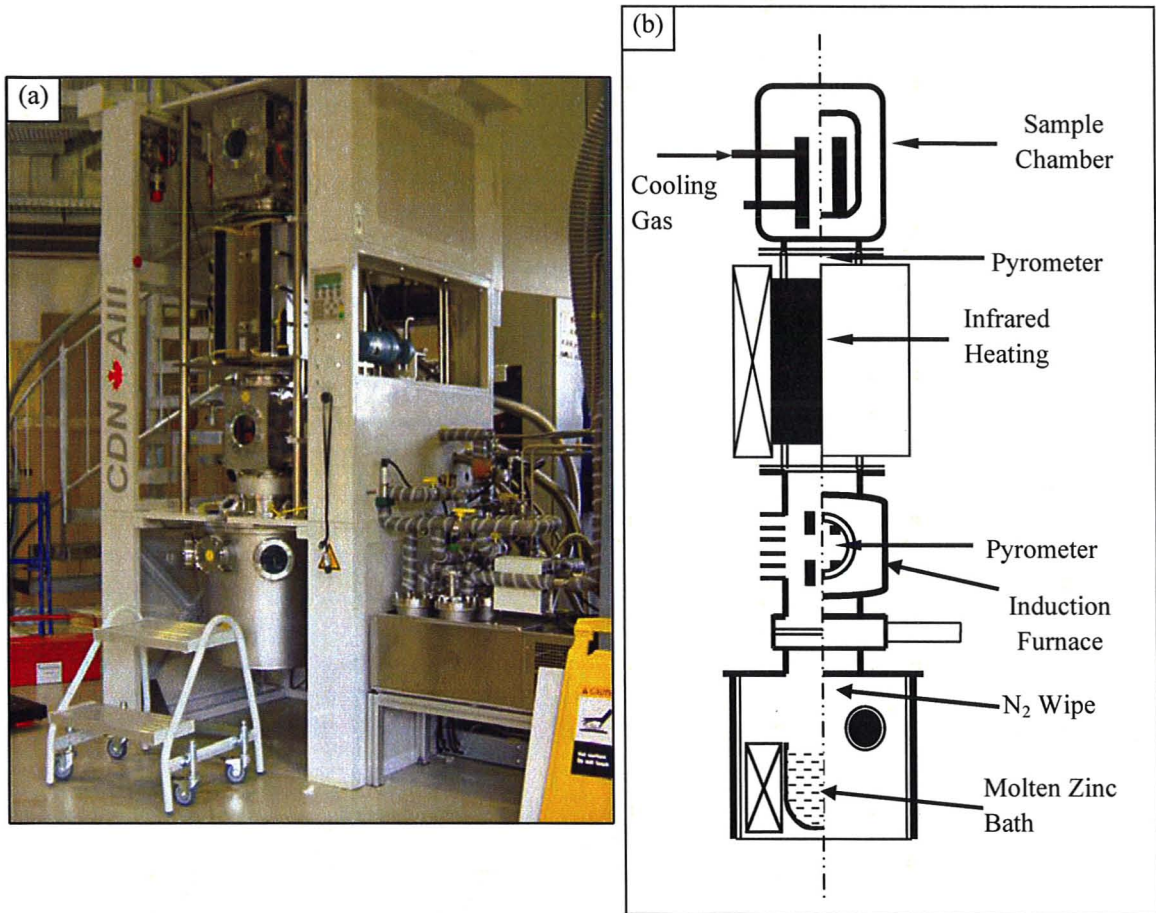


Figure 3-2. (a) Image and (b) schematic of McMaster Galvanizing Simulator (MGS)

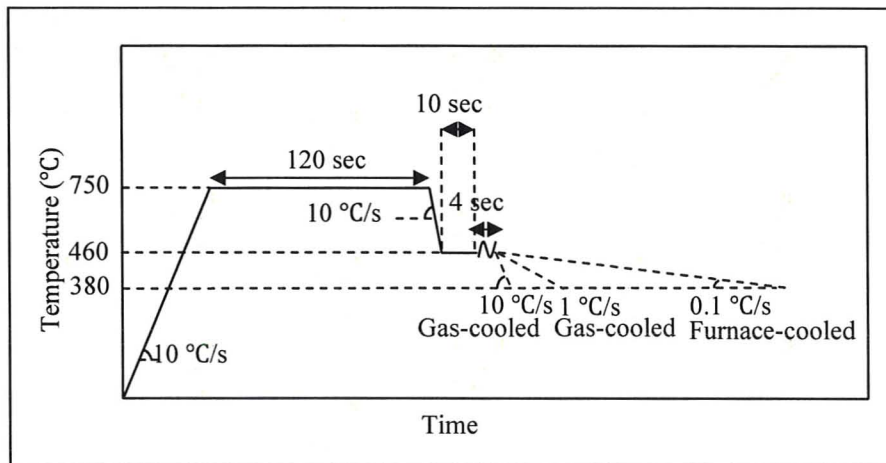


Figure 3-3. Heat treatment cycle for dipping experiments

3.3. Coating Weight

The coating weight was measured for each panel according to ASTM A90/A 90M - 01 [ASTM standards 2001]. A 20 mm by 10 mm rectangular sample was cut from the uniform coating zone of each coated panel and the initial weight of the sample was measured to the nearest 0.01 g. Next, the sample was dipped into 10% hydrochloric acid for approximately 15 s to dissolve the zinc overlay. Once the release of hydrogen gas bubbles stopped, the sample was rinsed in running water and dried with warm air. The sample mass was measured again and calculations were carried out in order to obtain the average coating weight in g/m^2 . For all coated panels, the average coating weight was approximately $140 \text{ g/m}^2/\text{side}$ or roughly a coating thickness of 20 microns per panel side.

3.4. Surface Roughness Measurements

In order to study the effect of the steel surface roughness on the solidification of zinc coatings, surface roughness measurements were carried out on the as-annealed BR and HR steel panels. Three panels of each steel type were annealed per the standard thermal cycle (Figure 3-3) in the MGS and the surface roughness of each panel measured using a Zygo white light optical interferometer and MetroPro 8.1.5 program. Measurements were performed over 40 field spots on the as-annealed surface of each panel. The spot size was 0.27 mm by 0.37 mm. Figures 3-4(a) and (b) show the roughness maps of the as-annealed surface for the BR and HR steel panels, respectively. Also, 3D models of the surface topography for each substrate are shown in Figure 3-5(a) and (b). Significant differences can be seen in the surface topography of these two surfaces. On

the BR surface, the topography was aligned with the rolling marks while for the HR surface, topography was relatively random. The average surface roughness (Ra) over all fields was 20 nm for the as-annealed BR steel surface and 420 nm for the as-annealed HR steel surface which was approximated by the roughness through the gas-jet wiping gap [McDermid 2009].

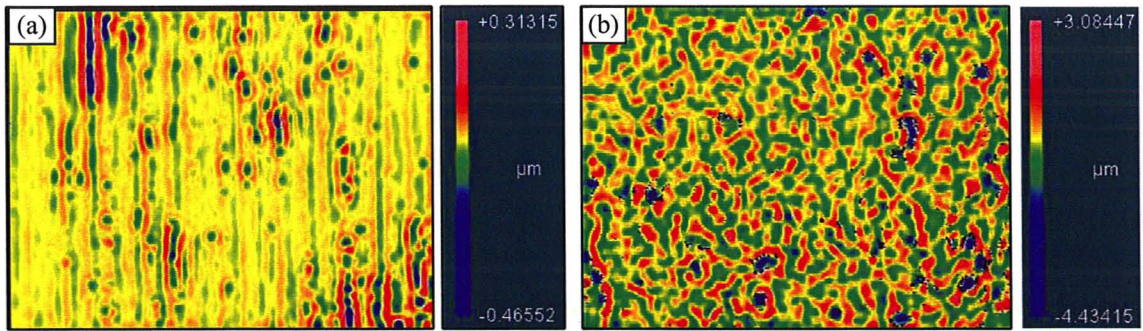


Figure 3-4. Surface roughness maps taken from (a) BR and (b) HR as-annealed steel

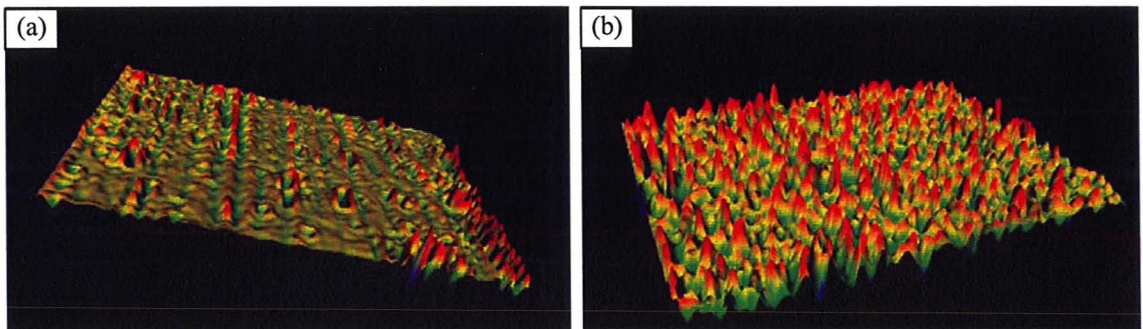


Figure 3-5. 3D model of surface roughness for (a) BR and (b) HR as-annealed steel

3.5. Metallography

3.5.1. Coating Surfaces

Zinc is a relatively soft material and as a result, the coating surface was scratched easily during storage. To minimize these scratches, the coating surface was hand-polished with a dilute colloidal silica solution on a MD-MOL cloth for 60 seconds. The surface was rinsed and ultrasonically cleaned in anhydrous ethyl alcohol for 15 s. The samples

were etched using 1% Nitric acid for a few seconds. After etching, the sample was rinsed off and ultrasonically cleaned in anhydrous ethyl alcohol for 15 s and dried in a warm air stream. All optical micrographs were taken such that the steel rolling direction (RD) is horizontal and transverse direction vertical in all images.

3.5.2. Coating Cross-sections

There were a number of difficulties encountered in the metallography of the coating cross-sections. Due to the difference in hardness of the zinc coating and steel substrate, the outer zinc-rich layer was ground off more rapidly than the steel substrate and thus, it was difficult to retain the coating and steel at equal levels in the mount media. The coating was also susceptible to cracking during grinding since it does not have sufficient ductility. Also, the coating edges can become rounded easily during polishing. Regarding etching, zinc is anodic compared to steel and is corroded rapidly in acidic solutions. As a result, etching time should be rather short or the etchant should be dilute. Furthermore, zinc coatings react with water quickly and thus, using water was prohibited during metallographic preparation, particularly after grinding. Finally, if the coating contained either Pb or Sb pure particles, these precipitates can be embedded in interdendritic regions and could easily be pulled out of the coating during grinding or polishing and create holes in the coating microstructure [Dionne 2006].

In order to prepare acceptable zinc coating cross-section, the detailed metallography procedure, outlined in Appendix A was followed [Jordan 1993] [Kilpatrick 1991]. Samples were etched using a mixture of 6 g picric acid + 100 mL ethanol + 5 mL

acetic acid + 10 mL water per the procedure in Appendix A until the coating grain boundaries were visible via optical microscopy.

3.6. Characterization Techniques

A number of characterization techniques were used to analyze the samples. For microstructural observations, optical microscopy and Scanning Electron Microscopy (SEM) were carried out both on the surface and cross-section of the samples. The JEOL-7000F SEM was operated using an acceleration voltage of 10 keV, probe current of 10 nA and working distance of 10 mm. Depending on the type of observations, the microscope was operated in either secondary electron or backscattered electron mode. Prior to insertion in the microscope, the sample surface was cleaned with plasma sputtering for 5 minutes.

Electron Backscattered Diffraction (EBSD) was used in conjunction with SEM to investigate the crystallographic texture of the surface and cross-section of coated samples as well as the chemical composition of intermetallic phases. The microscope was operated using an acceleration voltage of 20 keV, probe current of 13 nA and working distance of 18.4 mm for these analyses. Furthermore, HKL Channel 5 software was used to calculate the orientation distribution of the zinc grains over a minimum number of 10 fields. In $\{0002\}$ pole plots, Multiple Uniform Distribution (MUD) of poles was plotted as a function of the inclination angle of basal planes.

To study the intermetallic compounds present on the coating surface, Scanning Auger Microscopy (SAM) was performed using a JEOL JAMP-9500F Field Emission

Auger Microprobe. The conditions for SAM were acceleration voltage of 15 keV, probe current of 10 nA and working distance of 25 mm. The surface of each sample was first sputtered with Argon for 20-30 s prior to point analysis or elemental mapping. The sputtering conditions were an acceleration voltage of 2 keV, probe current of 20 mA and the sputtering rate was 15 nm/min. Also, some of the SAM analysis was carried out using a PHI 700Xi Scanning Auger Nanoprobe. The SAM conditions were acceleration voltage of 10 keV and 20 keV, probe current of 10 nA and 1 nA. Also, the sample was tilted by 10° from the surface normal to the electron gun. The Ar ion beam condition for sputter etching was acceleration voltage of 500 keV and the sample was tilted for 62° from the surface normal to the ion gun. For all the SAM mappings, secondary electron imaging (SEI) was used to locate the area of interest for SAM analysis. In addition, Transmission Electron Microscopy (TEM) was carried out on the coatings using a Philips CM12 at an acceleration voltage of 200 keV to analyze the intermetallic phases. TEM samples were prepared using Focused Ion Beam (FIB) milling using a NVision 40 by Zeiss.

3.7. Grain Size Measurements

Using Clemex 5.0 image analysis software, grain size measurements were carried out on each coating surface using the line intercept method [Chalmers 1964]. Grain size measurements were repeated over 40 randomly selected fields on each side of the samples considering 10 lines per field. The average grain size for the sample was calculated by averaging all the grain size values obtained for the fields within the 95% confidence interval.

CHAPTER 4. RESULTS

4.1. 0 wt% Sb Alloy

4.1.1. Coating Surface Microstructure

Optical micrographs of the surface of the coated BR and HR steel substrates at the 10 °C/s, 1 °C/s and 0.1 °C/s cooling rates for the 0 wt% Sb addition are shown in Figures 4-1(a-f). All coatings are in the as-cast condition and no metallographic preparation was carried out on the surface.

Figures 4-1(a-c) show the coating microstructure of the BR steel substrate cooled at 10 °C/s, 1 °C/s and 0.1 °C/s, respectively. A transition from planar to dendritic microstructure can be seen in Figures 4-1(a-c). The coatings consisted of nearly equiaxed zinc grains with a bright appearance at all cooling conditions. The cross-section of the primary arm can be seen at the center of each grain while the secondary arms grew out of the trunk in the six $\langle 10\bar{1}0 \rangle$ crystallographic fast growth directions laterally, as illustrated in Figure 4-2(a). Also, the projections and depressions in the inter-dendritic areas appeared as topographic features which have been annotated in Figure 4-2(a).

Optical images of the coating microstructure on the HR steel substrate at 10 °C/s, 1 °C/s and 0.1 °C/s cooling rates are illustrated in Figures 4-1(d-f), respectively. As can be seen, the zinc grains had an irregular shape with a dark appearance and did not exhibit clear internal dendritic structures. In addition, several topographic features and small pits were detected within the coating microstructure which were likely due to the surface roughness of the HR steel substrate (Figure 4-2(b)).

On both substrates, the coating surface exhibited curvature at the grain boundaries which appeared as dark grooves in optical images at all cooling conditions. Figures 4-3(a) and (b) show the SEM-SEIs of the grain boundary openings on coated BR and HR steels at 10 °C/s, respectively. As was already mentioned, the volume shrinkage during solidification, liquid pull-over at grain boundary regions, thermal stress during quenching as well as thermal residual stress may result in the formation of cracks and grooves at grain boundary regions [Fasoyinu 1993] [Jordanova 1004]. Furthermore, grain size measurements showed that the coating grain size was the smallest for the 10 °C/s cooling rate on BR and HR steel substrates due to the higher driving force for nucleation for the faster cooling rates (Figure 4-4).

The coated BR steel surface had a brighter appearance as compared to the coated HR steel surface. In addition, zinc grains were smaller on the HR steel substrate with respect to the BR steel substrate at 10 °C/s and 1 °C/s cooling rates while zinc grains were about the same size on both substrates at 0.1 °C/s as shown in Figure 4-4. Presumably, nucleation occurred on the steel surface. Based on the surface roughness measurements, the average surface roughness of the as-annealed HR steel was higher and, therefore, the nucleation rate was higher on this surface which resulted in the formation of smaller zinc grains.

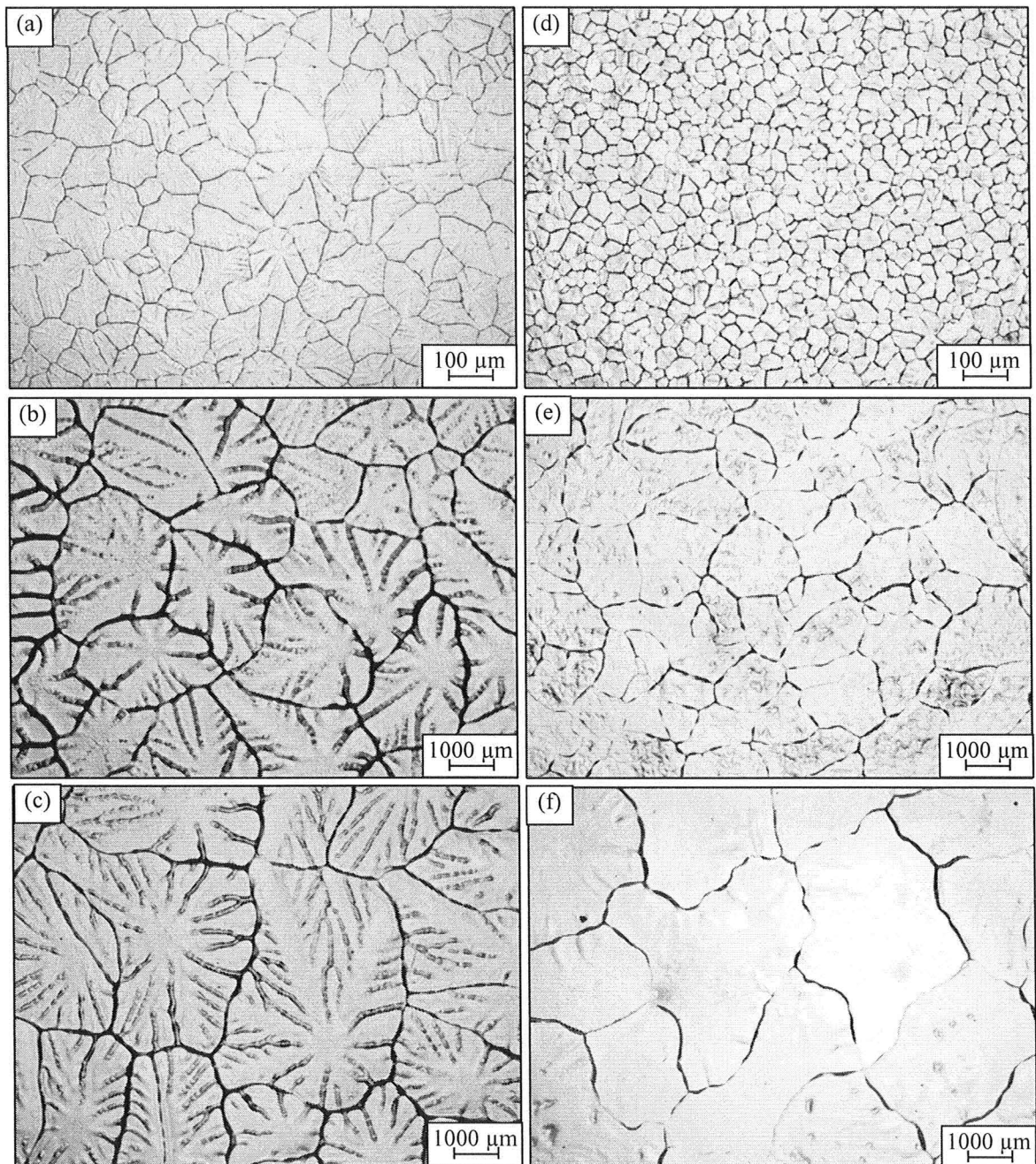


Figure 4-1. Optical micrographs of the as-cast coating surface containing 0 wt% Sb on BR steel cooled at (a) 10 °C/s (b) 1 °C/s (c) 0.1 °C/s and on HR steel cooled at (d) 10 °C/s (e) 1 °C/s (f) 0.1 °C/s

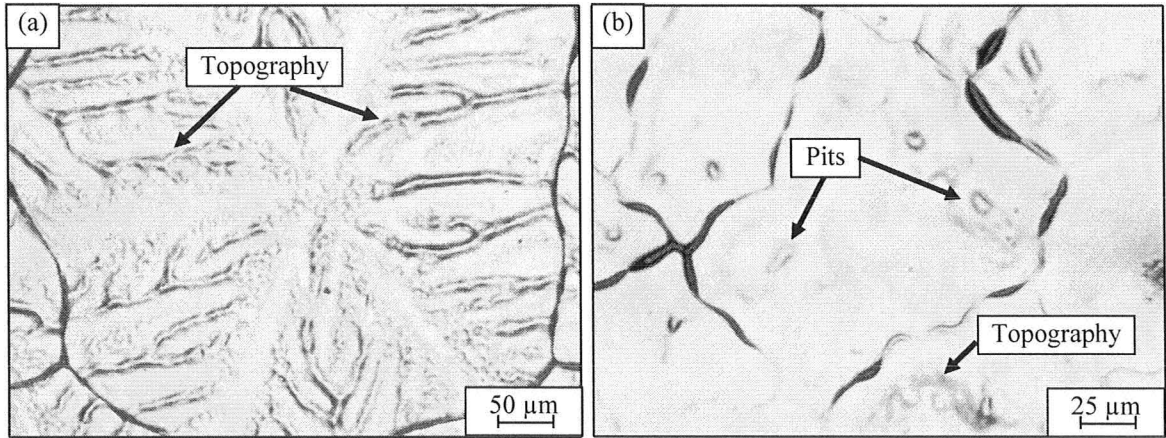


Figure 4-2. Optical micrographs of a single zinc grain on a coated (a) BR and (b) HR steel cooled at 0.1 °C/s

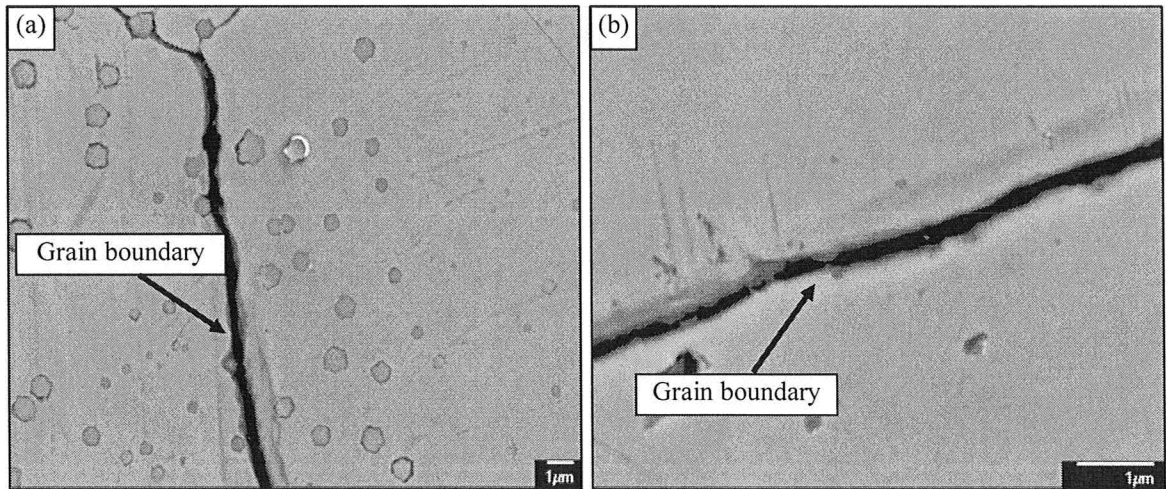


Figure 4-3. SEM-SEIs of the grain boundary openings on a coated (a) BR and (b) HR steel cooled at 10 °C/s

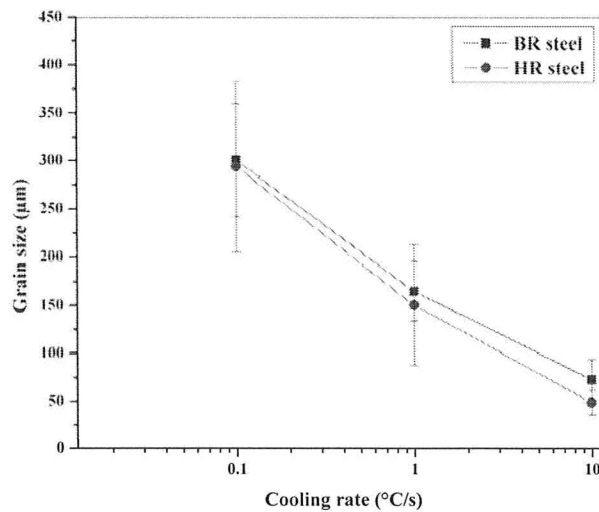


Figure 4-4. Grain size vs. cooling rate for the BR and HR steels

4.1.2. Coating Cross-section Microstructure

As discussed previously, the undercooling present across the liquid zinc layer at the onset of coating solidification was insufficient for the homogeneous nucleation of zinc and, therefore, depending on the process conditions, zinc nuclei could have formed heterogeneously on either the $\text{Fe}_2\text{Al}_5\text{Zn}_x$ /molten zinc interface, molten zinc/air interface or within the liquid zinc layer [Strutzenberger 1998] [Poulon-Quintin 2004]. In order to study the nucleation and growth mechanism of zinc grains during the coating solidification, optical microscopy was performed on coating cross- sections.

➤ **BR steel**

An optical micrograph of a coating cross-section of the BR steel substrate cooled at 10 °C/s is shown in Figure 4-5. It was found that the zinc overlay on the BR steel substrate was made up of two distinct layers. Considering the geometry of these grains, the base of each grain had a larger area at either the $\text{Fe}_2\text{Al}_5\text{Zn}_x$ or air interface as compared to the other end of the grain which was located further within the coating thickness as can be seen in Figure 4-5.

In order to explore the coating grain size and orientation distribution, a number of EBSD measurements were carried out on individual grains which were located in either the first or second coating layer. Figure 4-6(a) shows the SEM-SEI image of two grains. Based on the above argument, it is claimed that grain #1 nucleated at the $\text{Fe}_2\text{Al}_5\text{Zn}_x$ /coating interface while grain #2 nucleated at the coating/air interface. The Euler orientation colour map exhibits two different Euler colours which represent two

distinct orientations for the grains (Figure 4-6(b)). The acquired pole figures and {0002} pole plot confirmed that grain #1 had a basal crystallographic orientation while grain #2 was inclined 15° with respect to the substrate surface (Figures 4-6(c) and (d)). The presence of two distinct orientation distributions implies that the nucleation and growth conditions were different for the two grains. Furthermore, GDOES showed segregation of aluminum at the steel/zinc coating interface as well as at the coating/air interface, as illustrated in Figure 4-7. It has been reported that Al segregation is due to the presence of the $\text{Fe}_2\text{Al}_3\text{Zn}_x$ intermetallic layer at the steel/zinc coating interface and an aluminum oxide layer at the coating/air interface, respectively [Helwig 1981] [Leory 1980] [Kilbane 1982]. The aluminum oxide layer was likely formed at the molten zinc/air interface prior to the start of solidification since the dissolved Al in the zinc melt has a high affinity for oxygen in the air. Thus, in addition to the steel substrate, the aluminum oxide solid layer could provide heterogeneous nucleation sites for zinc grains. Particularly, this thin film may have become active at high cooling rates due to the high driving force for nucleation. The presence of two peaks in Figure 4-7 can be attributed to the steel surface roughness and non-uniform sputtering in the GDOES.

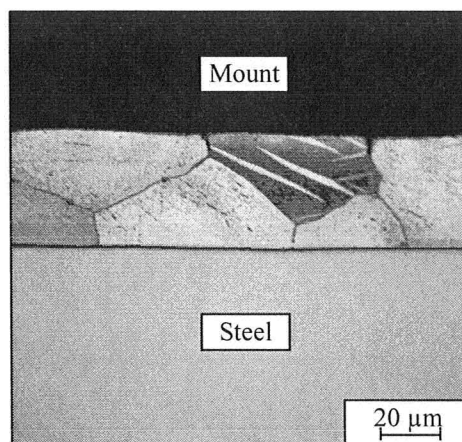


Figure 4-5. Optical micrograph of the coating cross-section on a BR steel substrate cooled at 10°C/s

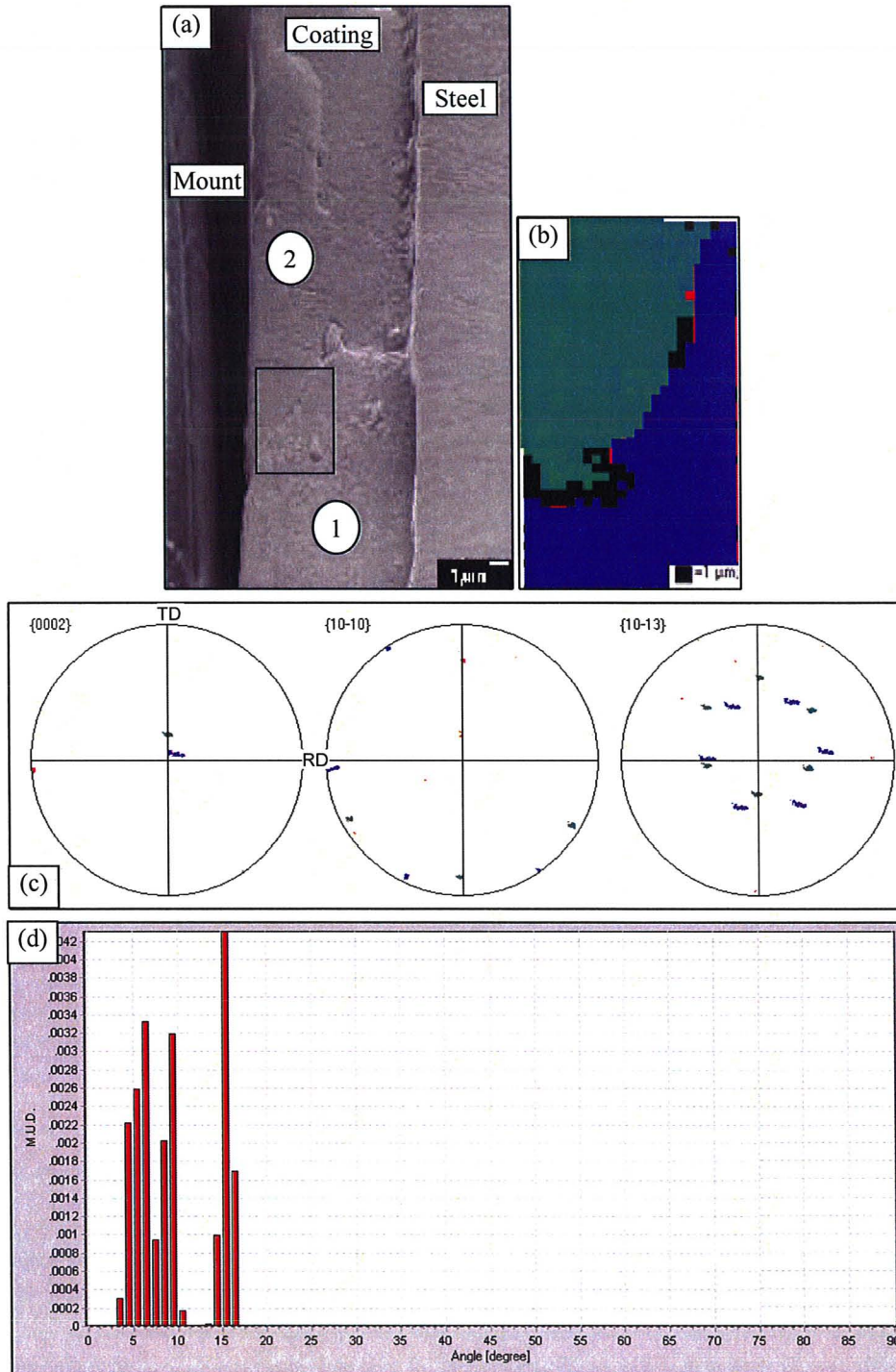


Figure 4-6. (a) SEM-SEI (b) Euler orientation colour map (c) pole figures and (d) {0002} pole plot of the coating cross-section on a BR steel substrate cooled at 10 °C/s

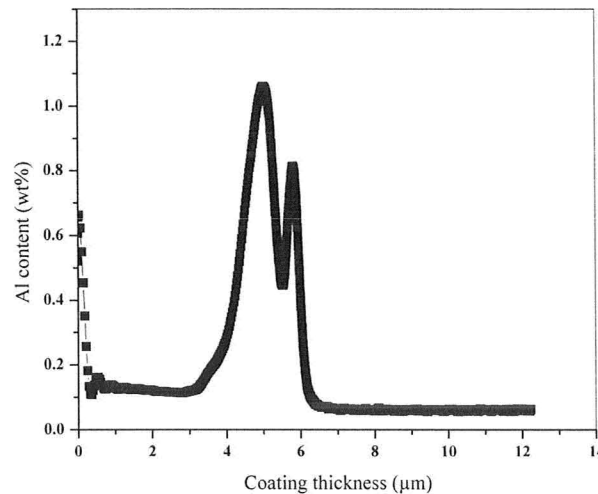


Figure 4-7. Al content as a function of coating thickness for coated BR steel substrate cooled at 10 °C/s

Thus, it is suggested that the grains present on the steel surface have been nucleated on the $\text{Fe}_2\text{Al}_5\text{Zn}_x$ /molten zinc interface while the grains present on the aluminum oxide surface have been nucleated on the molten zinc/air interface (Figure 4-5). Nucleation of zinc grains at both the substrate/coating and coating/air interface during thick coating solidification on thin substrate and at fast cooling rates has previously been reported by Cameron and Harvey [Cameron 1967]. Consequently, it is proposed that there were two active nucleation sites for the formation of zinc grains in the case of the coating on the smooth BR surface at 10 °C/s cooling rate.

Nucleation of zinc grains at the $\text{Fe}_2\text{Al}_5\text{Zn}_x$ /molten zinc interface and molten zinc/air interface was followed by three dimensional dendritic growth in the slightly undercooled melt [Dutta 2007]. The growth of primary dendrite arms along the normal direction to the substrate surface was limited due to the small coating thickness relative to the diffusion length of zinc atoms. However, secondary arms were rapidly formed in directions parallel to the crystallographic fast growth directions on the plane of the steel

substrate. Eventually, ternary arms grew out of the secondary arms and coating solidification was completed once the adjacent grains impinged on one another.

➤ **HR steel**

An optical micrograph of the cross-section of a zinc coating on the HR steel substrate cooled at 10 °C/s exhibited FeZn₁₃ columnar grains at the interface of steel/zinc coating as well as a number of equiaxed zinc grains present across the coating thickness, as shown in Figure 4-8. The inhibition breakdown was likely promoted by the higher energy of the rough HR surface and resulted in the formation of Fe-Zn intermetallic phases at the steel/zinc overlay interface.

According to the GDOES results, an aluminum oxide layer was present on the coating surface (Figure 4-9). However, it is proposed that preferential nucleation occurred at the coating/FeZn₁₃ interface since the driving force for nucleation was higher on the surface of the intermetallic phase due to the high surface roughness. As a result, it is more likely that the FeZn₁₃/molten zinc interface was the only active nucleation site at the beginning of solidification.

Once the FeZn₁₃ surface was covered with first layer of zinc grains, nucleation and three dimensional growth of the subsequent zinc grains continued until the last layer of zinc grains reached the coating/air interface.

It should be mentioned that similar results were found for the coatings on BR and HR steels cooled at 1 °C/s and 0.1 °C/s.

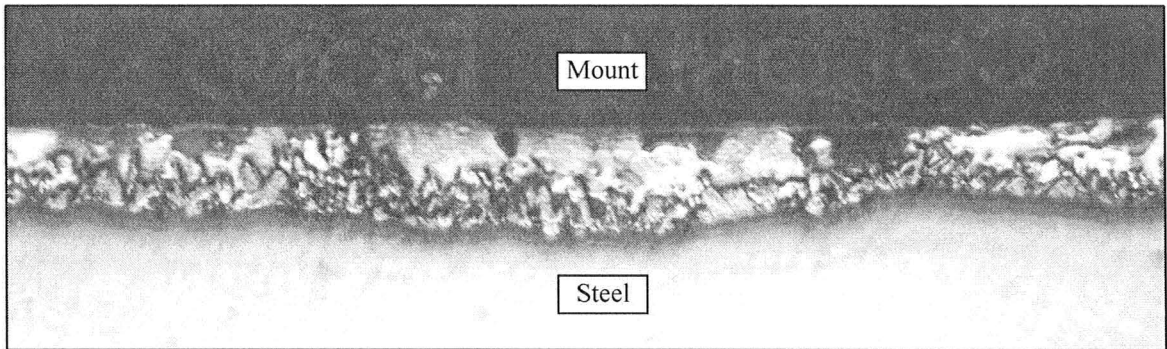


Figure 4-8. Optical micrograph of the coating cross-section on a HR steel substrate cooled at 10 °C/s

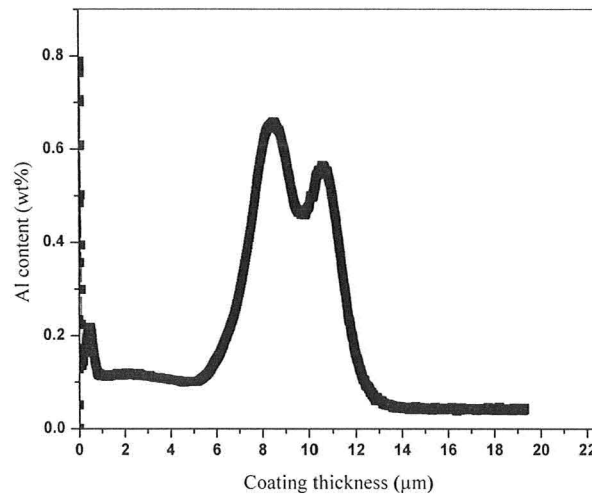


Figure 4-9. Al content as a function of coating thickness for coated HR steel substrate cooled at 10 °C/s

4.1.3. Coating Intermetallics

According to the experimental matrix shown in Table 3-1, the experimental zinc baths had varying contents of Sb, 0.2 wt% Al and minor amounts of impurities such as Cr, Ni, Sn and Pb. The baths were also Fe saturated. Most of these alloying elements have very low solubility in solid zinc and as a result may be rejected from the solid/liquid interface during coating solidification. Depending on the bath composition and cooling conditions, these solutes may form various intermetallic precipitates within the coating

[Sere 1999]. Figures 4-10(a-d) show the SEM-Backscattered Electron Images (SEM-BEIs) of the coating surface on the BR and HR steel substrates at the 0.1 °C/s cooling rate. The varying contrast between the particles and matrix in SEM-BEI implies that four phases were present in the coatings for both substrates. The zinc matrix with consistent grey contrast, small round particles with light grey contrast, particles with dark grey contrast and white spots were found on the coating surface as shown in Figure 4-10(a-d). It should be noted that the small round particles were detected within the zinc grains as well as at grain boundaries.

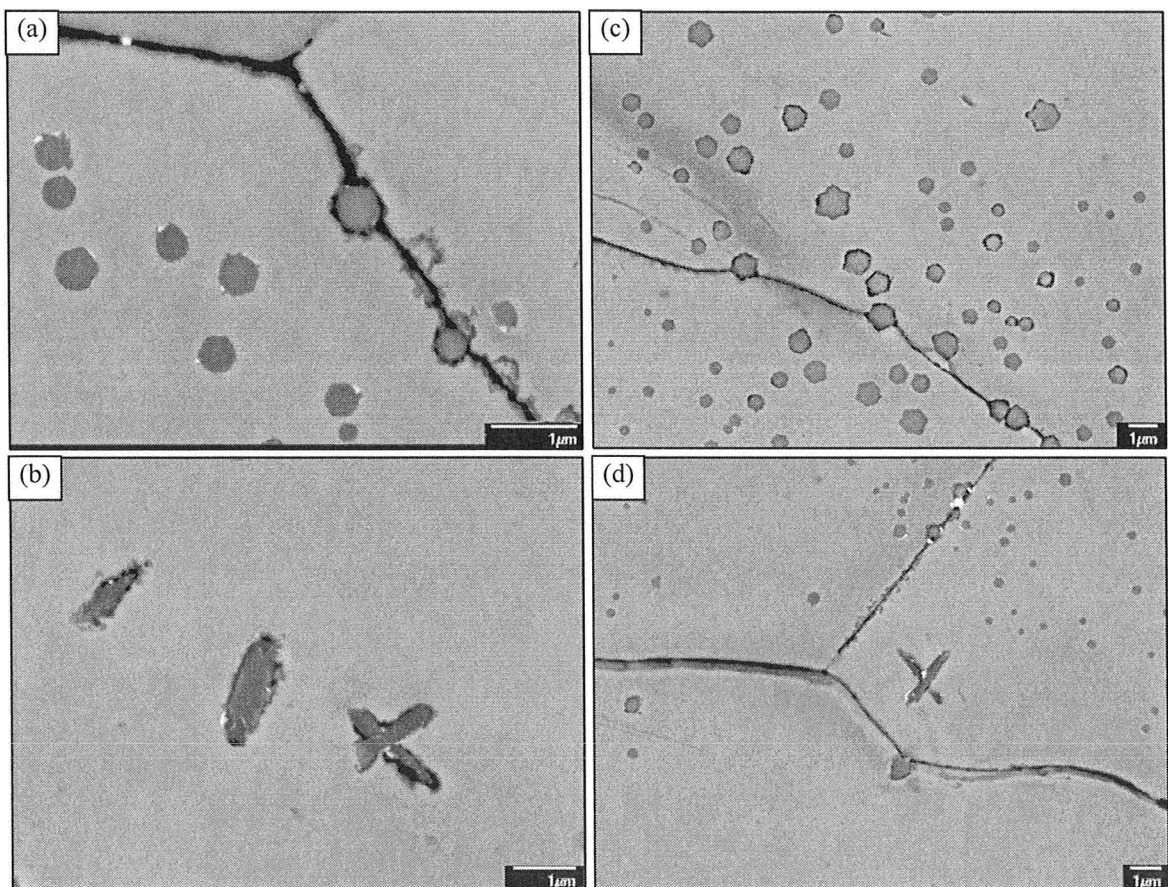


Figure 4-10. SEM-BEI of the coating surface on (a-b) BR and (c-d) HR steel substrate cooled at 0.1 °C/s

For the Auger analysis, a SEM-SEI was used to locate the areas of interest on a coated BR surface cooled at 0.1 °C/s. Two areas were chosen for the Auger mapping and point analysis. Prior to the analysis, the coating surface was sputtered with an Ar ion beam for 30 s to remove surface oxides and any contamination. The surface layer removed was approximately 3 nm thick.

The SEM-SEI and the corresponding Zn, Fe and Al Scanning Auger Microscopy (SAM) thermal pseudo colour elemental maps of the coating surface containing small round particles are shown in Figures 4-11(a-d), respectively. According to Figures 4-11(b-d), the small round particles contained Zn, Fe and Al. Furthermore, SAM point analysis was performed on the zinc matrix as well as intermetallic particles and the quantitative results are shown in Table 4-1. It was found that nearly 2 at% Al was dissolved in the zinc matrix. Regarding the amount of dissolved Al in the liquid zinc, it is likely that the Al in the aluminum oxide film present on the surface was partly analysed. Also, the small round particles mainly contained Zn and Al along with small quantities of Fe and Cr.

Figure 4-12(a) illustrates the SEM-SEI of the coating surface containing a dark grey particle. SAM elemental maps were collected for Zn, Fe and Al as shown in Figures 4-12(b-d), respectively. It was found that the intermetallic particle was composed of Al, Fe and small amount of Zn. In addition, small concentrations of Cr and Sn were detected in SAM quantitative analysis as shown in Table 4-1.

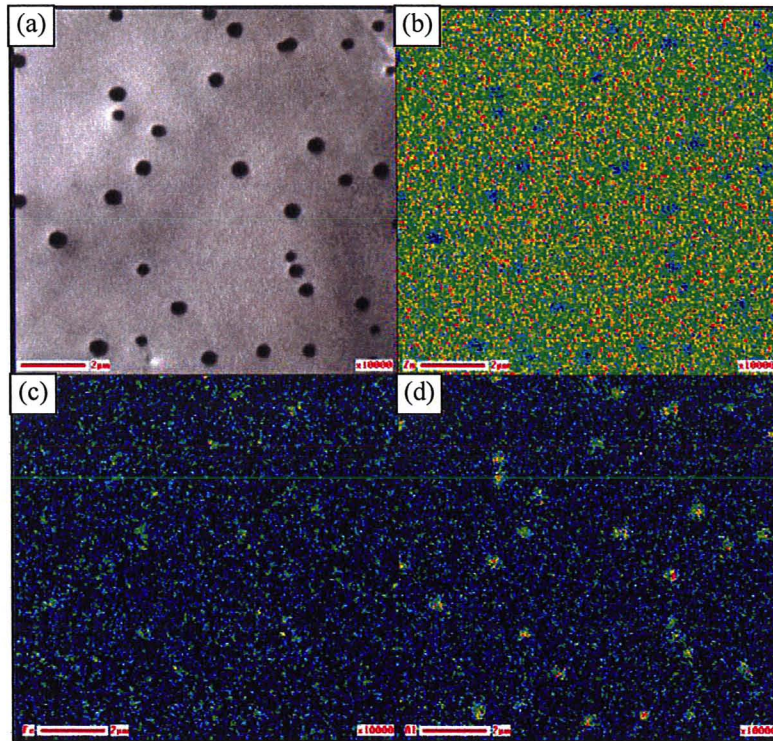


Figure 4-11. (a) SEM-SEI of the coated BR steel surface cooled at 0.1 °C/s containing round particles and (b) Zn (c) Fe and (d) Al SAM maps

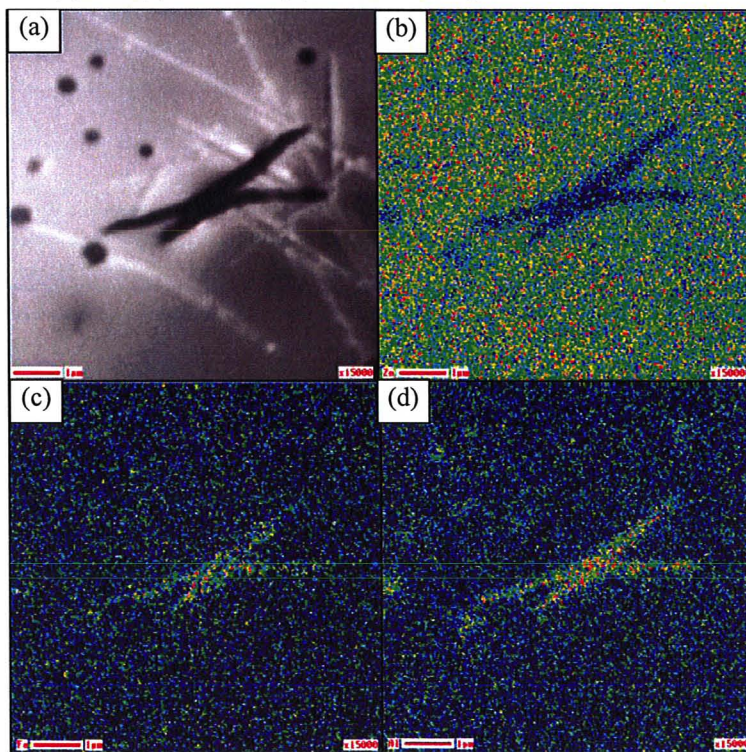


Figure 4-12. (a) SEM-SEI of the coated BR steel surface cooled at 0.1 °C/s containing star-like particle and (b) Zn (c) Fe and (d) Al SAM maps

Table 4-1. SAM point analysis of the different phases on coated BR steel cooled at 0.1 °C/s (at%)

Phase \ Element	Zn	Al	Fe	Cr	Sn
Matrix	98.1	1.9	-	-	-
Round	47	47.8	4.1	1.1	-
Dark grey	11.1	69.5	16.6	1.5	1.4

Based on the microstructural observations and SAM results, it was concluded that two types of intermetallic phases were present on coatings containing 0 wt% Sb on BR and HR steel substrates for all cooling conditions. Zn, Al, Fe and small quantities of both impurities such as Cr and Sn were detected in both intermetallic particles.

4.1.4. Coating Crystallographic Texture

Based on the previous microstructural observations, it was deduced that zinc grains tend to have dendritic structures on the BR steel substrate and non-dendritic structures on the HR steel substrate at all cooling rates. The fact that most of the zinc grains had a hexagonal shape with 6-fold symmetry on the BR steel substrate implies that these crystals solidified such that the {0002} basal planes were aligned parallel to the steel sheet surface whereas the basal texture was not dominant in the case of the coated HR steel substrate. EBSD was used to find the coating crystallographic texture as a function of coating cooling rate. It should be mentioned that there were no significant differences in EBSD results in the case of samples cooled at 1 °C/s as compared to the samples cooled at 0.1 °C/s. The EBSD data were collected for at least 10 grains for all samples through the EBSD study and only a portion of the analysed area is presented

herein. However, the pole figures and $\{0002\}$ pole plots exhibit the data for the entire examined area.

The microstructural maps, Euler orientation colour maps, pole figures and $\{0002\}$ pole plots for coatings on BR substrates cooled at 10 °C/s and 0.1 °C/s are illustrated in Figures 4-13(a-d) and 4-14(a-d), respectively. Clearly, the coatings had a strong preferred crystallographic orientation along the $\langle 0001 \rangle$ direction and a random crystallographic orientation along the $\langle 10\bar{1}0 \rangle$ and $\langle 10\bar{1}3 \rangle$ directions for both cooling conditions (Figures 4-13(c) and 4-14(c)). Also, the $\{0002\}$ pole plots showed an average inclination of 10-20° for the $\{0002\}$ planes with respect to the steel sheet surface for both cooling rates (Figures 4-13(d) and 4-14(d)). No significant differences were detected in the coating orientation distribution with changes in cooling rate.

The orientation distribution of the coating was also investigated for the coated HR steel substrates as a function of cooling rate. The corresponding microstructural maps, Euler orientation colour maps, pole figures and $\{0002\}$ pole plots for coatings cooled at 10 °C/s and 0.1 °C/s are shown in Figures 4-15(a-d) and 4-16(a-d), respectively. Based on the $\{0002\}$ pole figures, the coatings exhibited a very weak basal crystallographic texture at 10 °C/s and 0.1 °C/s cooling rates (Figures 4-15(c) and 4-16(c)). Also, the $\{0002\}$ pole plots showed a wide distribution of inclination angle for $\{0002\}$ planes with respect to the steel surface plane for both cooling rates (Figures 4-15(d) and 4-16(d)). The fact that coatings on HR substrates did not exhibit a strong basal crystallographic texture at 10 °C/s and 0.1 °C/s cooling rates is mainly due to the surface roughness of the HR steel substrate.

In conclusion, the zinc coating solidification for the 0 wt% Sb addition was essentially dendritic with preferred crystallographic growth directions along the $\langle 10\bar{1}0 \rangle$ and $\langle 0001 \rangle$ directions on both substrates. However, due to surface roughness, the coating showed a strong basal texture for BR substrate whereas the coating exhibited a more random texture on the HR substrate. Consequently, dendritic structures could be observed on the surface of the coated BR steel while no dendritic structures were detected on the surface of the coated HR steel (Figures 4-1(a-f)).

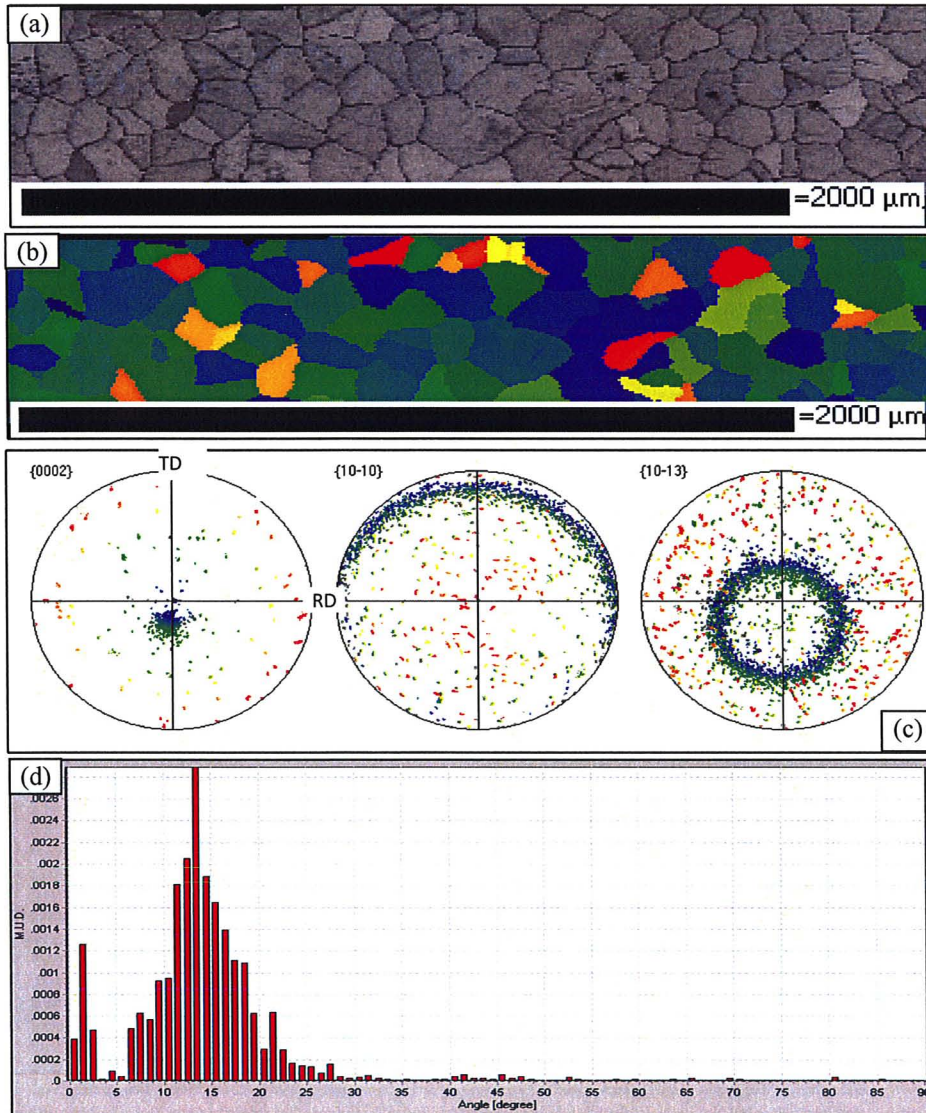


Figure 4-13. (a) Microstructural map (b) Euler orientation colour map (c) pole figures and (d) $\{0002\}$ pole plot of a cooled BR substrate cooled at 10 °C/s

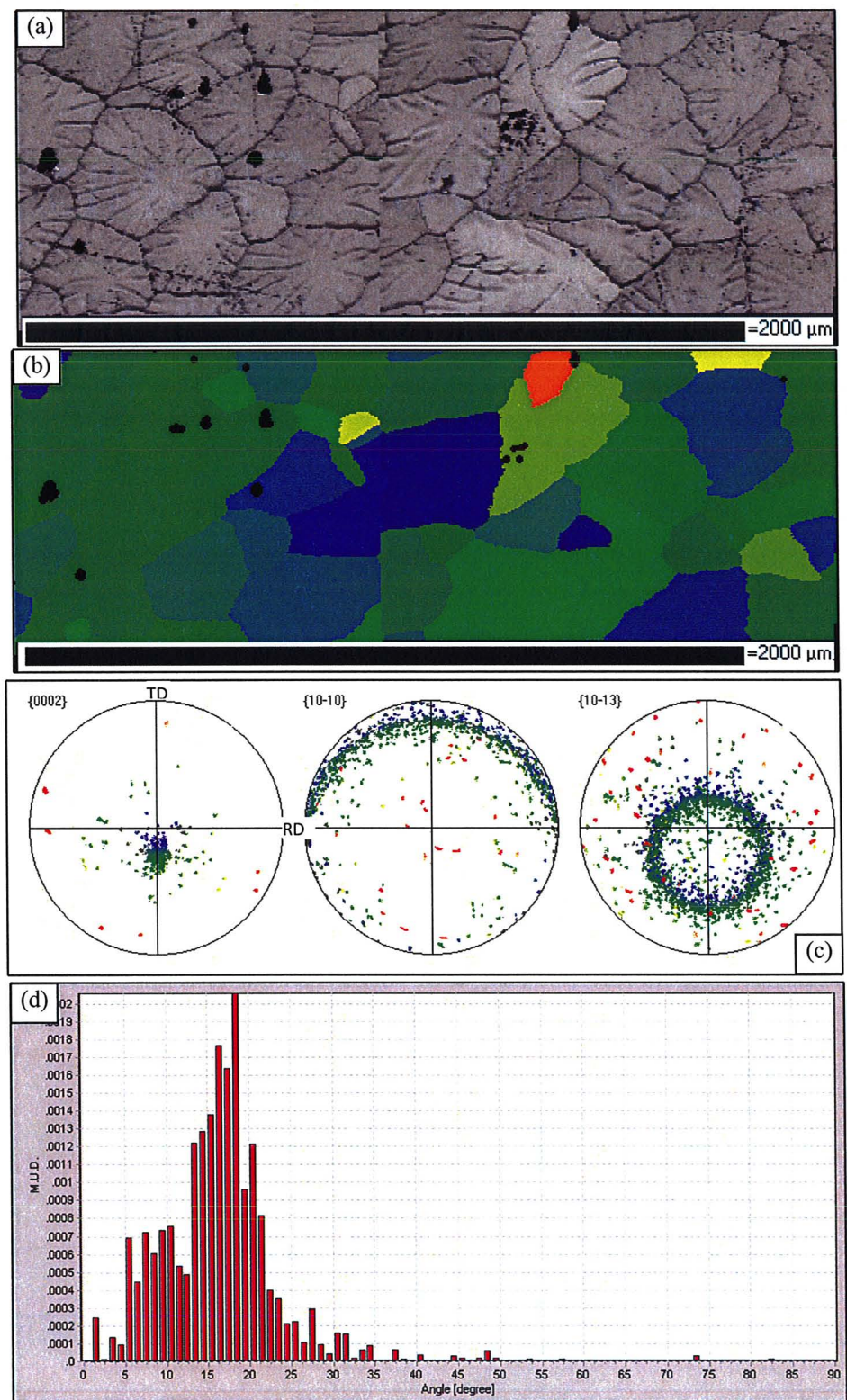


Figure 4-14. (a) Microstructural map (b) Euler orientation colour map (c) pole figures and (d) {0002} pole plot of a cooled BR substrate cooled at 0.1 °C/s

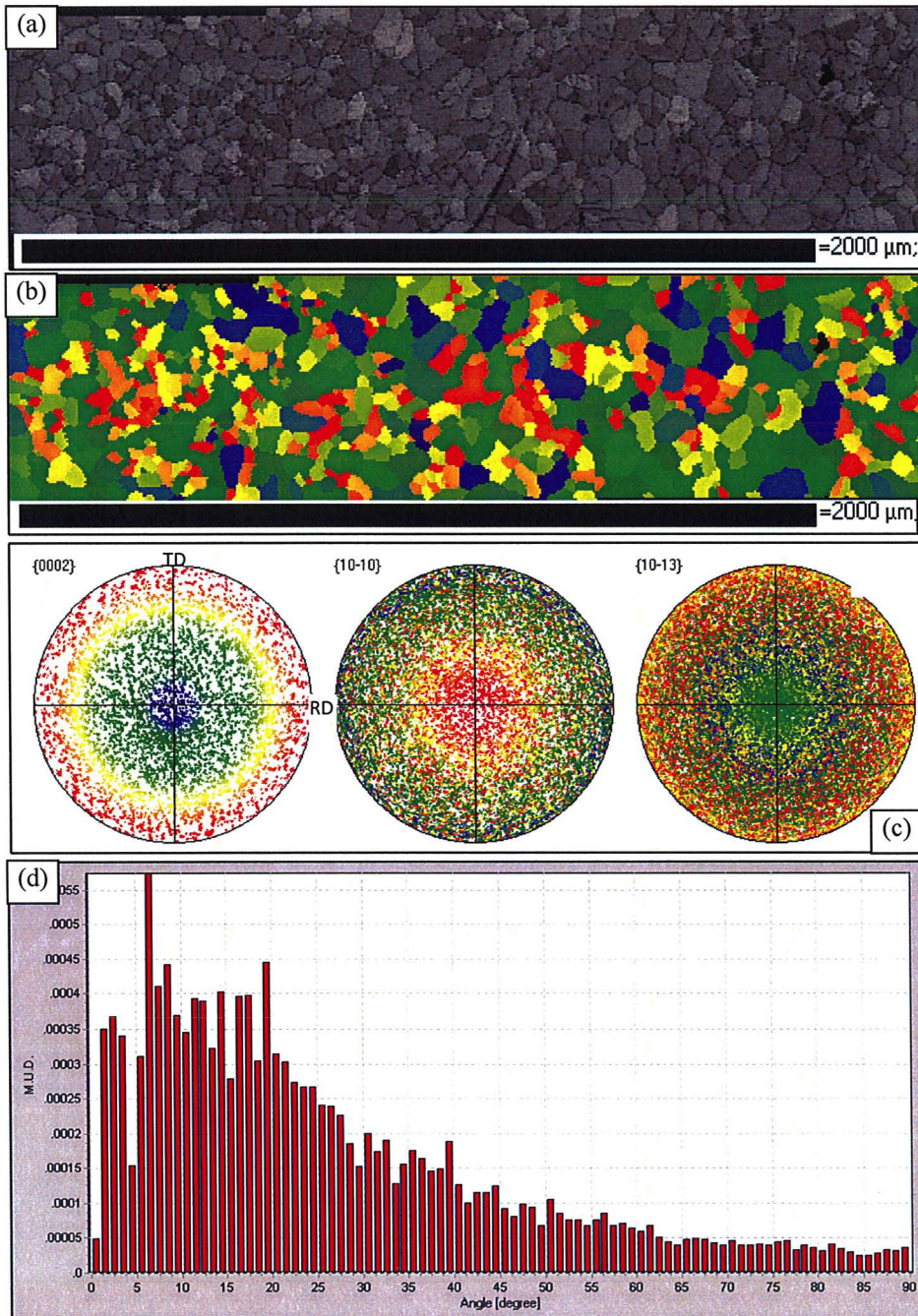


Figure 4-15. (a) Microstructural map (b) Euler orientation colour map (c) pole figures and (d) {0002} pole plot of a cooled HR substrate cooled at 10 °C/s

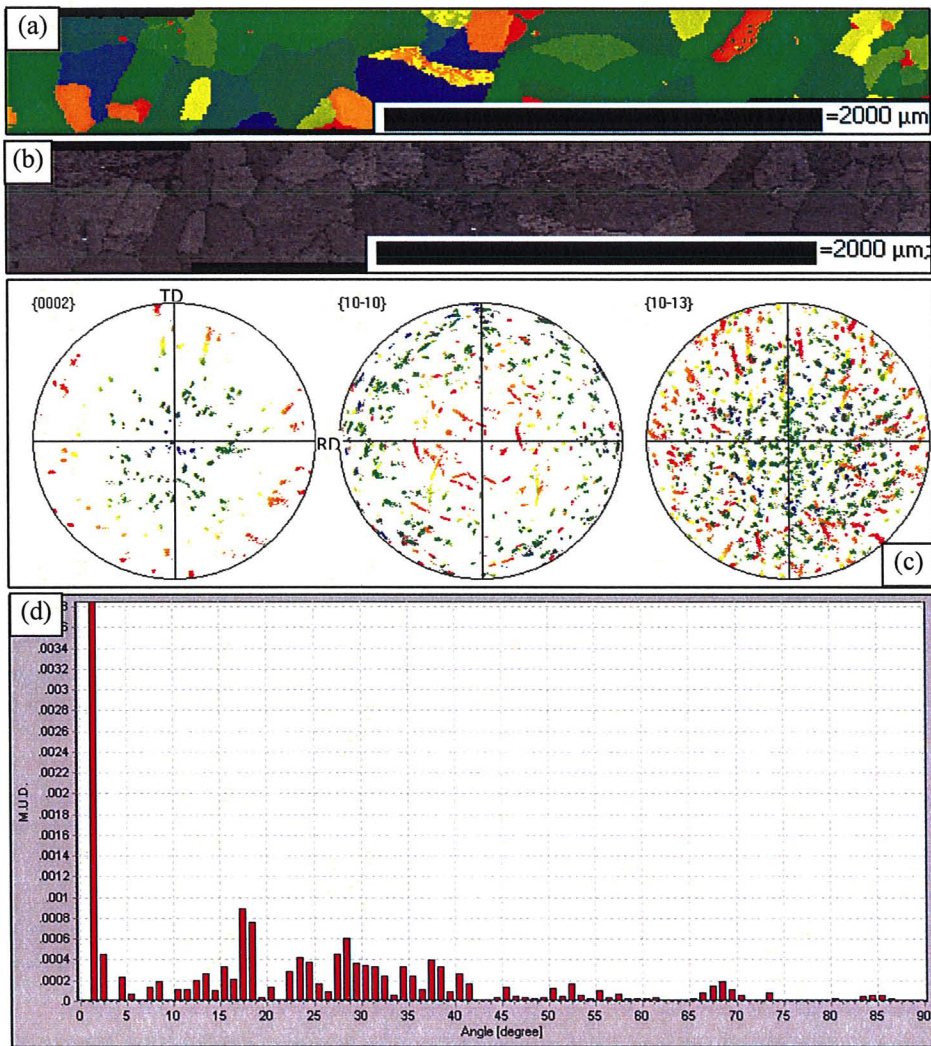


Figure 4-16. (a) Microstructural map (b) Euler orientation colour map (c) pole figures and (d) {0002} pole plot of a cooled HR substrate cooled at 0.1 °C/s

Table 4-2. Area percentage of basal zinc grains inclined for 0-15° relative to the steel sheet (%)

	Cooling rate (°C/s)	
Steel substrate	10	0.1
BR	30.2	25.1
HR	13.4	6.5

4.2. 0.01 wt% Sb Alloy

4.2.1. Coating Surface Microstructure

It has been reported that the presence of small amounts of Sb in the liquid zinc bath produces large zinc spangles on the coating surface [Fasoyinu 1990] [Jin-Tang 2007] [Marder 2000]. According to the experimental matrix shown in Table 3-1, the first addition to the molten zinc bath was 0.01 wt% Sb. The corresponding optical micrographs of the as-cast coating microstructure on the BR and HR steel substrates for the three cooling conditions are illustrated in Figures 4-17(a-f).

Figures 4-17(a-c) illustrate the coating microstructure of the BR steel substrate cooled at 10 °C/s, 1 °C/s and 0.1 °C/s, respectively. As was expected, the coating consisted of flowery zinc spangles with a relatively bright appearance and delineated internal dendritic structures for all cooling conditions. Most of the spangles exhibited 6-fold symmetry with primary dendrite arms radiating from the central point of each grain along the six $\langle 10\bar{1}0 \rangle$ crystallographic fast growth directions of the hexagonal crystal [Cameron 1964]. Macroscopically, each spangle was made up of white and black segments. White areas had dendritic structures and a bright appearance while black areas had non-dendritic structures and a dark appearance as shown in Figures 4-18(a-c).

Following the Strutzenberger classification, shiny, feathery, dimpled, ridged and orthogonal dendritic morphologies were found on the BR coating surface and are shown in Figures 4-19(a-e) [Strutzenberger 1998]. Higher magnification optical micrographs of the bright and dark regions are shown in Figures 4-20(a-c). In comparison, the bright

areas were relatively free of intermetallic precipitates and topographical depressions while the dark regions contained a number of intermetallic particles as well as distinct topographic features. Thus, it was concluded that the presence of intermetallic phases as well as high surface topography resulted in a dark coating appearance.

For the HR steel, the coating microstructure for the 10 °C/s, 1 °C/s and 0.1 °C/s cooling rates are shown in Figures 4-17(d-f), respectively. No zinc spangles were detected on the coated HR steel for all cooling conditions. Instead, similar to the coating containing 0 wt% Sb, the coating microstructure consisted of irregular zinc grains with a relatively dark appearance. In addition, the zinc grains exhibited dendritic structure in the case of 10 °C/s cooling rate as shown in Figure 4-18(d) and non-dendritic structures in the case of 1 °C/s and 0.1 °C/s cooling rates, as shown in Figure 4-18(e) and (f). For all cooling conditions, the coating had a dull morphology due to the presence of intermetallic precipitates and topographical features on the coating surface as shown in Figures 4-18(e) and (f).

For all cooling rates, grooves and openings at grain boundaries separated adjacent zinc spangles or zinc grains on both the coated BR and HR steels. Also, the smallest zinc grain size was observed for the fast cooled coating on both substrates as shown in Figure 4-21.

In comparison, the BR coatings were smoother and, thus, brighter than the comparable HR coating. Furthermore, the coating surface on the BR substrate exhibited a variety of morphologies such as shiny, feathery, dimpled, ridged and orthogonal-dendritic while the coating surface on the HR substrate only exhibited a dark appearance.

Regarding the spangle diameter, spangles were smaller in the case of the coated HR steel at all cooling rates vs. the comparable BR steel as shown in Figure 4-21.

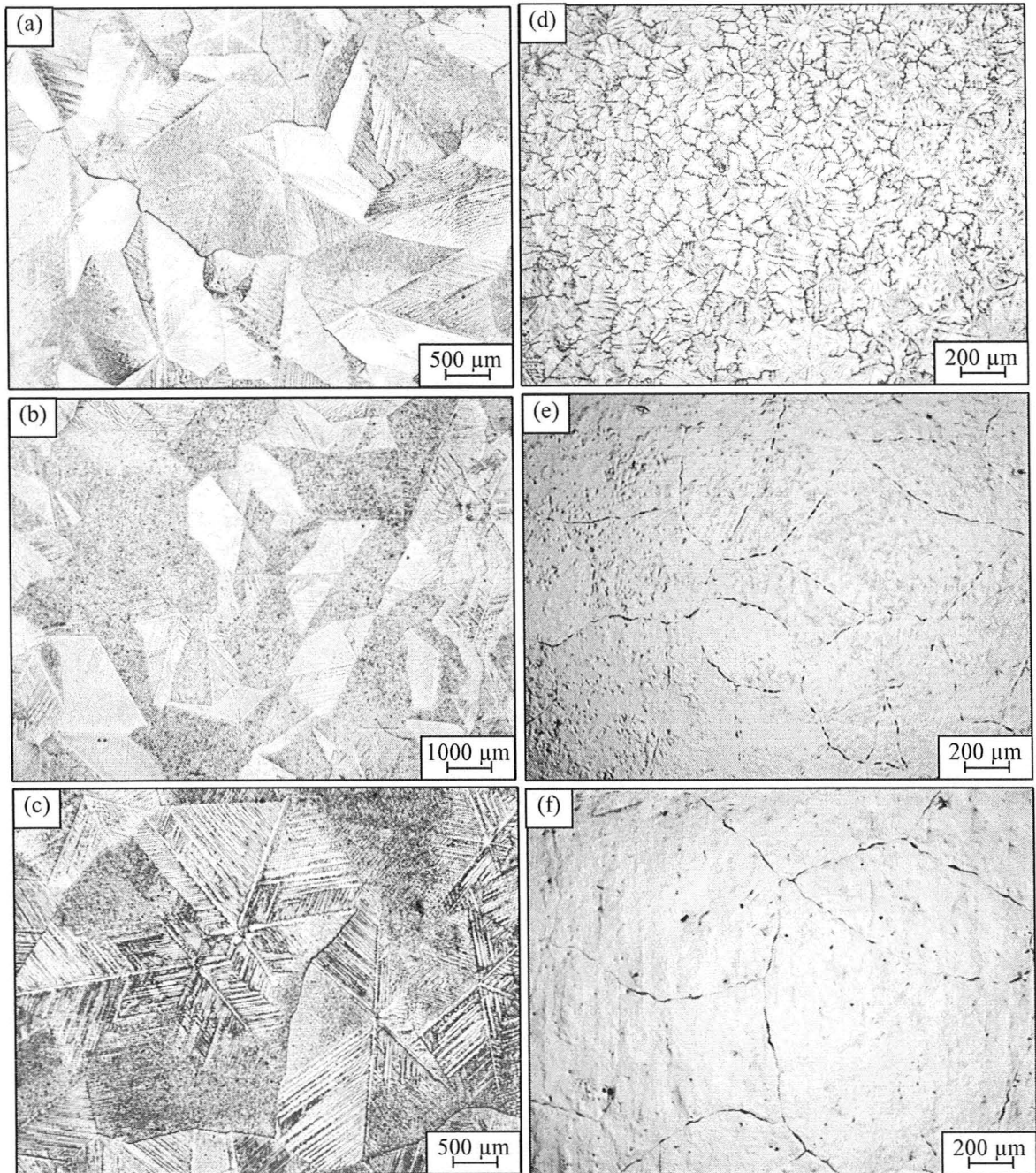


Figure 4-17. Low magnification optical micrographs of the as-cast coating surface containing 0.01 wt% Sb on BR steel cooled at (a) 10 °C/s (b) 1 °C/s (c) 0.1 °C/s and on HR steel cooled at (d) 10 °C/s (e) 1 °C/s (f) 0.1 °C/s

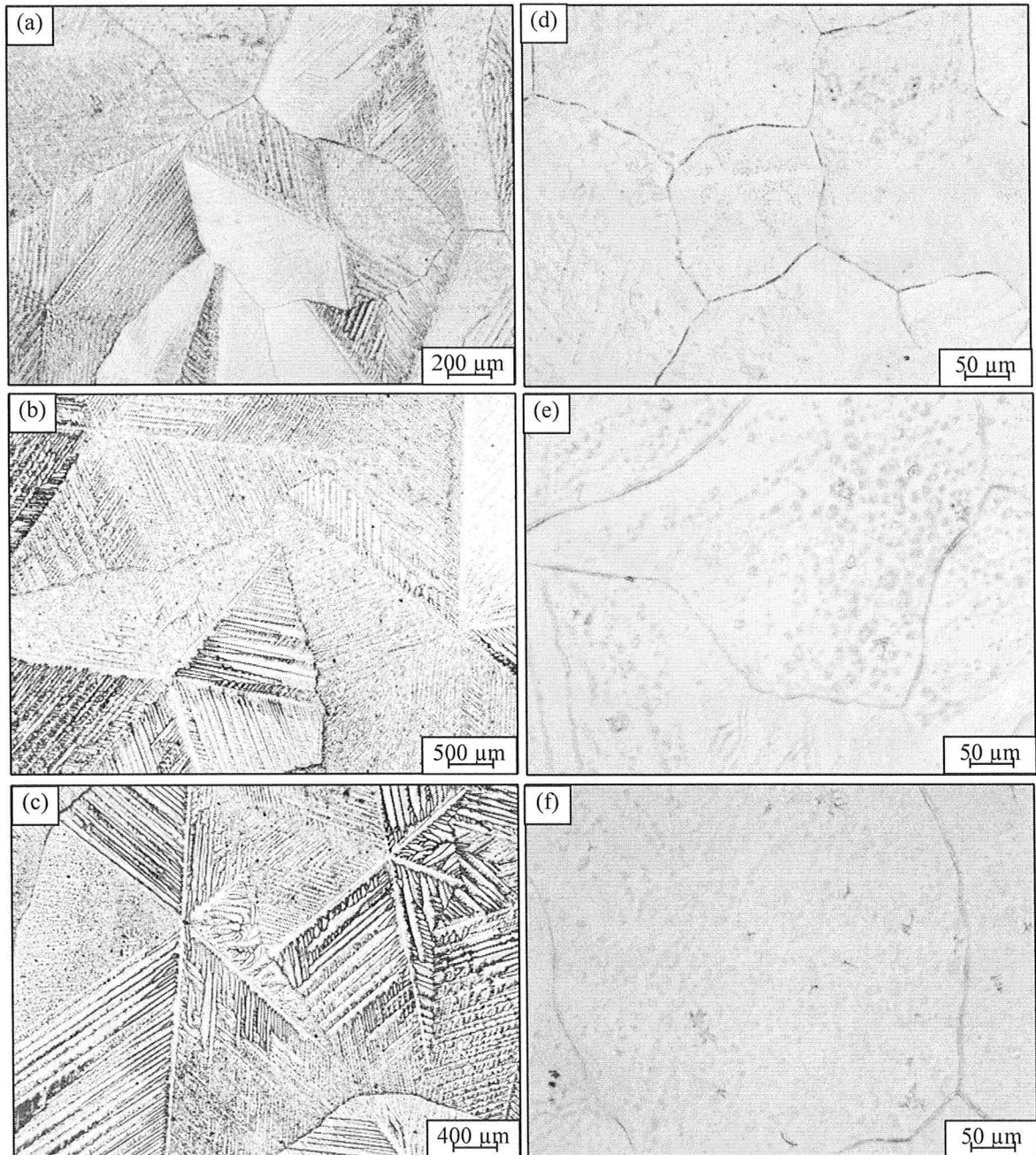


Figure 4-18. High magnification optical micrographs of the as-cast coating surface containing 0.01 wt% Sb on BR steel cooled at (a) 10 °C/s (b) 1 °C/s (c) 0.1 °C/s and on HR steel cooled at (d) 10 °C/s (e) 1 °C/s (f) 0.1 °C/s

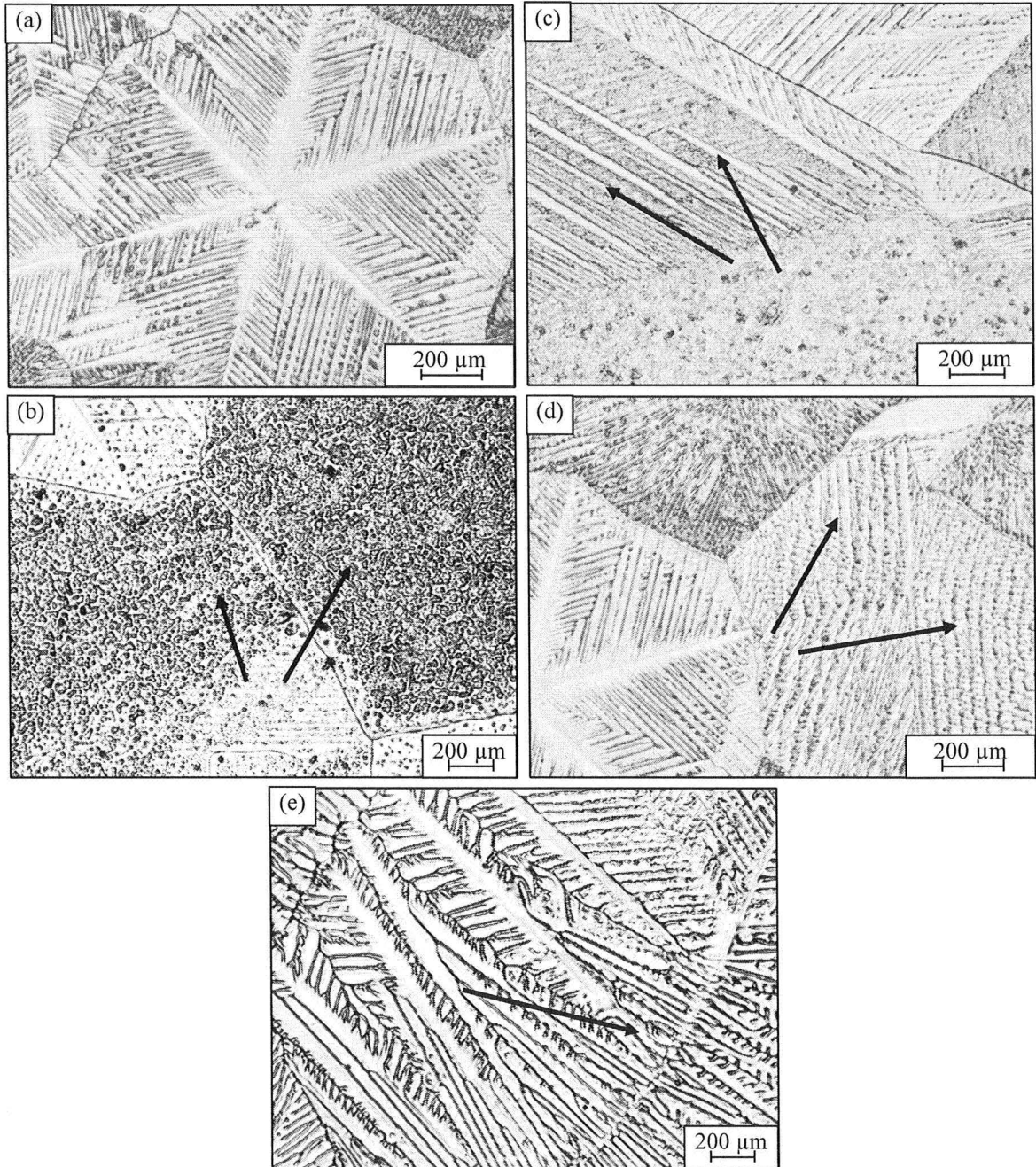


Figure 4-19. Optical micrographs of the (a) shiny (b) dimpled (c) feathery (d) ridged and (e) orthogonal-dendritic morphologies on coated BR steel cooled at $0.1\text{ }^{\circ}\text{C/s}$

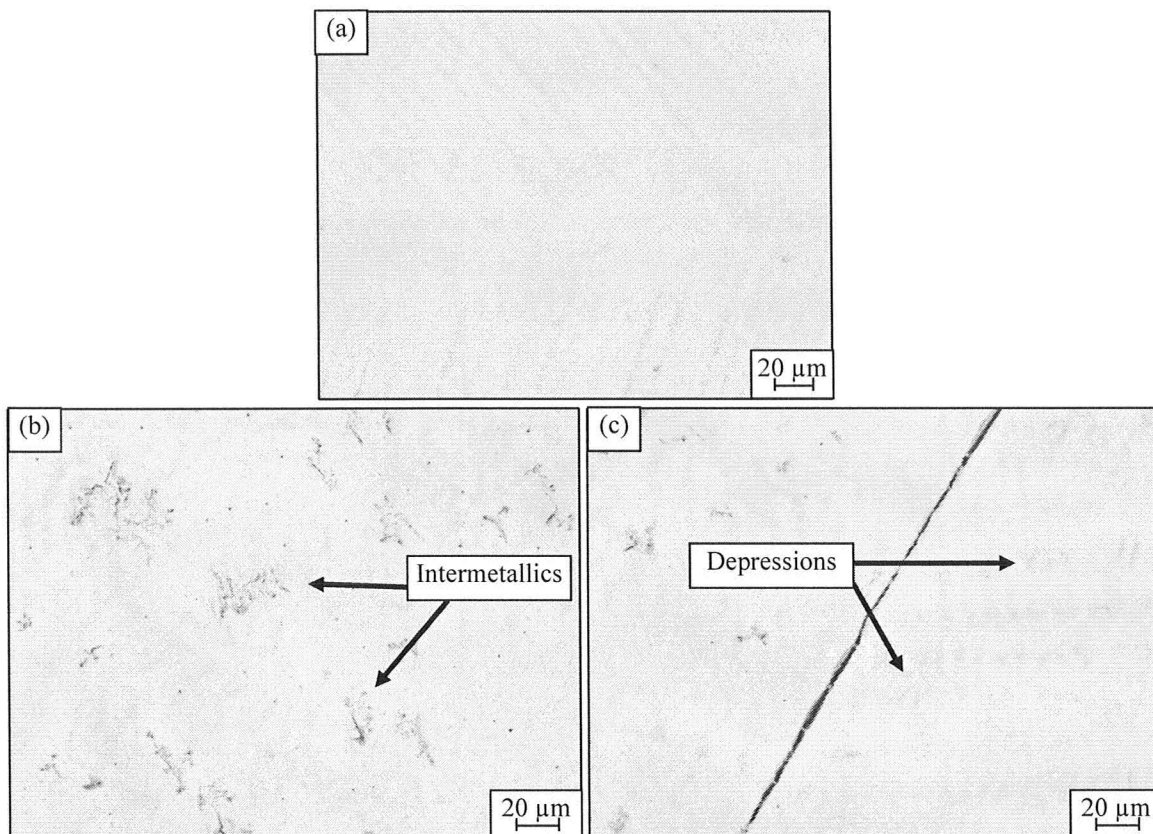


Figure 4-20. Optical micrographs of (a) bright and (b-c) dark regions on BR steel cooled at 0.1 °C/s

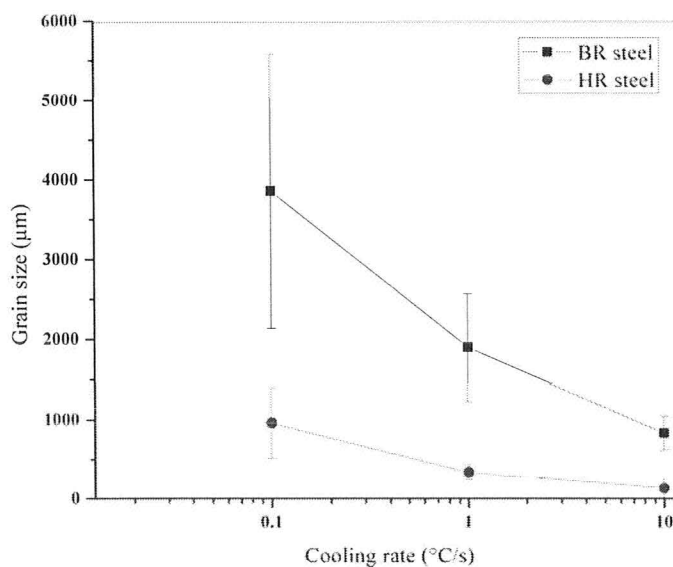


Figure 4-21. Grain size vs. cooling rate for the BR and HR steels

4.2.2. Coating Cross-section Microstructure

Optical microscopy was carried out on the coating cross-sections of both substrates for cooling rates of 10 °C/s and 0.1 °C/s.

➤ **BR steel**

The coating microstructure cooled at 10 °C/s on the BR substrate is shown in Figure 4-22. It can be seen that the coating consisted of two layers of zinc grains. Following previous reasoning for the presence of a two-layered structure for a coating containing no Sb, it is proposed that the zinc grains were nucleated simultaneously at both the steel/molten zinc and molten zinc/air interfaces. GDOES results showed higher concentration of Al at the steel/coating interface and on the coating surface, implying the presence of $\text{Fe}_2\text{Al}_5\text{Zn}_x$ and aluminum oxide film at the steel/coating interface and on the coating surface (Figure 4-23). Thus, nucleation could potentially take place at both the $\text{Fe}_2\text{Al}_5\text{Zn}_x$ and Al_2O_3 surfaces.

Figure 4-24 illustrates the coating cross-section on a BR steel cooled at 0.1 °C/s. Clearly, only one layer of zinc grains can be observed through the coating thickness since the cooling rate at the molten zinc/air interface was not sufficient for nucleation on this side. Thus, the steel surface was the only active interface for the nucleation of zinc grains.

Once the nuclei were formed, lateral growth of dendritic arms occurred in the plane of the steel substrate at both cooling rates. Also, grains were slowly thickened until the adjacent grains impinge together at the end of coating solidification.

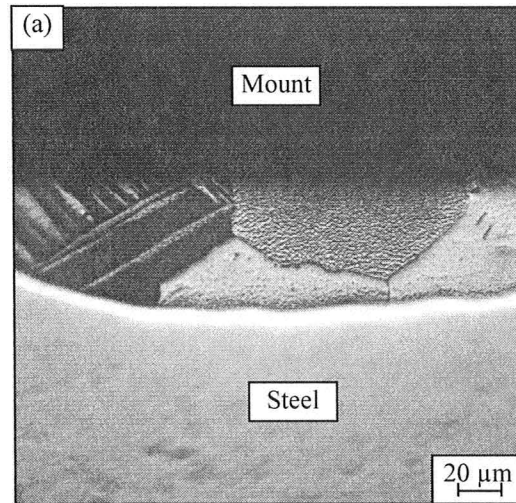


Figure 4-22. Optical micrograph of the coating cross-section on a BR substrate cooled at 10 °C/s

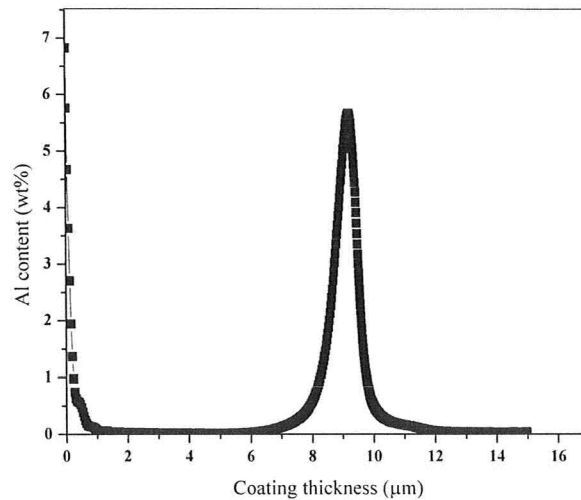


Figure 4-23. Al content as a function of coating thickness for coated HR steel substrate cooled at 10 °C/s

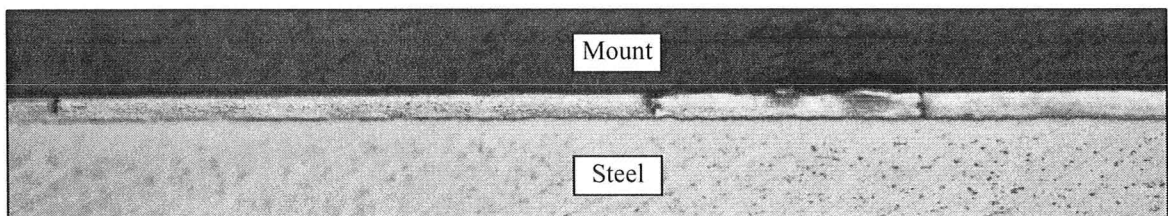


Figure 4-24. Optical micrograph of a coating cross-section cooled at 0.1 °C/s cooling rate on a BR substrate

➤ **HR steel**

An optical image of the coating cross-section cooled at 10 °C/s on the HR substrate displayed only one layer of zinc grains across the coating thickness (Figure 4-25). It is suggested that the rough $\text{Fe}_2\text{Al}_3\text{Zn}_x$ /molten zinc interface was more favourable for nucleation as compared to the molten zinc/air interface and therefore nucleation occurred solely at the steel surface. Also, Sb is known to decrease the surface tension of molten zinc and, therefore, decrease the relative surface energy of the steel surface which in turn results in the lower driving force for nucleation [Liu 2007]. Consequently, only one layer of zinc nuclei was likely formed during coating solidification. Once the surface of the steel was covered with this layer, slow thickening of grains occurred until they reached the coating/air interface. Similar results were obtained for the coated HR steel cooled at 0.1 °C/s.

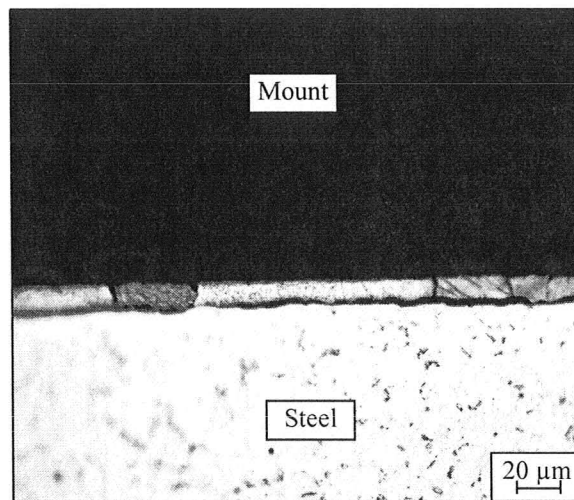


Figure 4-25. Optical micrograph of a coating cross-section on a HR steel substrate cooled at 10 °C/s

4.2.3. Coating Intermetallics

In order to investigate the intermetallic phases in coatings containing 0.01 wt% Sb, the coating microstructure of the BR and HR substrates at all cooling rates was studied using SEM-SAM and TEM. On both substrates and at all cooling rates, five different contrasts were observed in SEM-BEIs and, therefore, it was concluded that five phases were present in the coatings. Similar results were found for both substrates and all cooling conditions and, therefore, only the results for the BR substrate cooled at 0.1 °C/s will be discussed.

Figure 4-26(a) shows the SEM-BEI of the dendritic region on a coated BR steel cooled at 10 °C/s. Small white particles were found in the interdendritic regions and are highlighted by black arrows in the Figure 4-26(a-d). It can be seen that the zinc matrix was largely depleted of intermetallic particles.

The grain boundaries were decorated by a mixture of white and grey phases as shown in Figure 4-26(b). Furthermore, the coating surface in the non-dendritic regions contained a variety of intermetallic phases. Particles with white contrast, round particles with light grey contrast, star-like particles with dark grey contrast and Chinese-script particles with black contrast were randomly distributed on the coating surface (Figures 4-26(c) and (d)).

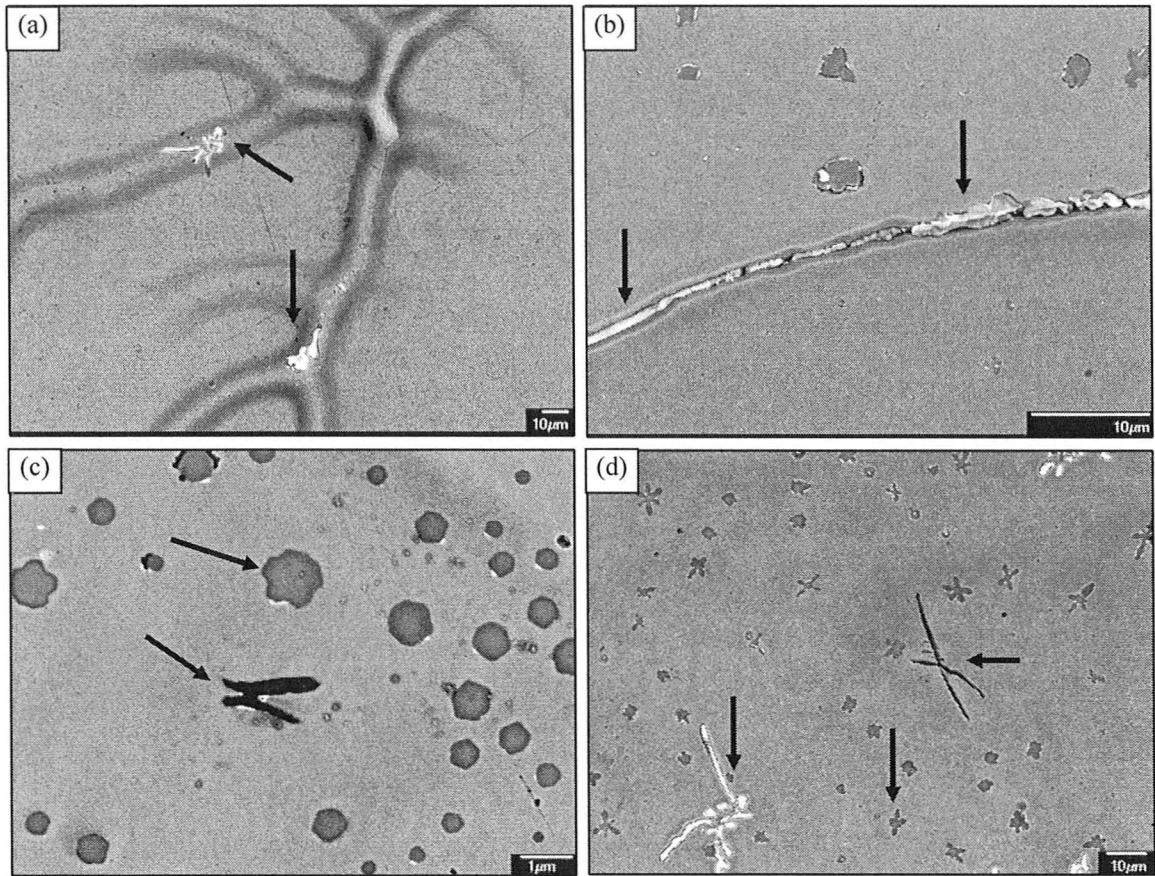


Figure 4-26. SEM-BEIs of the intermetallics on (a) dendritic (b) grain boundary and (c-d) non-dendritic regions on coated BR steel cooled at 0.1 °C/s

Figures 4-27(a-d) show higher magnification SEM-BEIs of the above mentioned intermetallic particles. It should be mentioned that the white and light grey particles were also found within the coating thickness while the dark grey and black precipitates were only detected on the coating surface.

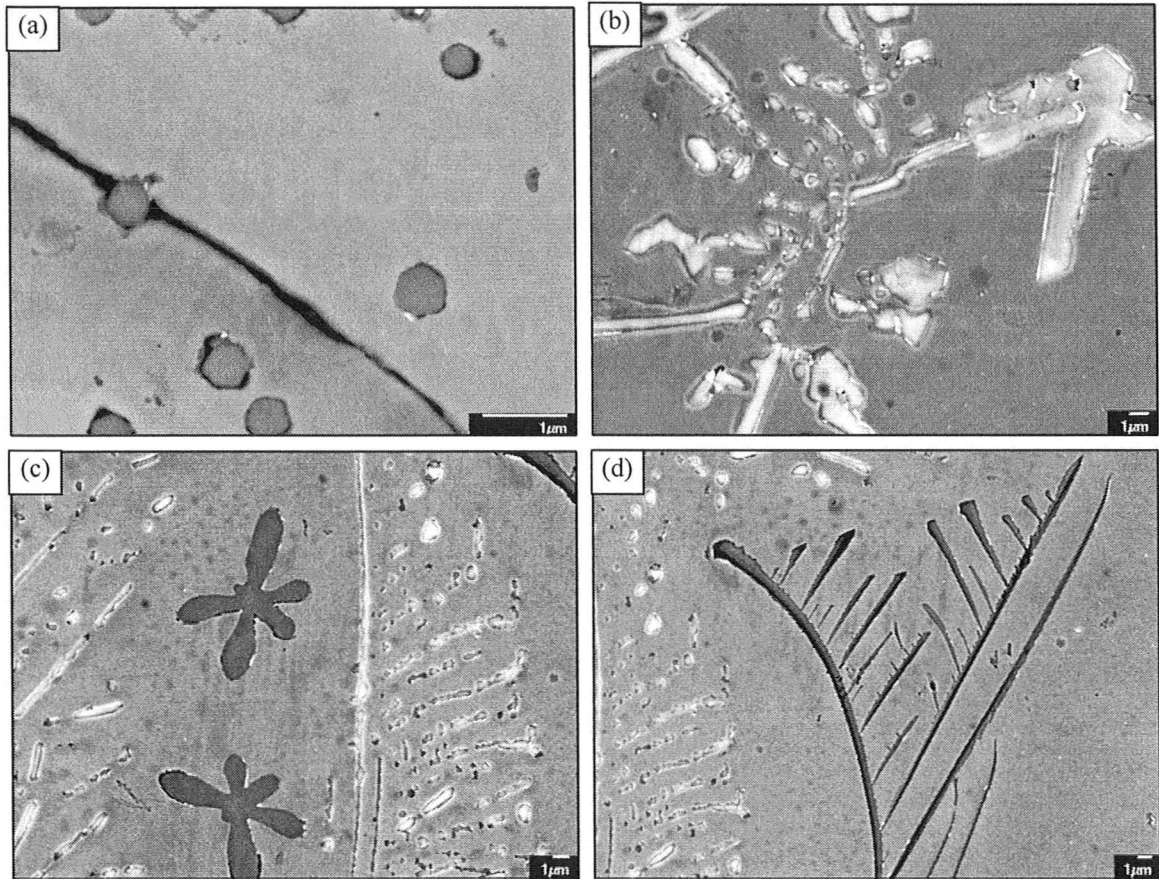


Figure 4-27. SEM-BEIs of (a) light grey (b) white (c) dark grey and (d) black particles on the BR steel cooled at 0.1 °C/s

For further study on the chemical composition of the intermetallic phases present, four regions on the slow cooled coated BR steel surface were examined using SAM elemental mapping and point analysis on several areas after surface sputtering with Ar ions for 20-30 s to remove oxide films and other contaminants.

The first area chosen contained small round precipitates for which the Zn, Fe and Al elemental maps were similar to those shown previously in Figures 4-11(a-d). Also, the

corresponding quantitative chemical analysis results were similar to the data presented in Table 4-1 and are not repeated here.

The SEM-SEI of an area containing an irregular intermetallic particle is shown in Figure 4-28(a). The corresponding Zn, Al and Sb SAM thermal pseudo colour maps are shown in Figures 4-28(b-d). It can be seen that the intermetallic phase contained mainly Sb and Al. Auger colour overlay images confirmed the presence of Al along with the zinc matrix as shown in Figure 4-28(e). Also, Figure 4-28(f) shows the presence of a mixed Al+Sb phase in the particle. According to the SAM point analysis results, the main constituents of the irregular particle were Sb and Al along with a small amount of Zn (Table 4-3).

Figure 4-29(a) illustrates an area on the coating surface containing a star-like particle. The acquired elemental maps showed the presence of Zn, Fe, Cr, Al and Pb within this phase while high concentrations of Sn were detected in areas outside the particle perimeter (Figures 4-29(a-g)). Also, the presence of high concentrations of Zn and Al as well as small quantities of impurities such as Sn and Cr were confirmed using the SAM point analysis. It should be noted that no elemental Sb was detected in this precipitate.

The final area chosen contained a Chinese-script intermetallic particle on which SEM-SEI and SAM mapping were performed and the results shown in Figures 4-30(a-e). Accordingly, Zn, Fe, Al and small amount of Cr were identified in the intermetallic

phase. Based on the quantitative data shown in Table 4-3, high concentrations of Al and Fe, small concentrations of Zn and Cr and 0 at% Sb were detected in this phase.

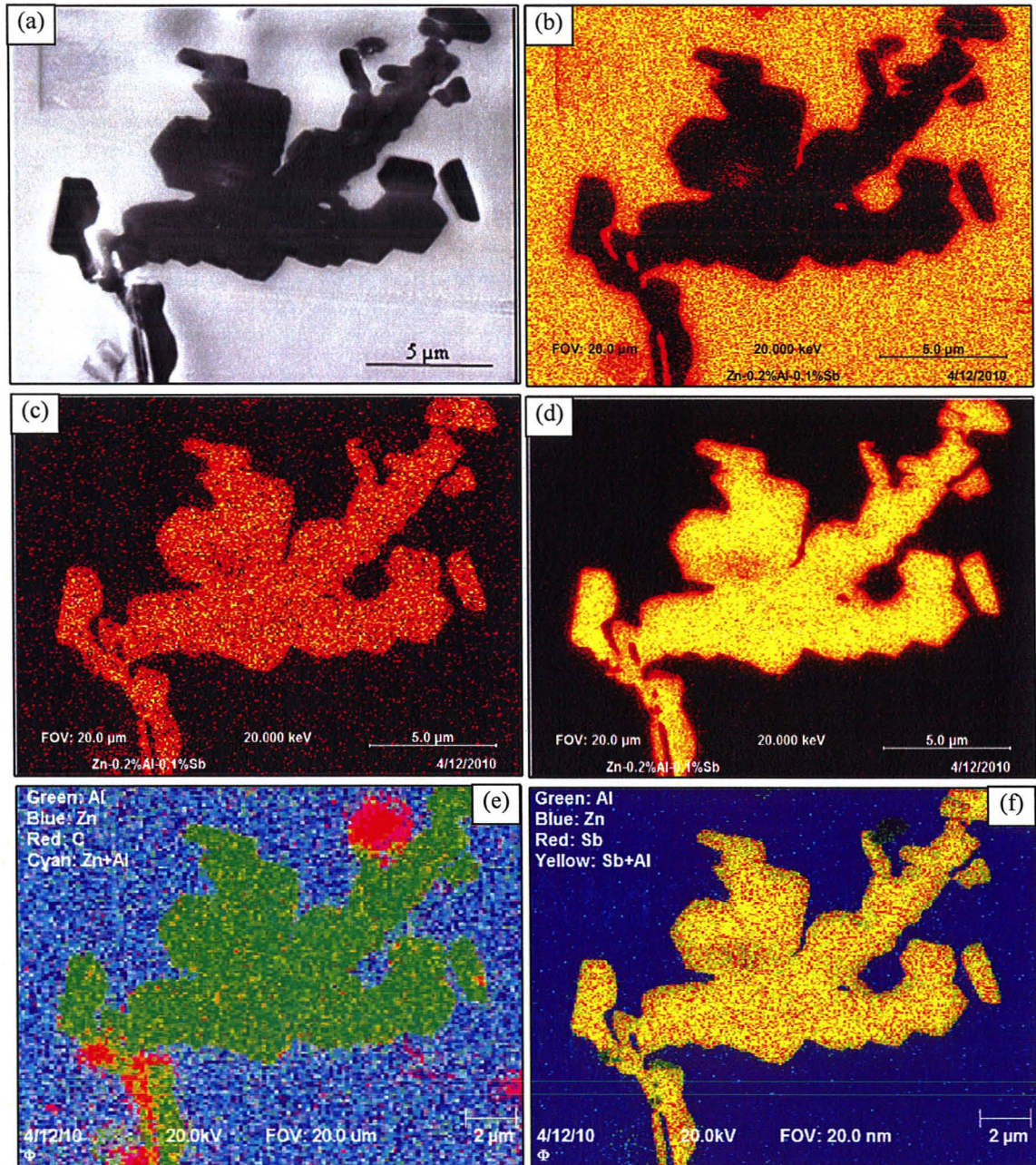


Figure 4-28. (a) SEM-SEI of a coated BR steel cooled at 0.1 °C/s containing an irregular particle and (b) Zn (c) Al and (d) Sb SAM maps (e-f) auger colour overlay images

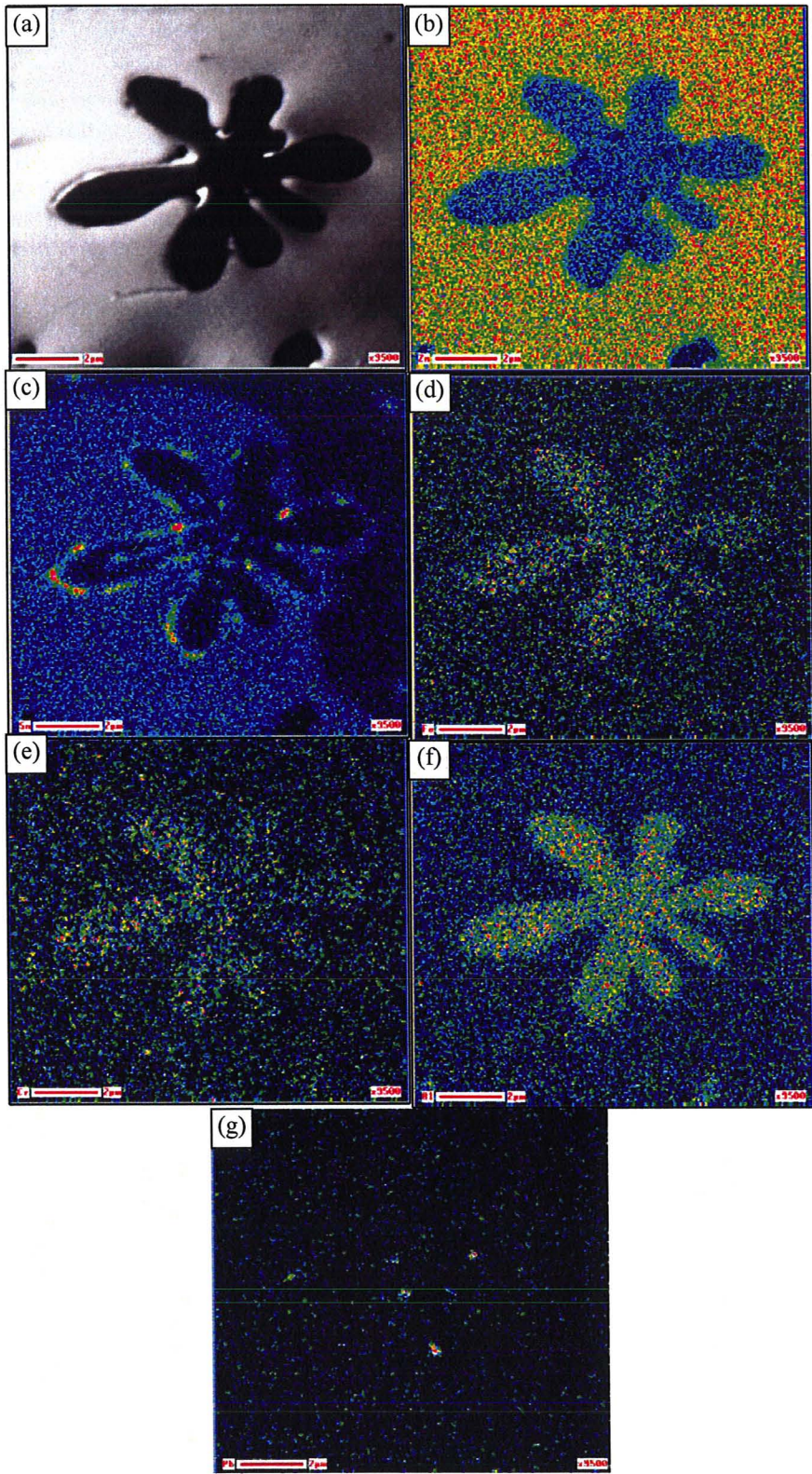


Figure 4-29. (a) SEM-SEI of the coated BR steel cooled at 0.1 °C/s containing a star-like particle and (b) Zn (c) Sn (d) Fe (e) Cr (f) Al and (g) Pb SAM maps

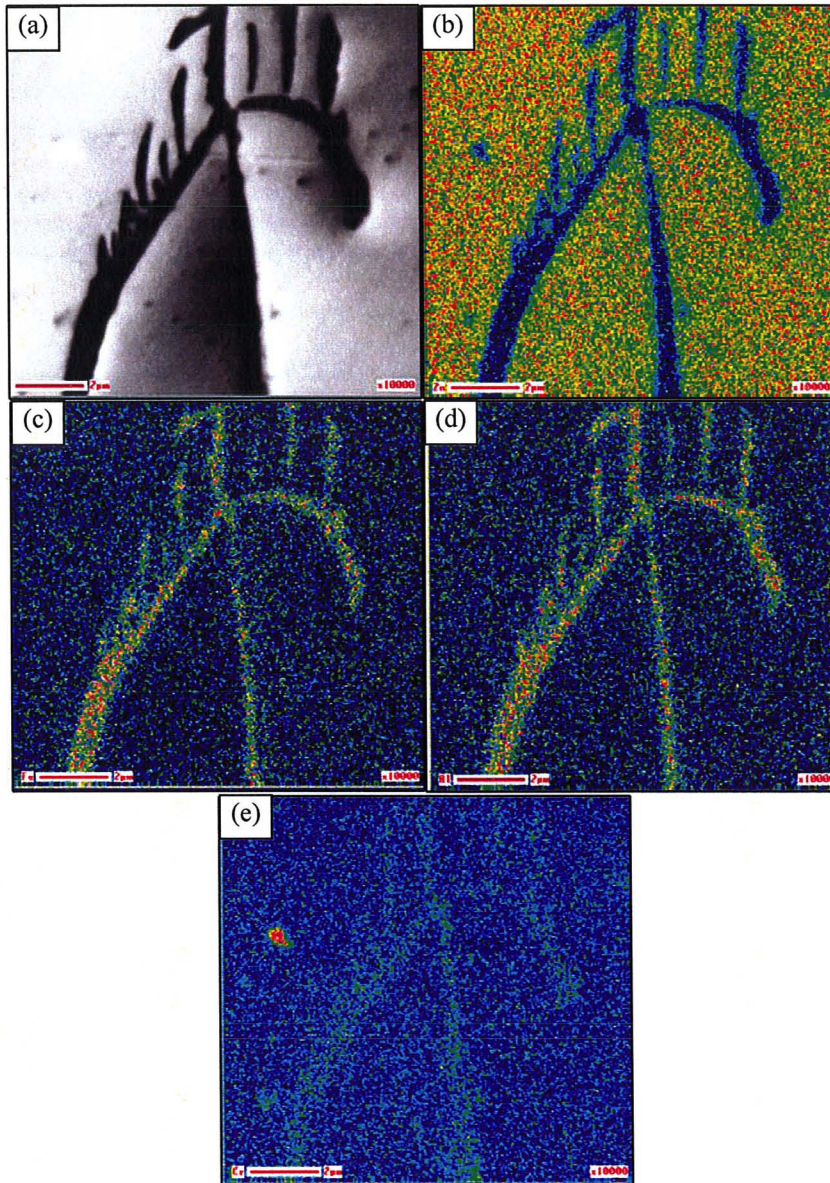


Figure 4-30. (a) SEM-SEI of a coated BR steel cooled at 0.1 °C/s containing a Chinese-script particle and (b) Zn (c) Fe (d) Al and (e) Cr SAM maps

Table 4-3. SAM point analysis of the different phases on coated BR steel cooled at 0.1 °C/s (at%)

Phase \ Element	Zn	Al	Sb	Fe	Cr	Sn
Irregular	17.1	30.4	52.5	-	-	-
Star-like	31.3	46.4	-	12.6	2.8	6.9
Chinese-script	7.7	65.2	-	23.7	3.3	-

In conclusion, it was deduced that the Sb addition to the molten zinc bath resulted in the precipitation of irregular Al+Sb intermetallic particles. It was also found that the formation of star-like and Chinese-script particles was associated with the presence of segregated impurities such as Cr, Sn and Pb on the coating surface. In addition, the Chinese-script particle contained more Al and Fe as compared to the star-like particle.

To further investigate the composition of the white intermetallic phase, TEM was carried out on a coated BR steel cooled at 0.1 °C/s fabricated via FIB milling.

A TEM-dark field image of the white intermetallic particle and the corresponding diffraction pattern are shown in Figures 4-31(a) and (b), respectively. The {001} diffraction pattern for a variety of Zn, Al and Sb intermetallics was simulated and is shown in Figure 4-32(a). Figure 4-32(b) shows the matching AlSb intermetallic diffraction pattern.

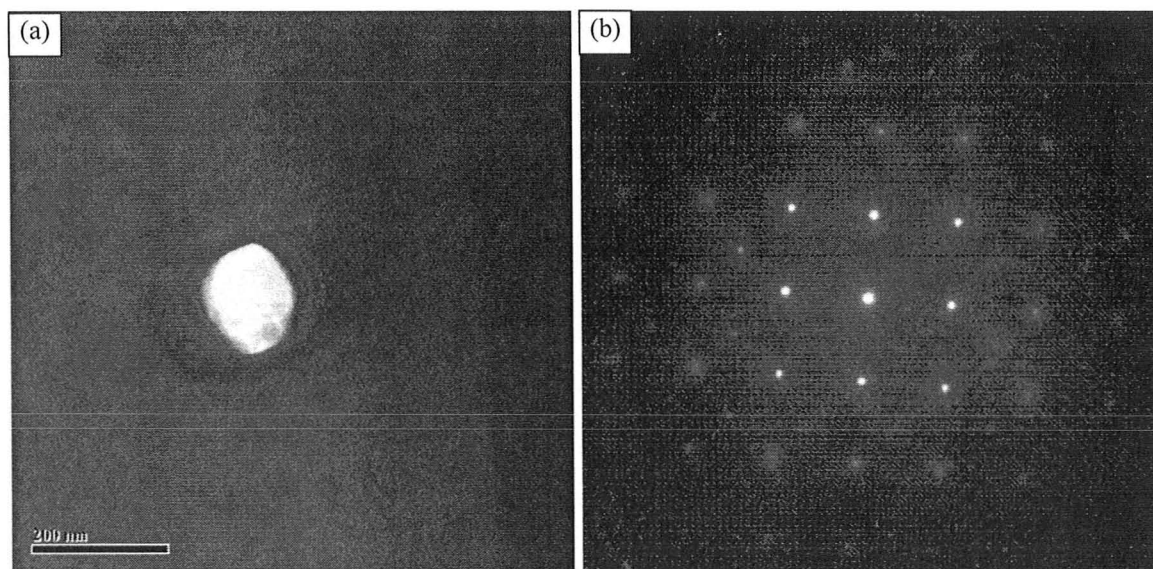


Figure 4-31. (a) TEM-dark field image of the white intermetallic particle and the corresponding (b) diffraction pattern

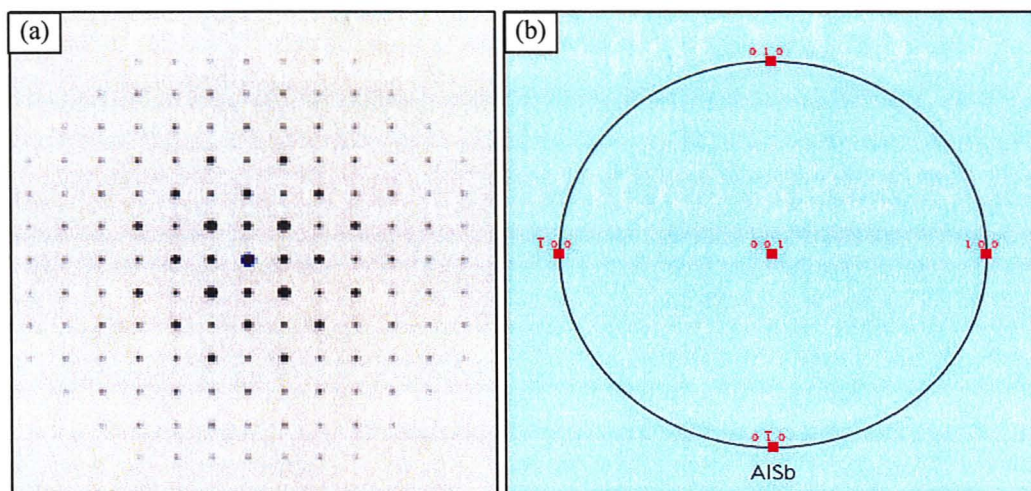


Figure 4-32. (a) Simulated $\{001\}$ diffraction pattern (b) solution for the obtained diffraction pattern

4.2.4. Coating crystallographic texture

As mentioned previously, it has been reported that the addition of small concentrations of Sb to the liquid zinc bath promotes the basal crystallographic texture in zinc coatings [Strutzenberger 1998]. In order to explore the coating crystallographic texture, EBSD orientation mapping was carried out on BR and HR coated steels cooled at $10\text{ }^{\circ}\text{C/s}$ and $0.1\text{ }^{\circ}\text{C/s}$.

Figures 4-33(a-d) and 4-34(a-d) display the microstructure, Euler orientation colour maps, pole figures and $\{0002\}$ pole plot for coatings on BR steel substrate cooled at $10\text{ }^{\circ}\text{C/s}$ and $0.1\text{ }^{\circ}\text{C/s}$, respectively. As can be seen for both cooling rates, there was a very strong preferred orientation along the $\langle 0001 \rangle$ direction and random distribution for the other orientations. In addition, the $\{0002\}$ pole plot exhibited a $10\text{-}15^{\circ}$ inclination angle for the $\{0002\}$ basal planes with respect to the steel substrate surface. This was very similar to the previous findings for BR substrates with 0 wt% Sb.

The crystallographic texture of the coatings on HR steels cooled at 10 °C/s and 0.1 °C/s were investigated and the results shown in Figures 4-35(a-d) and 4-36(a-d). According to the {0002} pole figures for both cooling conditions, the coating exhibited a strong preferred basal orientation with an average inclination angle of 20-30° with respect to the steel surface plane. In conclusion, Sb addition to the molten zinc bath had a similar influence on the overall texture for the HR steel for both cooling rates, although the <0001> fiber texture was not as pronounced as this texture on coated BR steel. As a result, some dendritic spangles with basal texture may be observed on the coated HR surface (Figures 4-17(d)).

To explore the crystallography of a zinc grain containing dendritic and non-dendritic regions, EBSD analysis was performed on the coated BR steel cooled at 0.1 °C/s. Figure 4-37(a) illustrates the SEM-SEI of a zinc spangle containing dendritic and non-dendritic regions on a coated BR steel cooled at 0.1 °C/s. The Euler orientation colour map displayed a uniform blue for the entire spangle which implies that the dendritic and non-dendritic regions have the same orientation (Figure 4-37(b)). The corresponding pole figures show the orientation of the examined spangles with respect to the RD and TD as shown in Figures 4-37(c). In addition, the orientation of a number of spangles were analysed similarly and the Euler orientation colour maps exhibited uni-colour distributions. Table 4-4 shows the area percentage of basal zinc grains inclined for 0-15° relative to the steel sheet for the BR and HR steels at 10 °C/s and 0.1 °C/s cooling rates.

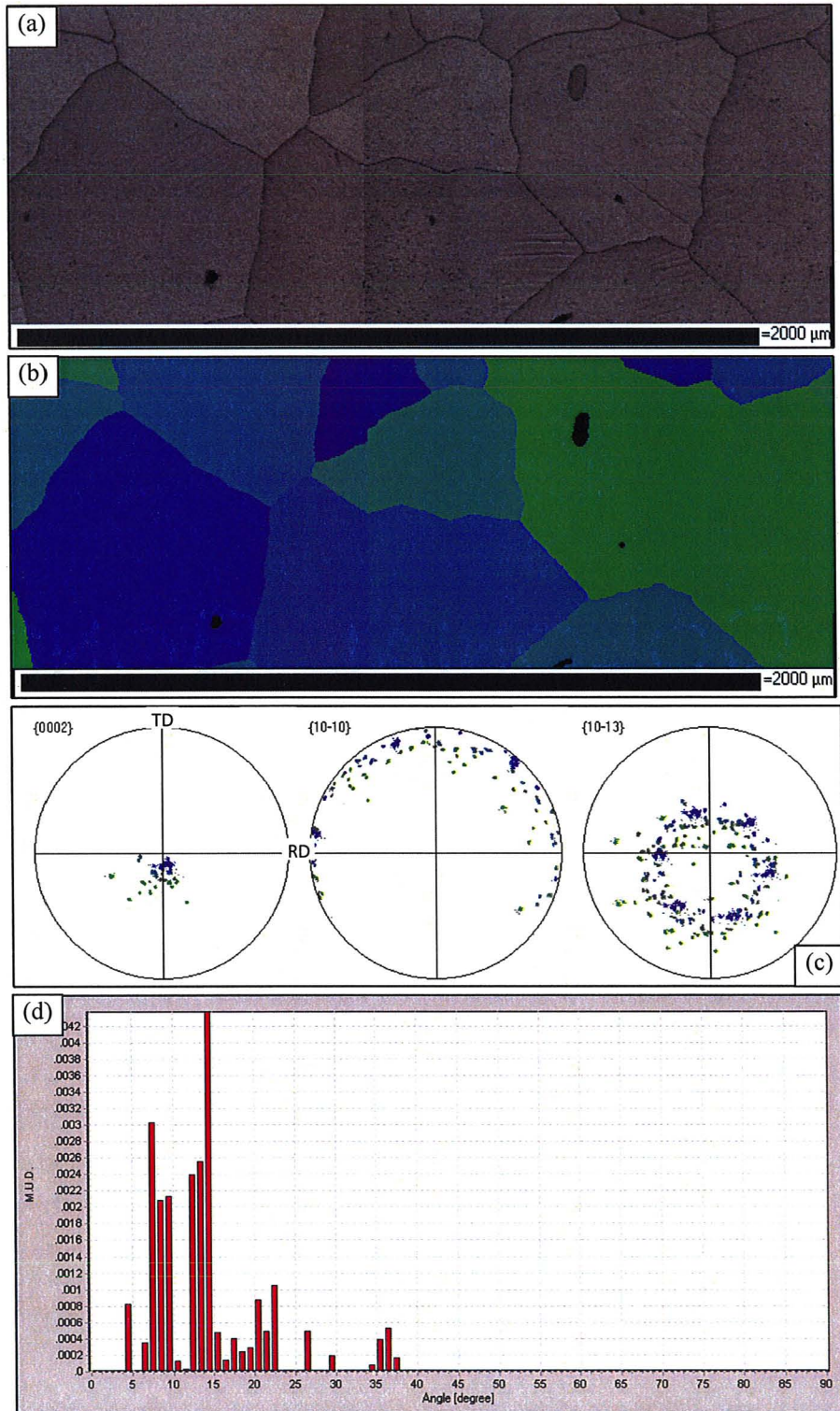


Figure 4-33. (a) Microstructural map (b) Euler orientation colour map (c) pole figures and (d) {0002} pole plot of coating surface on BR steel cooled at 10 °C/s

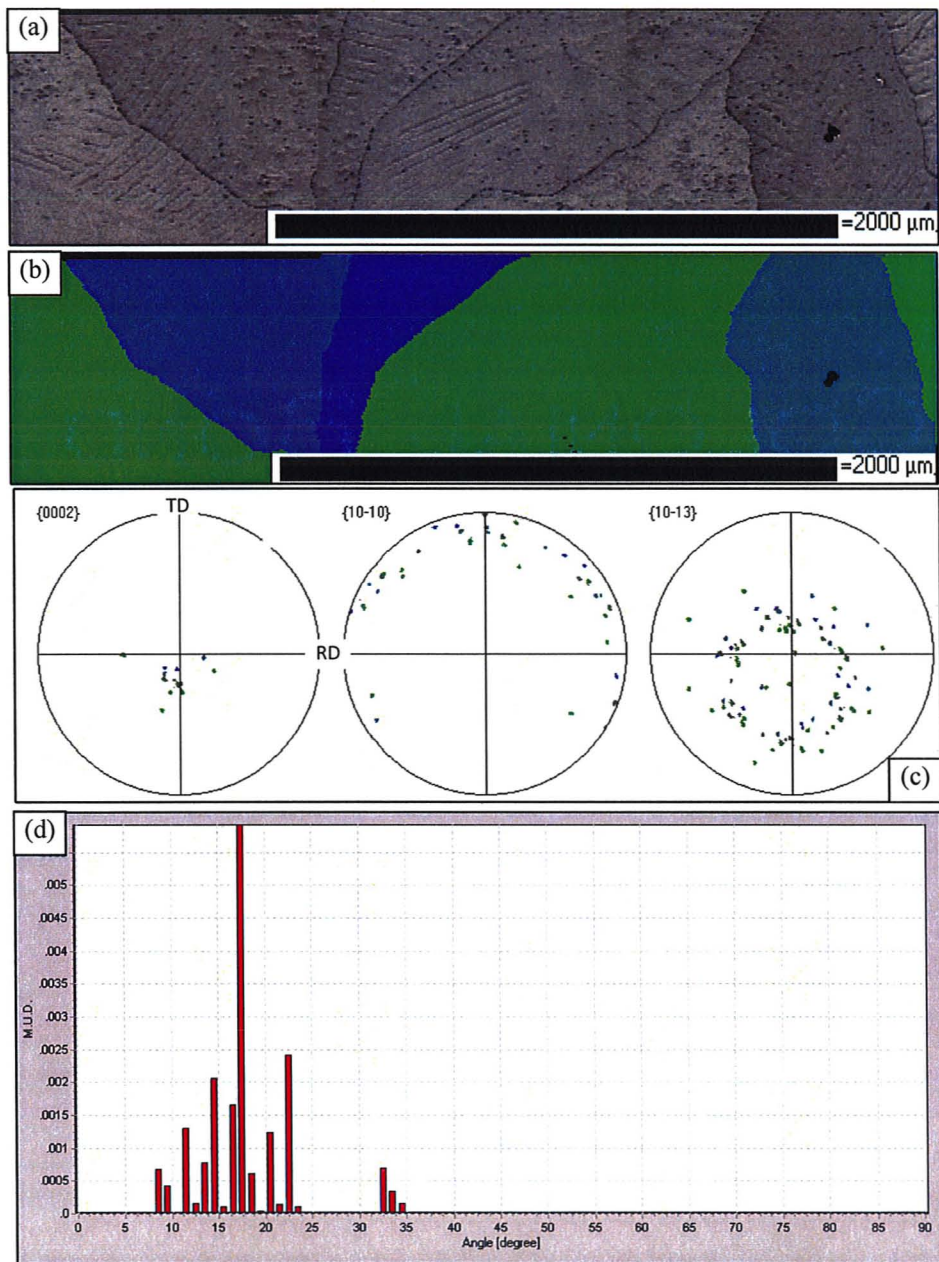


Figure 4-34. (a) Microstructural map (b) Euler orientation colour map (c) pole figures and (d) {0002} pole plot of coating surface on BR steel cooled at 0.1 °C/s

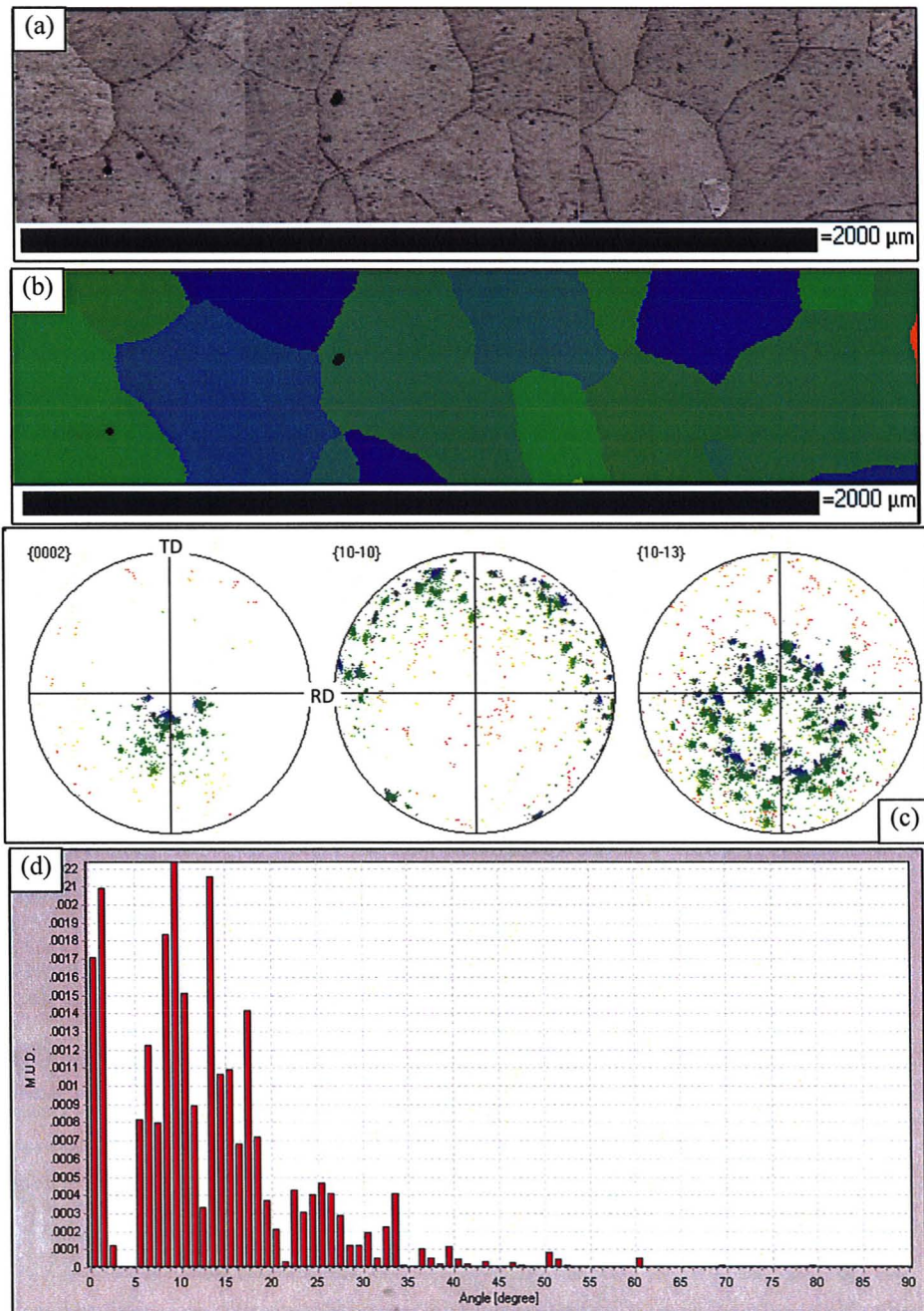


Figure 4-35. (a) Microstructural map (b) Euler orientation colour map (c) pole figures and (d) {0002} pole plot of coating surface on HR steel cooled at 10 °C/s

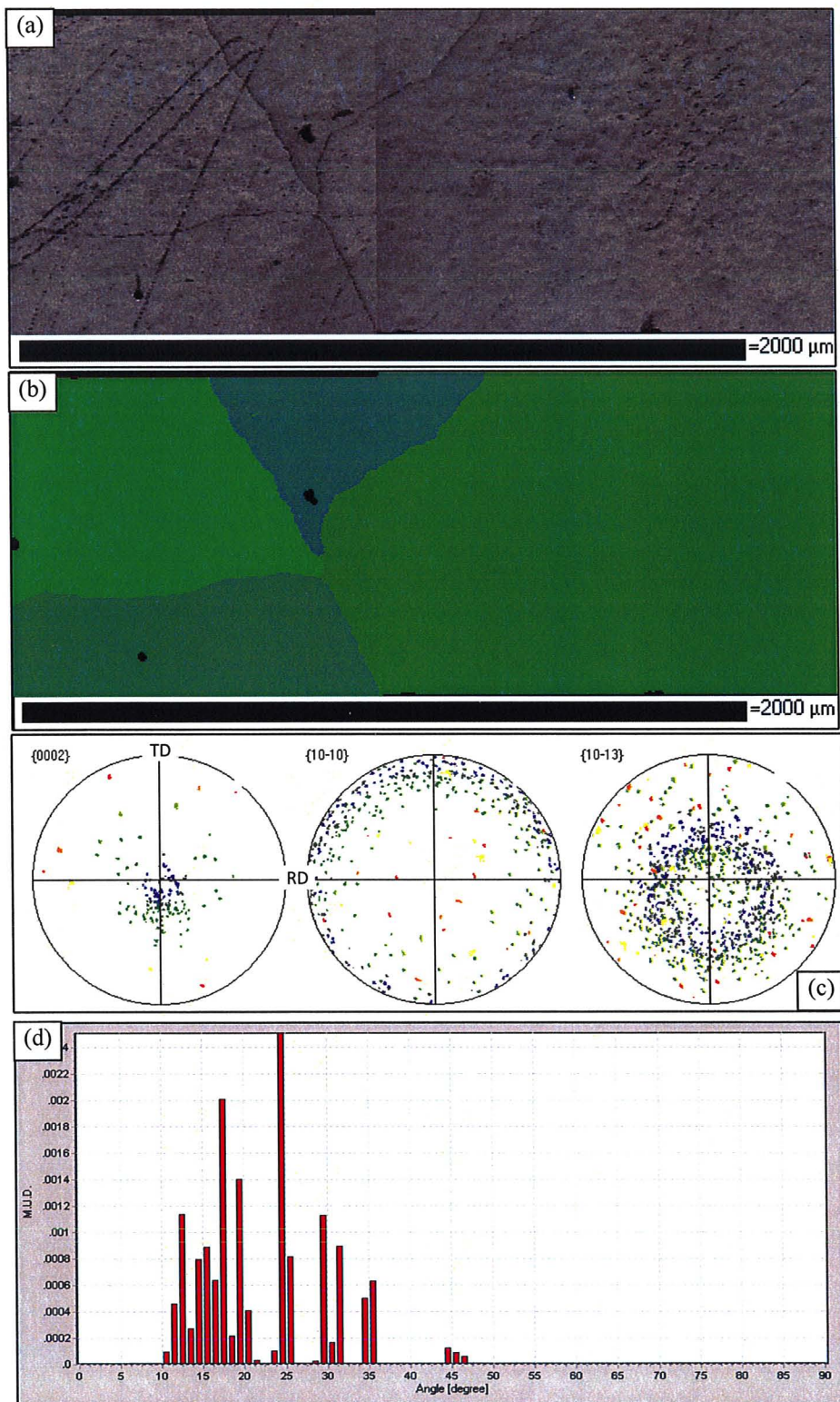


Figure 4-36. (a) Microstructural map (b) Euler orientation colour map (c) pole figures and (d) {0002} pole plot of coating surface on HR steel cooled at 0.1 °C/s

Thus, it was concluded that zinc spangles are essentially single crystals of zinc and there is no orientation difference between the bright and dark areas within one spangle. It should be mentioned that the EBSD results for the coated BR and HR steels cooled at 1 °C/s were similar to the samples cooled at 0.1 °C/s.

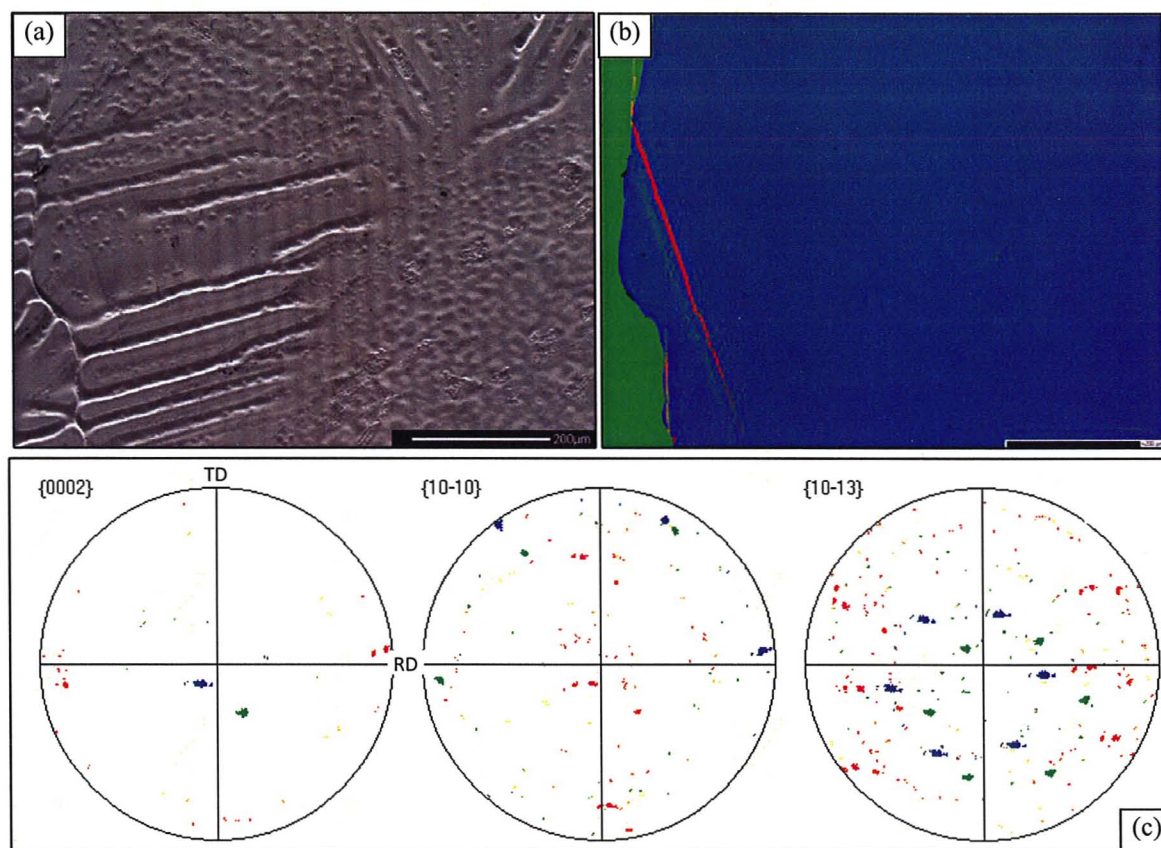


Figure 4-37. (a) SEM-SEI (b) Euler orientation colour map and (c) pole figures of zinc grains on coated BR steel substrate cooled at 0.1 °C/s

Table 4-4. Area percentage of basal zinc grains inclined for 0-15° relative to the steel sheet (%)

Steel substrate	Cooling rate (°C/s)	
	10	0.1
BR	45.1	28.9
HR	20.2	10.4

4.3. 0.03 wt% Sb Alloy

4.3.1. Coating Surface Microstructure

Following the experimental matrix shown in Table 3-1, the Sb content of the molten zinc bath was raised to 0.03 wt% and dipping experiments carried out per the experimental matrix shown in Table 3-1. The as-cast coating microstructure on the BR and HR steel substrates for the 10 °C/s, 1 °C/s and 0.1 °C/s cooling rates are shown in Figures 4-38(a-f).

The optical images of the coating microstructure on the BR substrate exhibited hexagonal or diamond-shaped zinc spangles for all cooling conditions as shown in Figures 4-38(a-c) and 4-39(a-c). As can be seen, spangles were equally divided into alternate bright and dark regions, respectively. Bright areas had internal dendritic structures while dark areas were non-dendritic (Figure 4-38(b)). Regarding the spangle morphology, only shiny and dimpled structures were detected on the coating surface. Figure 4-40(a) displays a flowery zinc spangle with 6-fold symmetry and primary dendrite arms in the six $\langle 10\bar{1}0 \rangle$ crystallographic fast growth directions. The entire surface of similar spangles had a shiny morphology. On the other hand, some spangles were half dendritic and half non-dendritic and comprised both the shiny and dimpled morphology, as shown in Figure 4-40(b). In dimpled areas, the coating surface contained significant population of intermetallic precipitates as well as projections and depressions due to solidification shrinkage [Strutzenberger 1998] [Biber 1988].

The coating microstructure of the HR substrate cooled at 10 °C/s, 1 °C/s and 0.1 °C/s are illustrated in Figures 4-38(d-f) at higher magnification. For all cooling rates, the coating grains had an irregular shape and uneven surface, due to the underlying steel surface roughness. Similar to the coatings containing 0.01 wt% Sb, grains were partly dendritic for the 10 °C/s cooling rate (Figure 4-39(a)) while grains were entirely non-dendritic for the 1 °C/s and 0.1 °C/s cooling rates (Figures 4-39(b) and (c)). Furthermore, the surface of the 10 °C/s cooled coating was semi-reflective in dendritic regions (Figure 4-40(c)) while the surface of the 10 °C/s and 0.1 °C/s cooled coatings was dark where intermetallic compounds and microshrinkage depressions were present on the surface (Figure 4-40(d)). In addition, the coatings largely exhibited a dull morphology for all cooling conditions.

In comparison, flowery zinc spangles were formed on BR steel substrates while irregular zinc grains were formed on HR steel substrate for the 0.03 wt% Sb addition. The coating surface was smoother in the case of coatings on the BR substrate as compared to coatings on the HR substrate. Regarding the zinc morphology, coated BR samples had both shiny and dimpled structures while coated HR samples had a dominant dull morphology. Figure 4-41 shows the zinc grain size as a function of coating cooling rate for BR and HR substrates. The finest grains were found on the HR steel substrate cooled at 10 °C/s.

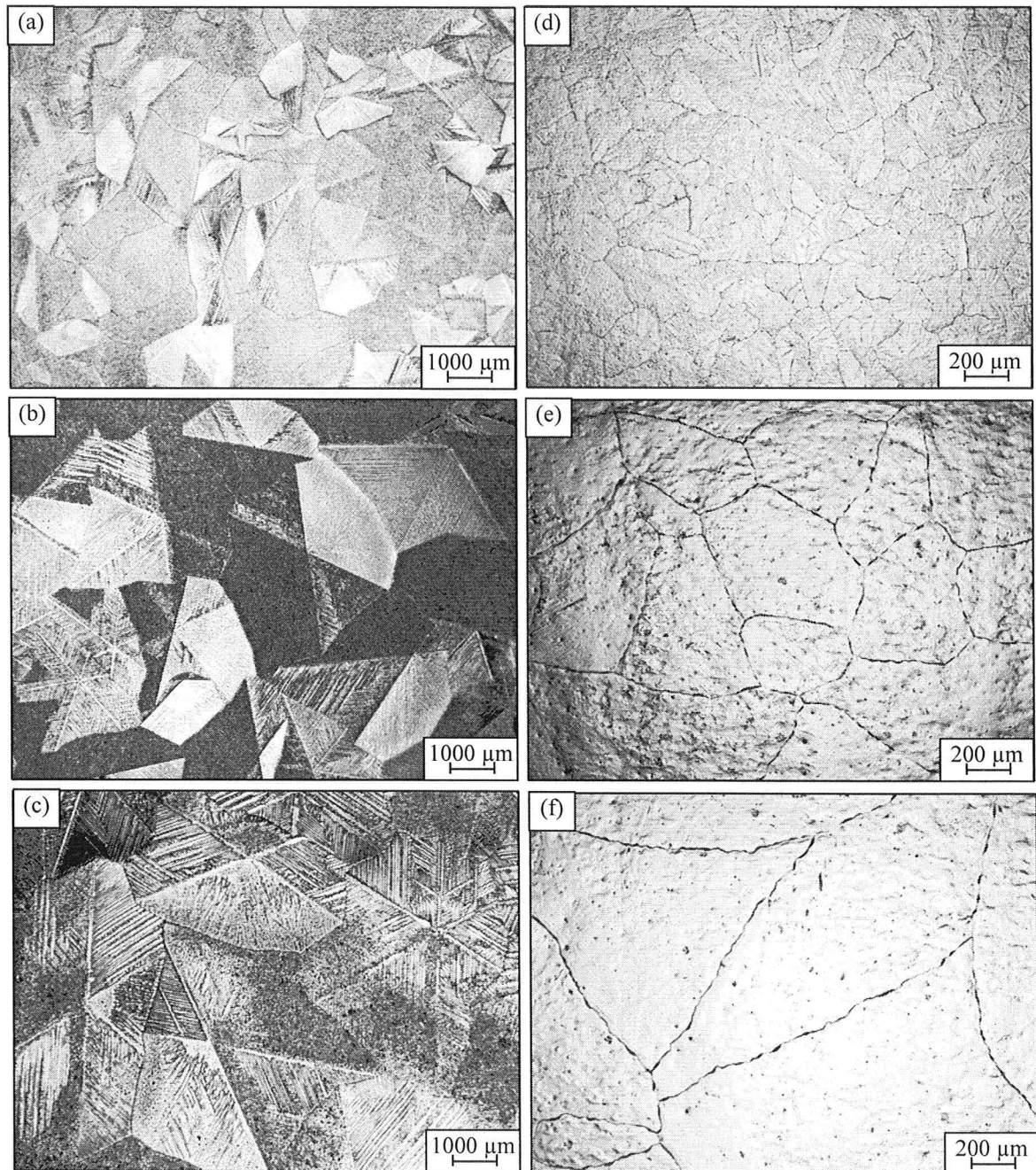


Figure 4-38. Low magnification optical micrographs of the as-cast coating surface containing 0.03 wt% Sb on BR steel cooled at (a) 10 °C/s (b) 1 °C/s (c) 0.1 °C/s and on HR steel cooled at (d) 10 °C/s (e) 1 °C/s (f) 0.1 °C/s

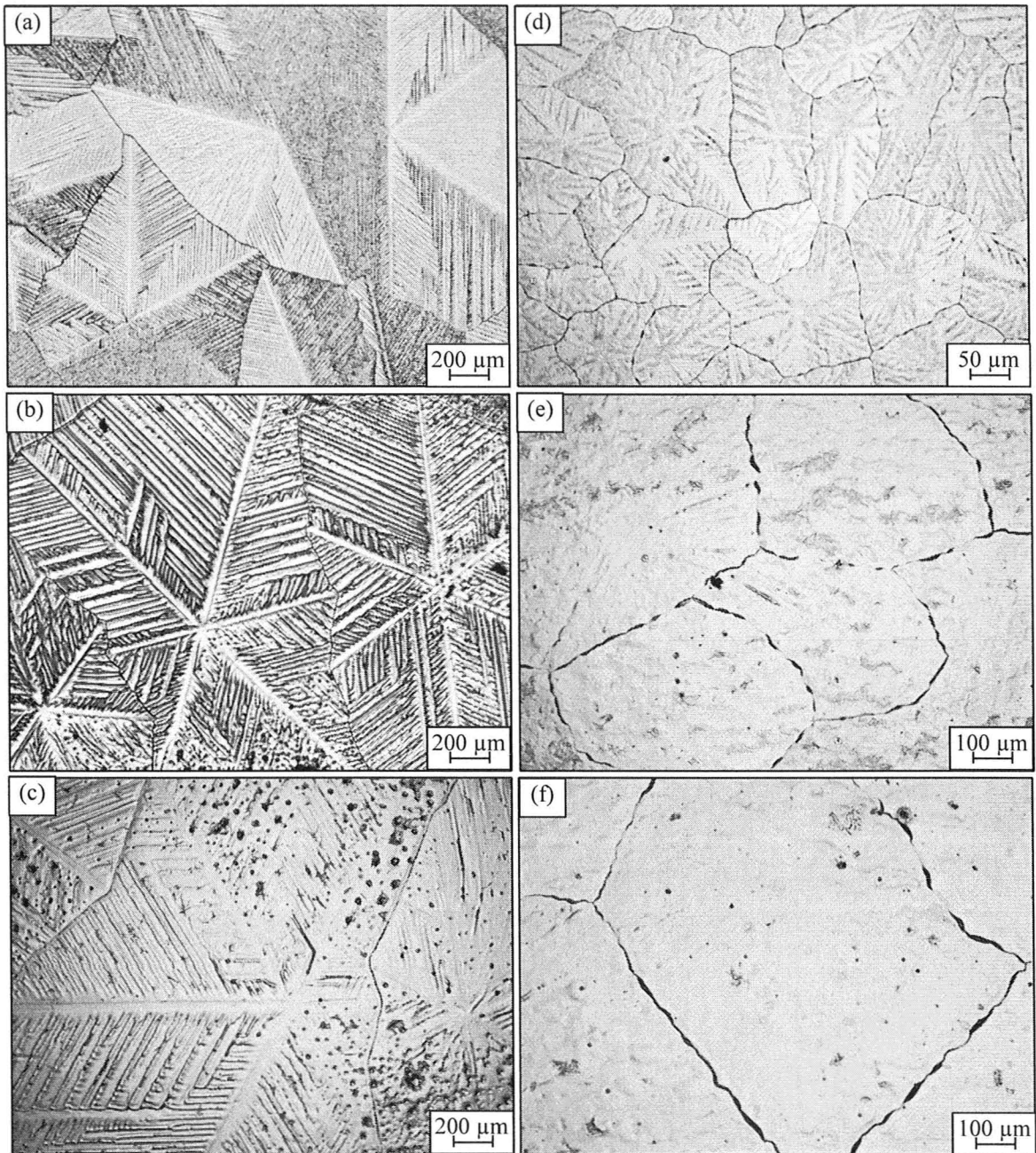


Figure 4-39. High magnification optical micrographs of the as-cast coating surface containing 0.03 wt% Sb on BR steel cooled at (a) 10 °C/s (b) 1 °C/s (c) 0.1 °C/s and on HR steel cooled at (d) 10 °C/s (e) 1 °C/s (f) 0.1 °C/s

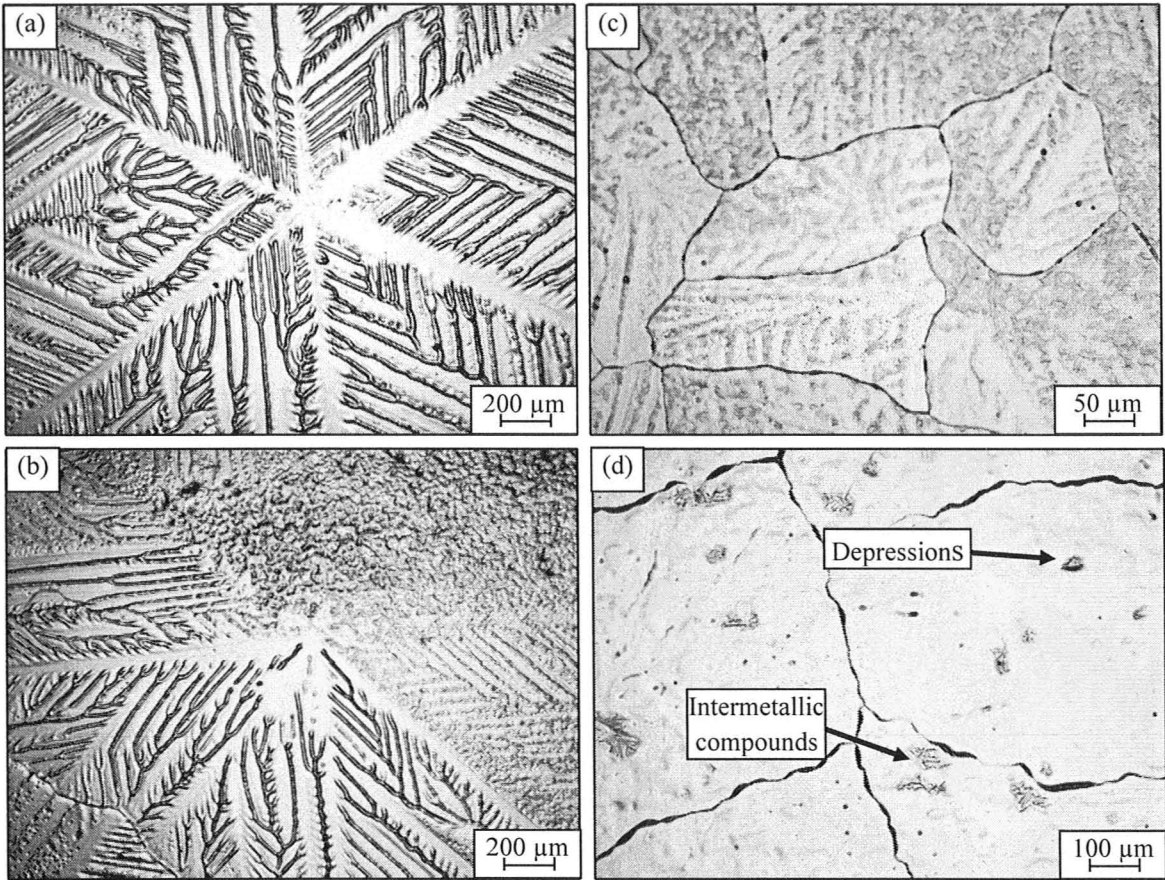


Figure 4-40. Optical micrographs of the (a) shiny (b) semi-shiny spangles on a coated BR surface and (c) semi-shiny (d) dull grains on a coated HR surface cooled at 10 °C/s

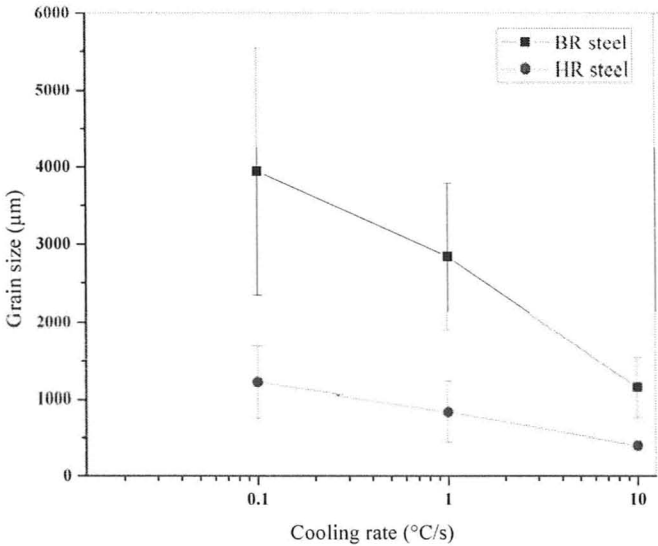


Figure 4-41. Grain size vs. cooling rate for the BR and HR steels

4.3.2. Coating Cross-section Microstructure

Optical microscopy was carried out on the coating cross-sections of BR and HR substrates cooled at 10 °C/s and the results are shown in Figures 4-42(a) and (b). On both substrates, the coating cross-sections exhibited only one layer of zinc grains across the coating thickness. As was mentioned previously, addition of a small amount of Sb lowers the surface tension of the molten zinc bath and as a result only a single layer of zinc grains was formed during coating solidification. It is proposed that the rough surface of the $\text{Fe}_2\text{Al}_5\text{Zn}_x$ interfacial layer was the only active interface for nucleation since the driving force for nucleation was higher at this rough interface as compared to the aluminum oxide surface. Thus, the molten zinc/aluminum oxide surface was most likely inactive during coating solidification since the relative surface energy was small at this interface. It should be mentioned that twins were also observed in the form of inclined features with respect to the steel surface in the optical micrographs of the coatings cross-section. Also, there were not any significant differences in the cross-sectional microstructure for the lower cooling rates and for the HR substrate.

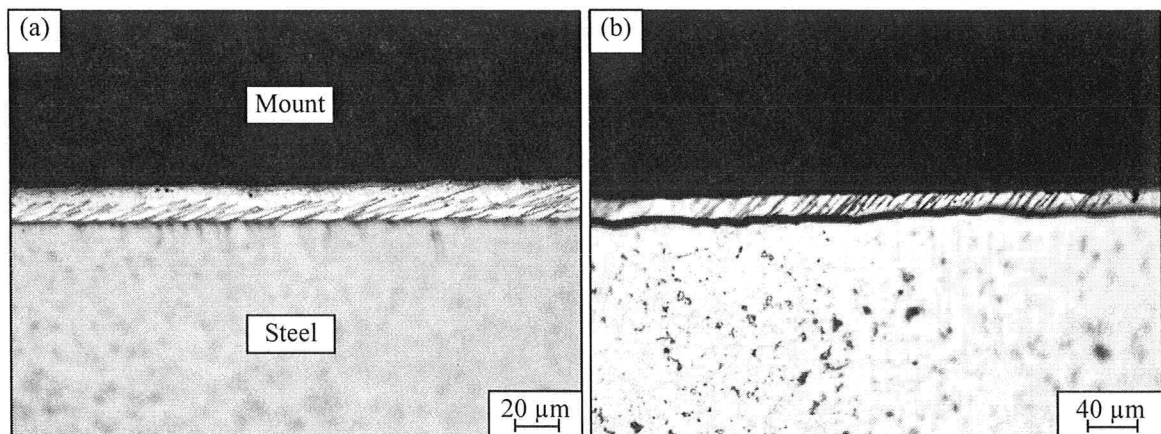


Figure 4-42. Optical micrographs of the coating cross-section at 10 °C/s cooling rate on (a) BR and (b) HR steel substrate

4.3.3. Coating Intermetallics

The SEM-BEIs of the coated BR and HR substrates at all cooling rates showed similar intermetallic particles to those observed on coatings containing 0.01 wt% Sb (Figures 4-43(a-d)). Figures 4-43(a-d) illustrate the intermetallic particles observed in the dendritic, grain boundary and non-dendritic regions on a coated BR steel substrate. According to Figure 4-43(a), the dendritic regions contained the white phase, which was segregated to the interdendritic areas. Also, the same type of intermetallic precipitates in the grain boundaries as shown in Figure 4-43(b). Figures 4-43(c) and (d) illustrate four types of intermetallic precipitates in the non-dendritic regions. The light grey particles with a small round shape, white particles, star-like particles with dark grey contrast and Chinese-script particles with black contrast were found on the coating surface in dull areas.

According to Figures 4-43(a-d), the total amount of white precipitates was higher on these coatings vs. previously discussed samples due to increased amount of Sb in the liquid zinc bath. Also, the reported intermetallic particles were observed on both steel substrates for all cooling conditions. The light grey and white phases were found within the coating thickness as well as on the coating surface while the dark grey and black particles were only detected on the coating surface and mostly in the non-dendritic regions.

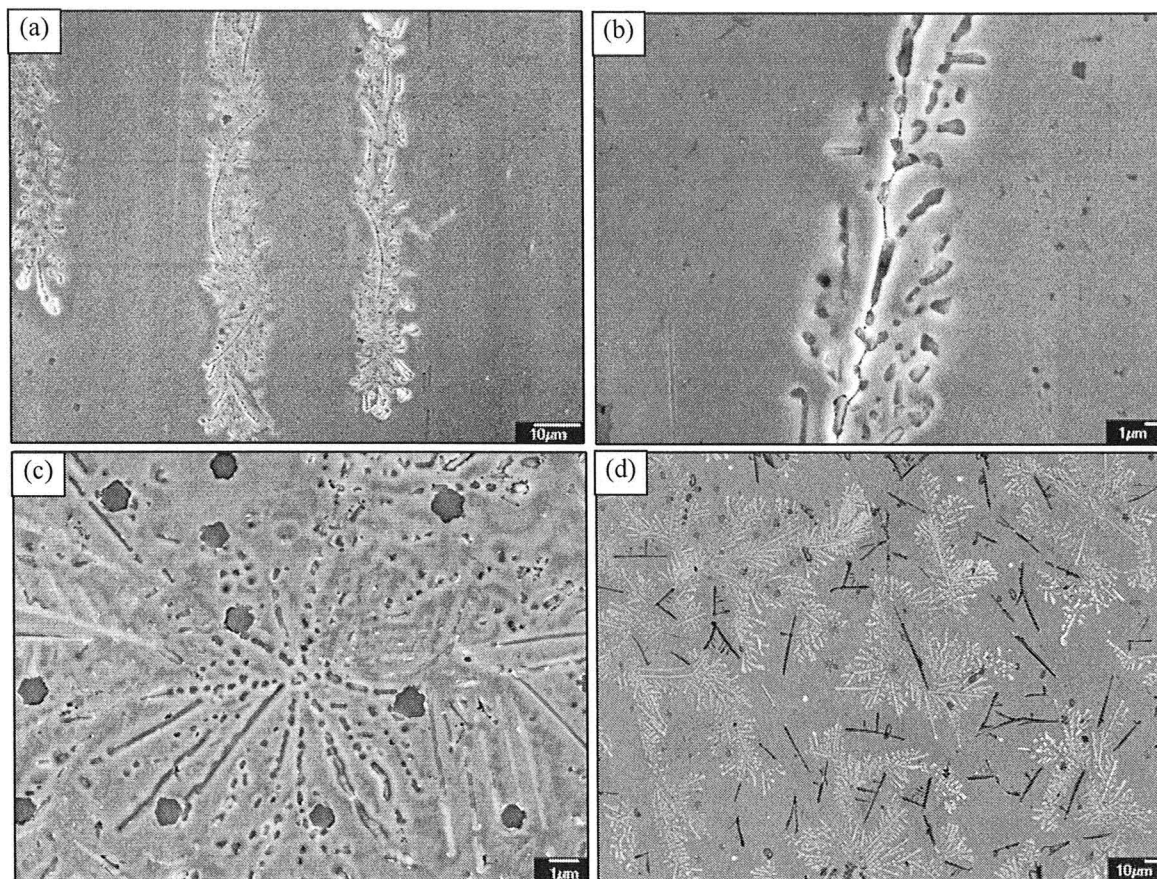


Figure 4-43. SEM-BEIs of the coating microstructure in the (a) dendritic (b) grain boundary and (c-d) non-dendritic region on coated BR steel cooled at 0.1 °C/s

SAM elemental mapping and quantitative point analysis were performed on several regions across the coating surface on a coated BR substrate cooled at 0.1 °C/s. Surface sputter etching removed approximately 7 nm of the coating using the Ar ion beam for 30 s.

The first region selected was located in a non-dendritic region of a zinc spangle which contained a number of elongated intermetallic particles. The SEM-SEI and the corresponding SAM thermal pseudo colour maps are shown in Figures 4-44(a-d). Clearly,

the intermetallic phase was mainly composed of Sb and Al along with a small amount of Zn. According to the point analysis shown in Table 4-5, approximately 50 at% Sb and 30 at% Al along with less than 10 at% Zn were detected in this intermetallic phase which was similar to the findings for similar particles in the lower Sb coatings. A small round particle with grey contrast along with the Al+Sb compounds can be found in the SEM-SEI in Figure 4-45(a). Elemental SAM maps were collected for Zn, Pb, Sn, Al, Cr and Fe and are displayed in Figure 4-45(b-g). It can be seen that Zn, Al and Cr were the main constituents in the grey intermetallic phase. It was also found that the bath impurities such as Pb and Sn were segregated in areas surrounding this intermetallic particle. Quantitative analysis showed high concentrations of Sn and Pb around the edges of the intermetallic particle as shown in Table 4-5.

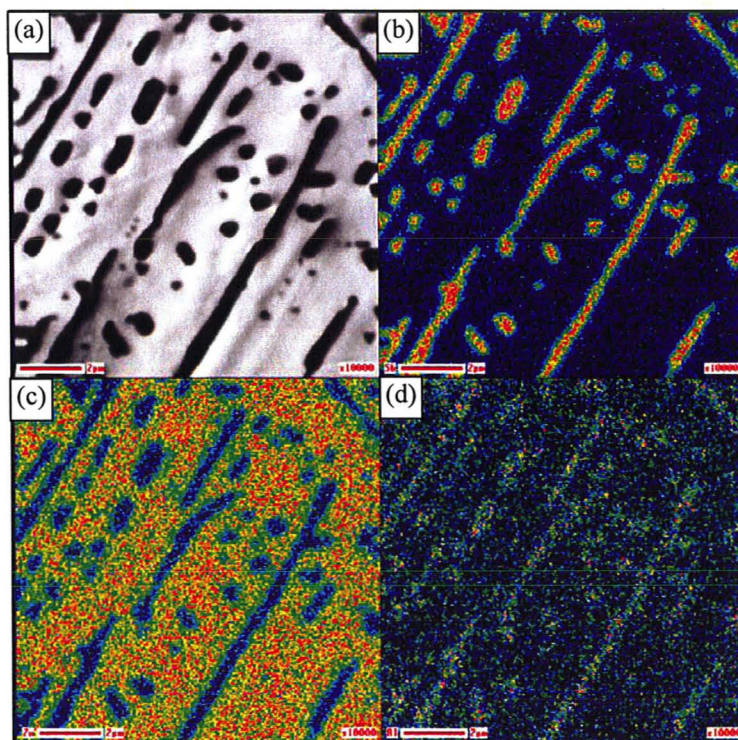


Figure 4-44. (a) SEM-SEI of a coated BR surface cooled at 0.1 °C/s containing elongated particles and (b) Sb (c) Zn and (d) Al SAM maps

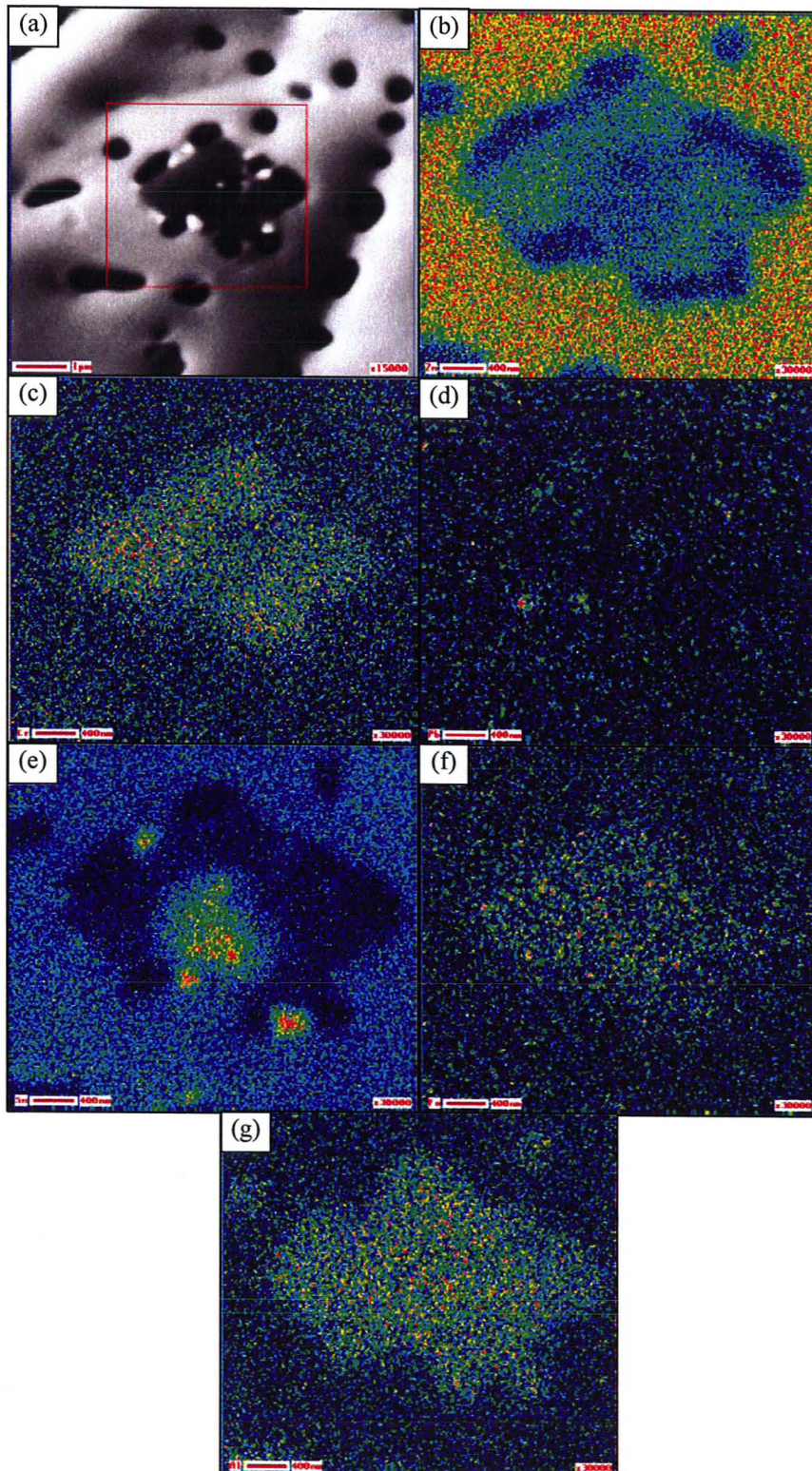


Figure 4-45. (a) SEM-SEI of the coated BR steel surface cooled at 0.1 °C/s containing round particles and (b) Zn (c) Cr (d) Pb (e) Sn (f) Fe and (g) Al SAM maps

Table 4-5. SAM point analysis of the different phases on coated BR steel cooled at 0.1 °C/s (at%)

Phase \ Element	Zn	Sn	Fe	Cr	Al	Sb
Elongated	17.1	4	-	-	30.4	52.5
Round	41.8	25.5	3.6	3.3	23.8	2.1

It should be mentioned that SAM mapping and point analysis were also performed on the star-like and Chinese-script intermetallic precipitates. As was reported previously, the results confirmed the presence of Al, Fe and small quantities of both impurities in both particles (Table 4-3).

4.3.4. Coating Crystallographic Texture

To investigate the microscopic coating crystallographic texture, EBSD orientation mapping was carried out on coated BR and HR steels cooled at 10 °C/s and 0.1 °C/s. The EBSD results for coatings cooled at 1 °C/s were similar to coatings cooled at 0.1 °C/s and, therefore, are not presented here.

Figures 4-46(a-d) and 4-47(a-d) display the microstructural maps, Euler orientation colour maps, pole figures and {0002} pole plot for the coatings on BR steel cooled at 10 °C/s and 0.1 °C/s. As shown, the coating exhibited a strong basal crystallographic texture for both cooling conditions. Figures 4-46(c) and 4-47(c) illustrate the strong basal orientation of the {0002} planes roughly parallel to the steel surface and the symmetrical distribution of the $\{10\bar{1}0\}$ and $\{10\bar{1}3\}$ planes, representing the strong

$\langle 0001 \rangle$ fiber texture for the coatings. The inclination angle of the $\{0002\}$ planes was approximately $10\text{-}15^\circ$ with respect to the steel surface.

Similar crystallographic texture was observed for coatings on HR substrates cooled at 10°C/s , as shown in Figures 4-48(a-d). According to the $\{0002\}$ pole figures, coatings had a preferred basal crystallographic texture with the average inclination angle of $15\text{-}20^\circ$ with respect to the steel surface. On the other hand, coated HR steel cooled at 0.1°C/s exhibited a much more random crystallographic texture (Figures 4-49(a-d)).

Table 4-6 shows the area percentage of basal zinc grains inclined for $0\text{-}15^\circ$ relative to the steel sheet for the BR and HR steels at 10°C/s and 0.1°C/s cooling rates. As can be seen, there is a significant difference between the area percentage of basal grains for the BR and HR steels at each cooling rate.

In conclusion, regardless of the type of steel substrate, zinc coatings containing 0.03 wt% Sb exhibited clear basal crystallographic texture for all cooling conditions.

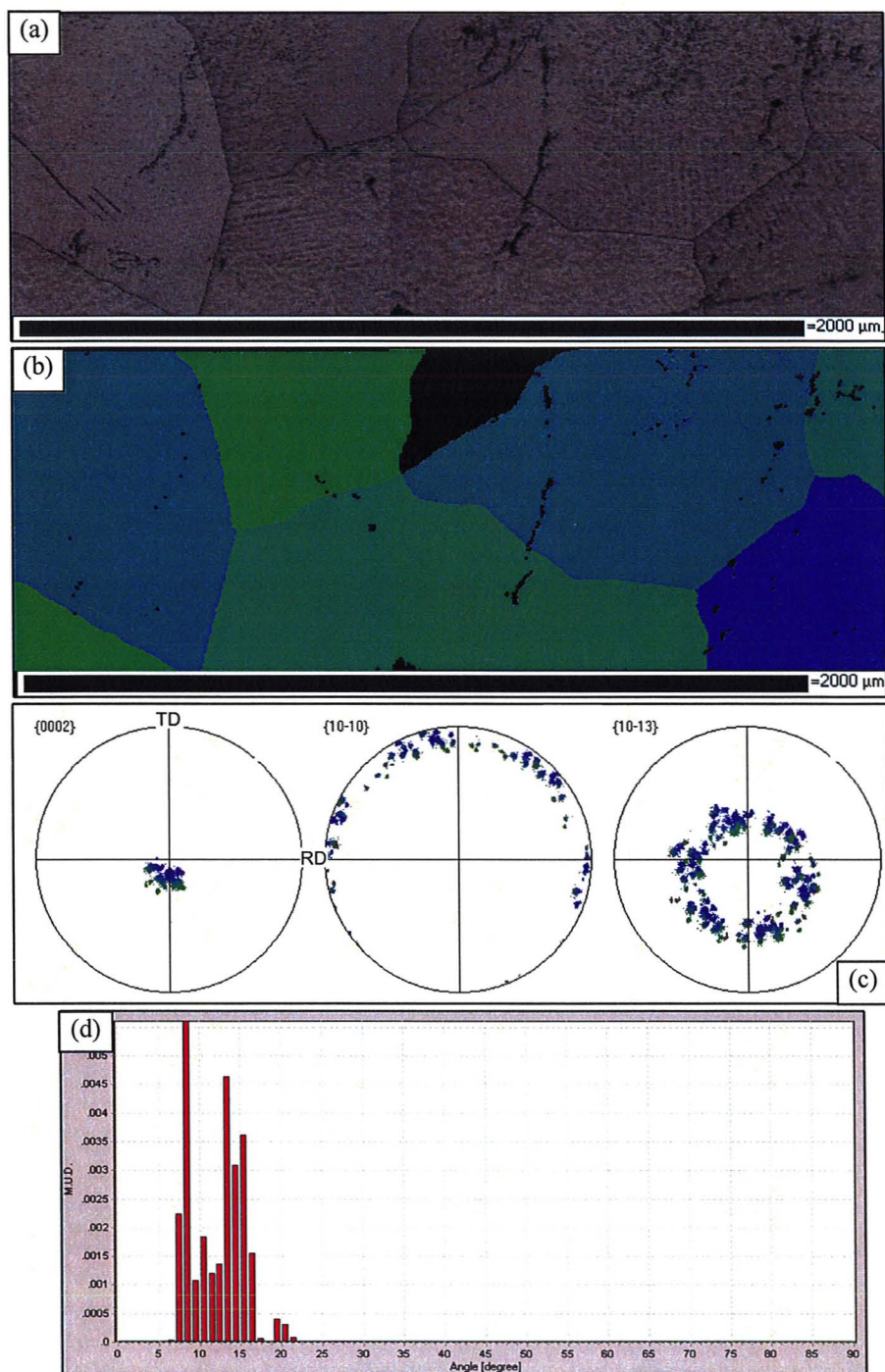


Figure 4-46. (a) Microstructural map (b) Euler orientation colour map (c) pole figures and (d) {0002} pole plot of a coating on a BR steel cooled at 10 °C/s

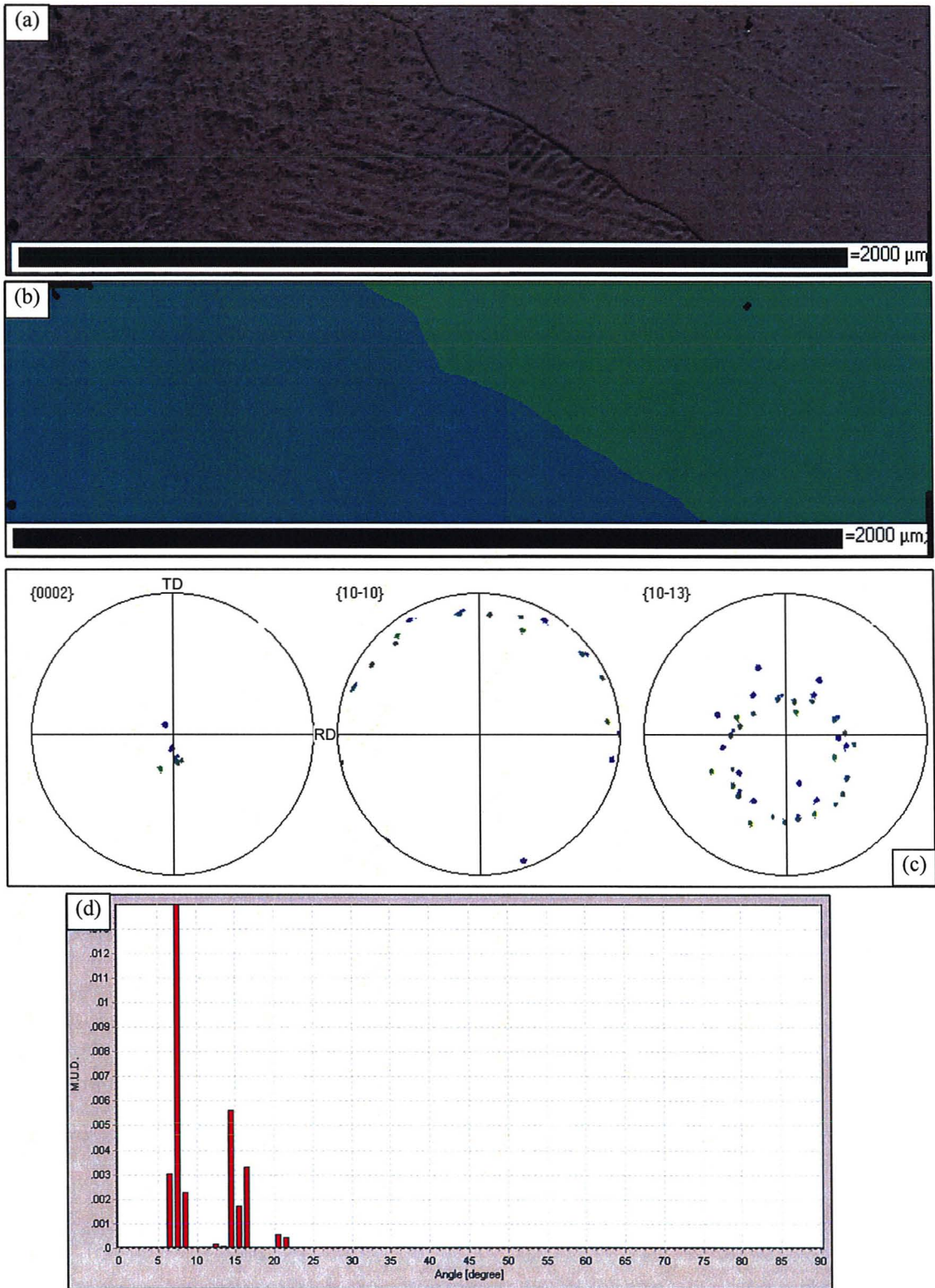


Figure 4-47. (a) Microstructural map (b) Euler orientation colour map (c) pole figures and (d) {0002} pole plot of a coating surface on a BR steel cooled at 0.1 °C/s

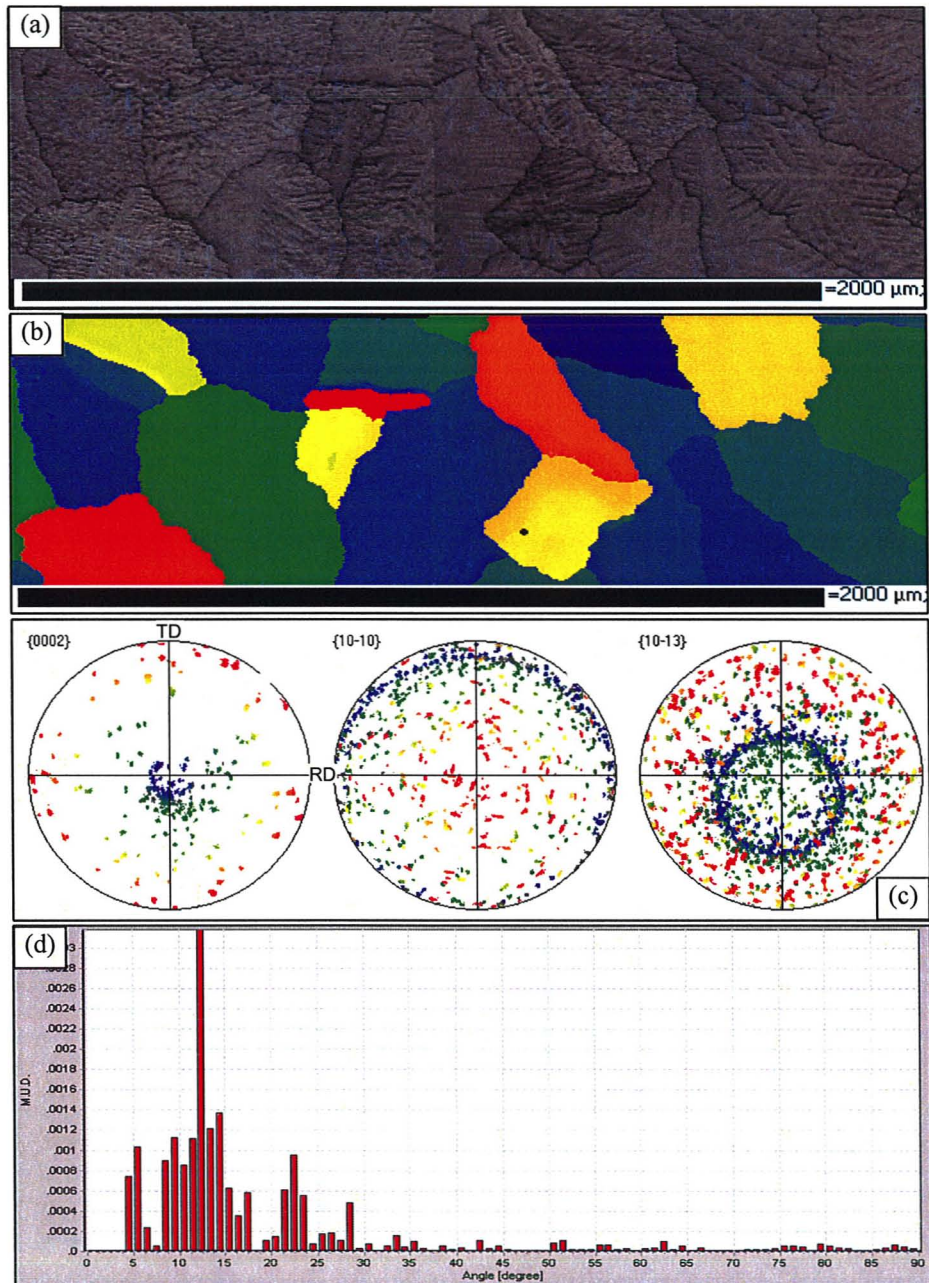


Figure 4-48. (a) Microstructural map (b) Euler orientation colour map (c) pole figures and (d) $\{0002\}$ pole plot of a coating surface section on a HR steel cooled at $10\text{ }^{\circ}\text{C/s}$

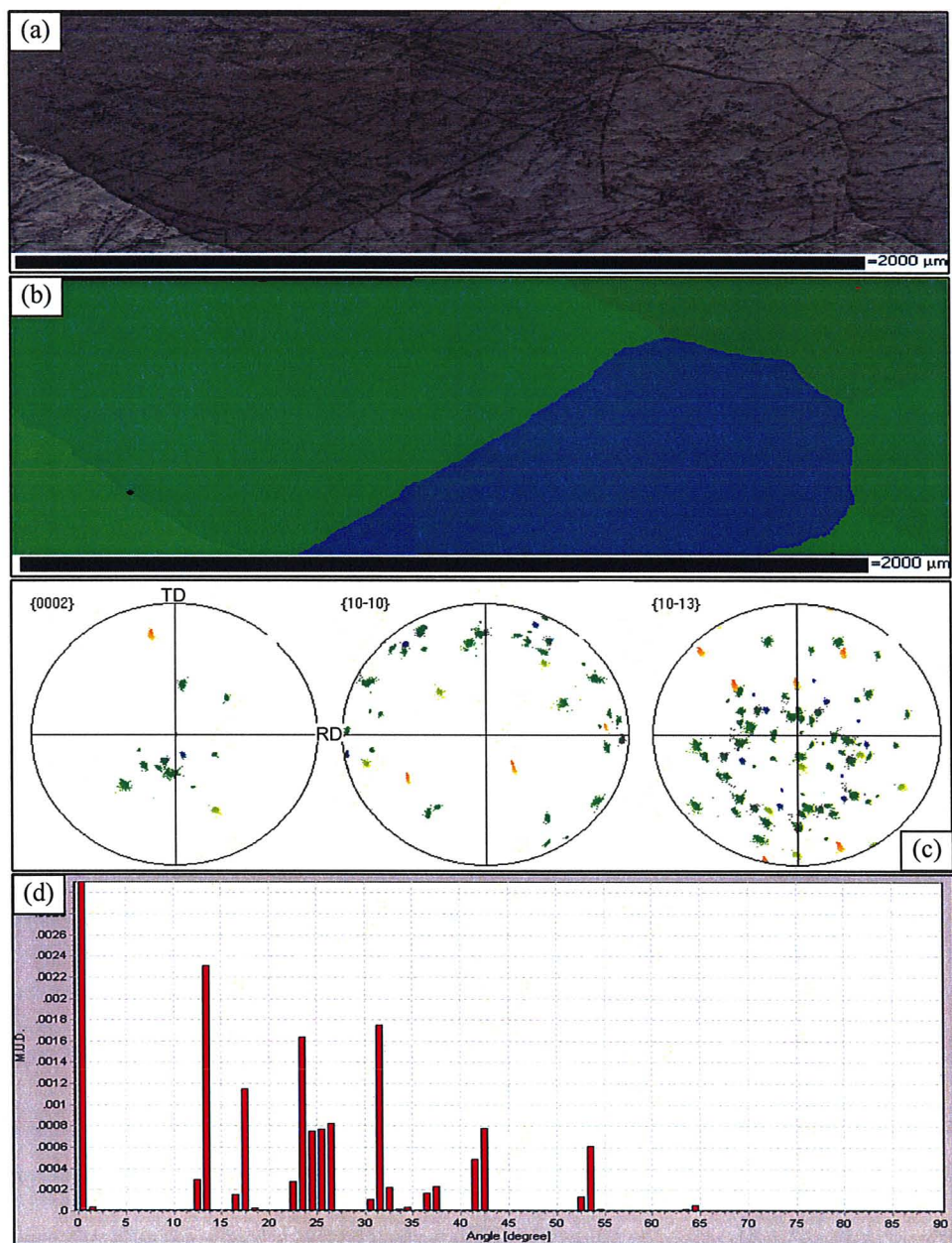


Figure 4-49. (a) Microstructural map (b) Euler orientation colour map (c) pole figures and (d) $\{0002\}$ pole plot of a coating surface on a HR steel cooled at $0.1\text{ }^{\circ}\text{C/s}$

Table 4-6. Area percentage of basal zinc grains inclined for $0\text{-}15^{\circ}$ relative to the steel sheet (%)

Steel substrate	Cooling rate ($^{\circ}\text{C/s}$)	
	10	0.1
BR	46.7	43.9
HR	21.8	11.3

4.4. 0.1 wt% Sb Alloy

4.4.1. Coating Surface Microstructure

Following the experimental matrix shown in Table 3-1, dipping experiments were carried out in a molten zinc bath containing 0.1 wt% Sb. Optical images of the as-cast coating surface on BR and HR substrates for all cooling conditions are shown in Figures 4-50(a-f).

The coating surface microstructure on the BR substrate cooled at 10 °C/s, 1 °C/s and 0.1 °C/s are shown in Figures 4-50(a-c). Most spangles were non-symmetric and were divided into a number of segments with a bright and dark appearance. The coating surface was dendritic, relatively smooth and reflective in the bright segments. On the other hand, the coating surface was non-dendritic, rough and non-reflective in the dark segments. Regarding the coating morphology, the coating surface consisted mainly of dimpled areas characterized by the presence of randomly distributed intermetallic precipitates. However, shiny and feathery morphologies were also detected on the coating surface as seen in Figures 4-51(a-c). Also, ridged or orthogonal-dendritic spangles could not be found on the coated BR steel at any cooling condition.

Interestingly, similar spangle microstructures were also found on the coating surface of the HR substrates for all cooling rates, as illustrated in Figures 4-50(d-f) and 4-51(a-d). At the 10 °C/s cooling rate, the coating exhibited symmetrical flowery zinc spangles as well as non-symmetrical spangles. Flowery spangles were reflective while other spangles were non-reflective (Figure 4-50(d)). Spangles on the surface of the 1 °C/s

and 0.1 °C/s cooled samples were largely non-symmetrical and non-dendritic, as shown in Figures 4-51(e) and (f). Regarding spangle morphology, most of the spangles exhibited a dark appearance along with a few shiny dendritic branches.

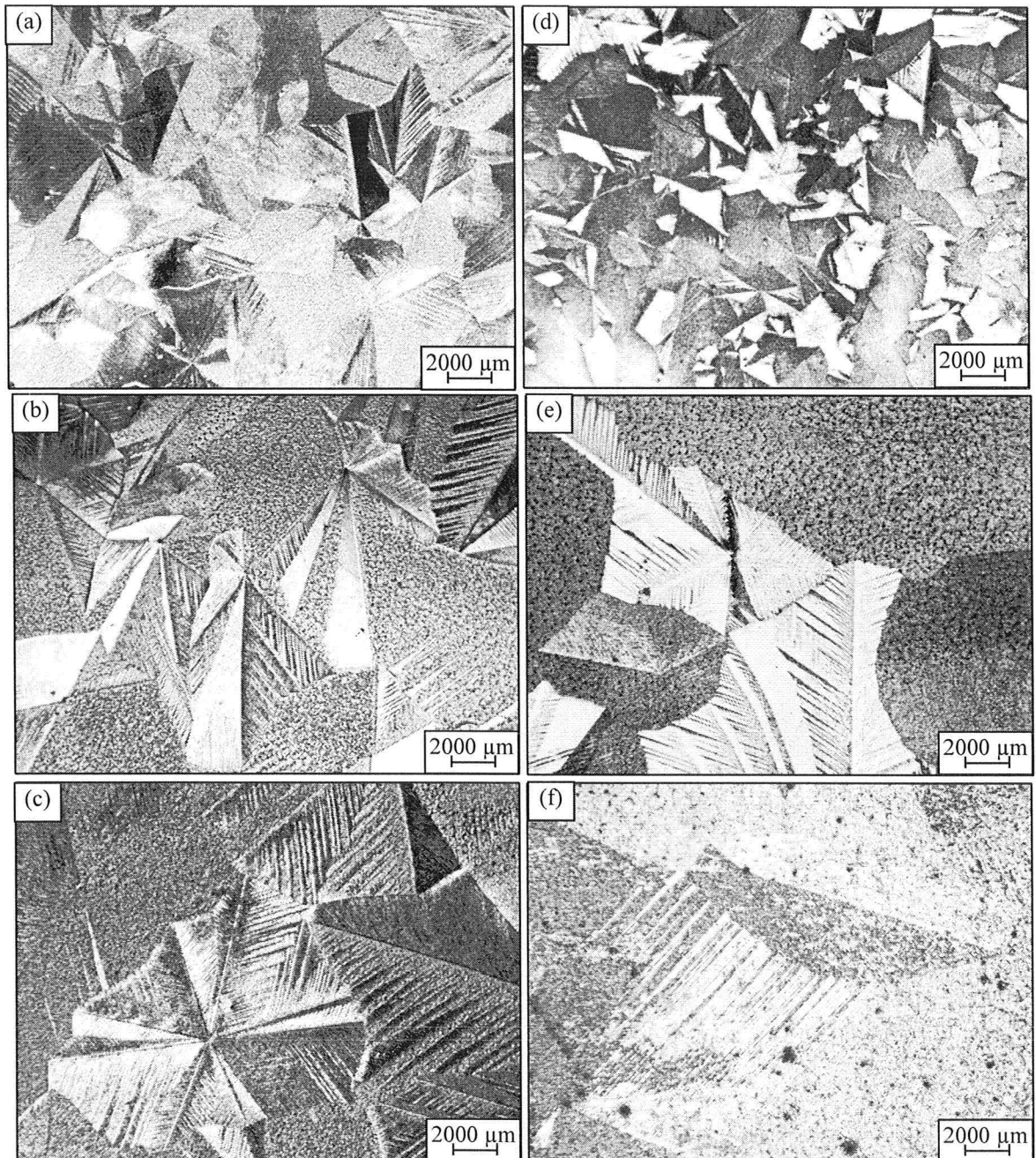


Figure 4-50. Low magnification optical micrographs of the as-cast coating surface containing 0.1 wt% Sb on BR steel cooled at (a) 10 °C/s (b) 1 °C/s (c) 0.1 °C/s and on HR steel cooled at (d) 10 °C/s (e) 1 °C/s (f) 0.1 °C/s

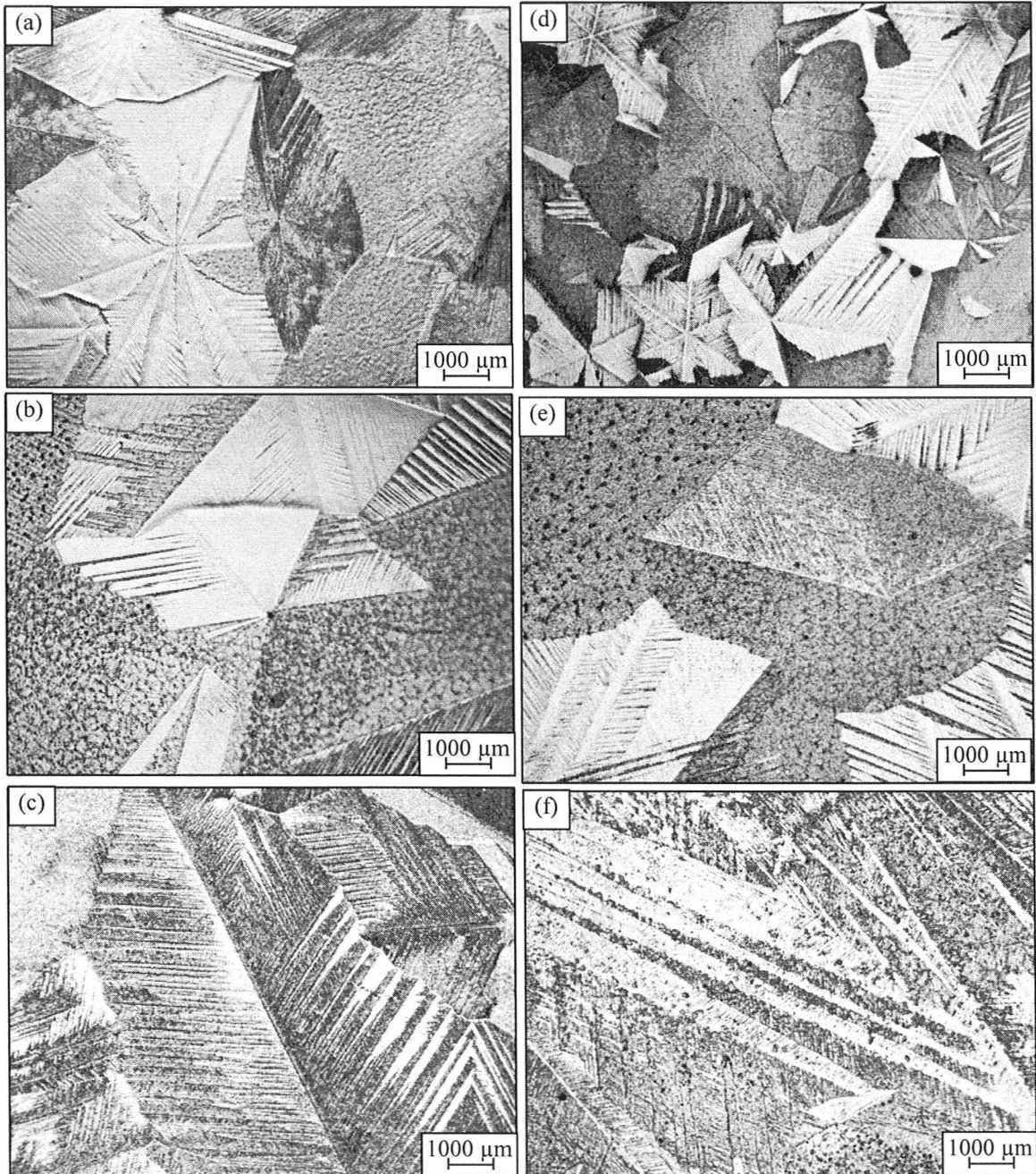


Figure 4-51. Optical micrographs of the as-cast coating surface containing 0.1 wt% Sb on BR steel cooled at (a) 10 °C/s (b) 1 °C/s (c) 0.1 °C/s and on HR steel cooled at (d) 10 °C/s (e) 1 °C/s (f) 0.1 °C/s

Optical micrographs of the dendritic and non-dendritic regions on both substrates were shown in Figures 4-52(a) and (b). As can be seen, intermetallic phases were present

in interdendritic regions while the dendrite branches were depleted of any precipitates. As a result, the interdendritic regions had a bright appearance and shiny morphology. The intermetallic precipitates were distributed randomly across the non-dendritic surface as shown in Figure 4-52(b) and, therefore, the non-dendritic regions had a dark appearance and dull morphology. In general, the coating surface was darker in the case of the HR steel substrate as compared to the BR steel, which was most likely due to the HR steel surface roughness. Furthermore, it was found that zinc grains were smaller on the HR steel as compared to the BR steel at the same cooling rate. Also, higher cooling rates resulted in smaller grains on both substrates (Figure 4-53).

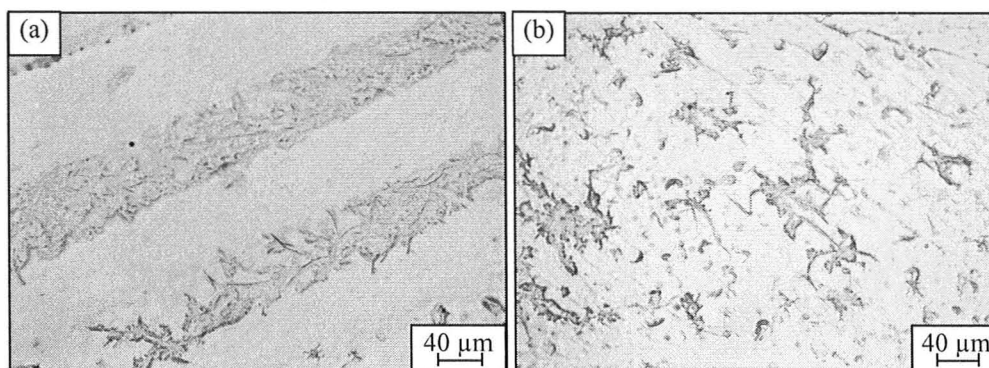


Figure 4-52. High magnification optical micrographs of the (a) dendritic and (b) non-dendritic regions on a coated BR steel cooled at 10 °C/s

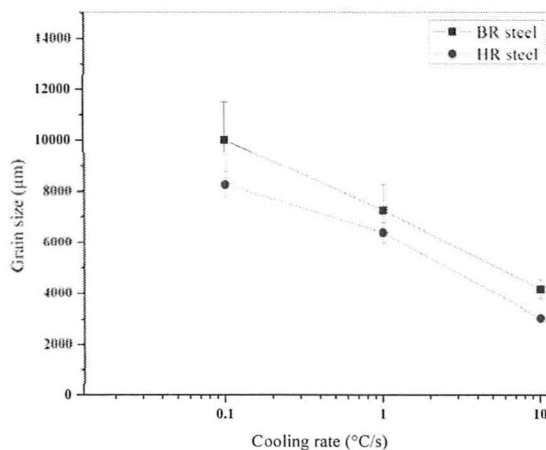


Figure 4-53. Grain size vs. cooling rate for BR and HR steels

4.4.2. Coating Cross-section Microstructure

Microstructural observations of the coating cross-section on the BR and HR steel substrates at different cooling rates showed the presence of a single layer of zinc grains across the coating thickness. Following the discussion on the mechanism of zinc grain formation in coatings containing 0.03 wt% Sb, it is proposed that nucleation was more favourable on the rough steel/liquid zinc interface as compared to the liquid zinc/aluminum oxide interface and, therefore, zinc nuclei were formed on $\text{Fe}_2\text{Al}_5\text{Zn}_x$ crystals at the onset of solidification. Zinc nucleation was followed by a dendritic growth on the plane of the steel substrate two dimensionally. Solidification was complete once the zinc grains reached the free surface of the liquid coating.

4.4.3. Coating Intermetallics

To investigate the coating intermetallic phases, microstructural observations were carried out on the coated BR and HR steels using SEM and SAM for the various cooling conditions. Figures 4-54(a-d) display the SEM-BEIs of the dendritic, grain boundary and non-dendritic regions on a coated BR steel cooled at 0.1 °C/s. Based on the particle contrast and morphology, it was deduced that the coating contained similar intermetallic phases as those previously observed in coatings containing smaller amounts of Sb. The small round particles with light grey contrast, the white phase, the star-like particles with dark grey contrast and the Chinese-script particles with a black contrast were found in all coatings.

Figure 4-54(a) illustrates the presence of the white particles in interdendritic regions while the main dendrite arms were depleted of any intermetallic precipitates. A mixture of white and light grey phases was detected in grain boundary regions as shown in Figure 4-54(b). In addition, Figures 4-54(c) and (d) show all four types of previously observed intermetallic compounds in a non-dendritic region. In non-dendritic regions, the intermetallic precipitates covered a large proportion of the coating surface, resulting in the dull morphology and dark appearance of these areas.

It should be mentioned that the reported intermetallic phases were also detected on the coated HR steel for all cooling conditions. The only difference was that the size of the particles was smaller in the case of the more rapidly cooled samples.

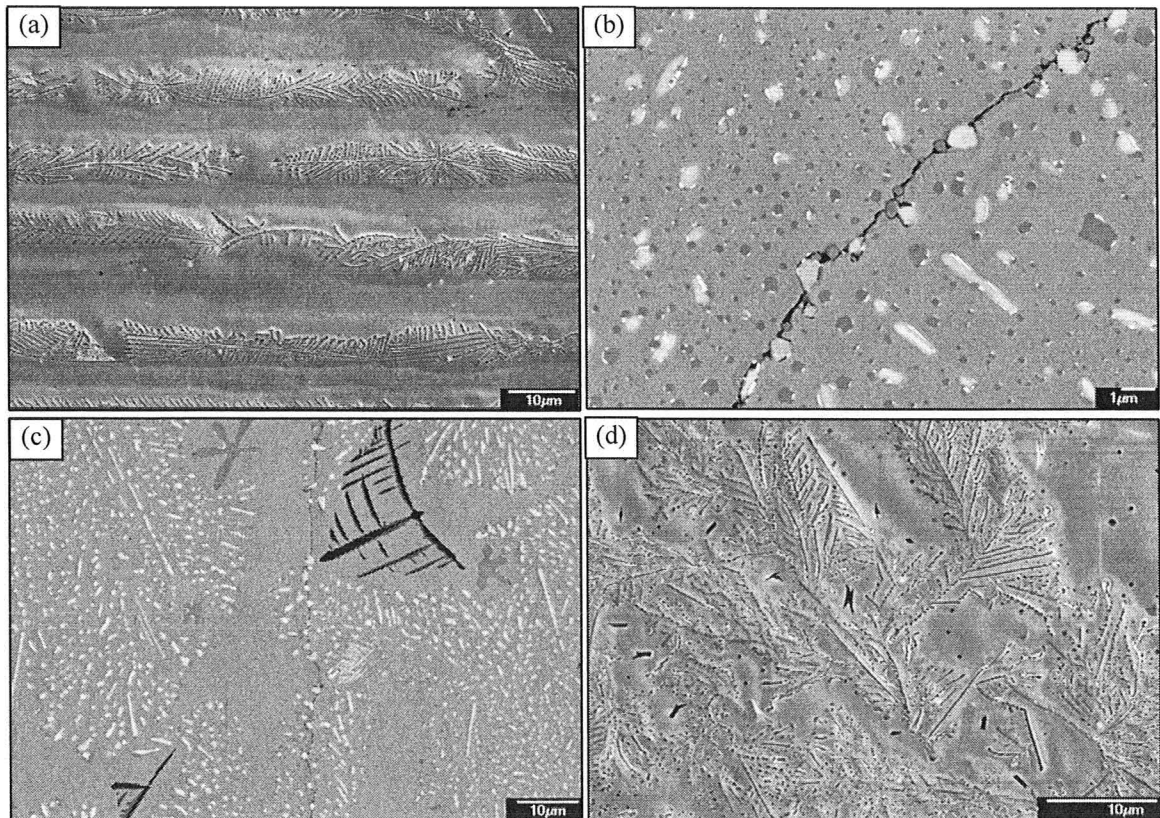


Figure 4-54. SEM-BEIs of the intermetallics on (a) dendritic (b) grain boundary and (c-d) non-dendritic regions on a coated BR steel cooled at 0.1 °C/s

Further chemical analysis was carried out by SAM on coated BR and HR steels to confirm the chemical composition of each phase. Using the Ar ion beam, an area of interest was sputtered for 30 s and SAM elemental maps acquired for Zn, Al and Sb and the results shown in Figures 4-55(a-d). It was determined that the intermetallic particles in shiny and dull regions were mainly composed of Sb and Al along with small amounts of Zn. Figure 4-55(e) shows the corresponding Auger colour overlay image which confirmed the presence of Zn, Al and Sb as well as Al+Sb intermetallic particles.

For finer scale observations of the elemental distribution between the intermetallic particles, SAM elemental mapping was carried out over the area within the yellow square in the SEM-SEIs shown in Figures 4-56(a-b). As shown, this area contained two intermetallic phases which were the irregular precipitates and a star-like particle. Figures 4-56(c-f) illustrate the Zn, Al, Sb and Sn SAM elemental maps. Accordingly, the irregular intermetallic particles were Zn depleted while they were Al and Sb enriched. On the other hand, the star-like particle contained Zn and Al. Also, Sn segregation was detected in areas around both of the intermetallic particles. The Auger colour overlay images in Figures 4-56(g-i) confirmed the presence of a Al+Sb compound in the irregular intermetallic precipitates and Al and Zn in the star-like particle. For both types of intermetallic particles, Sn was detected in areas surrounding the Al.

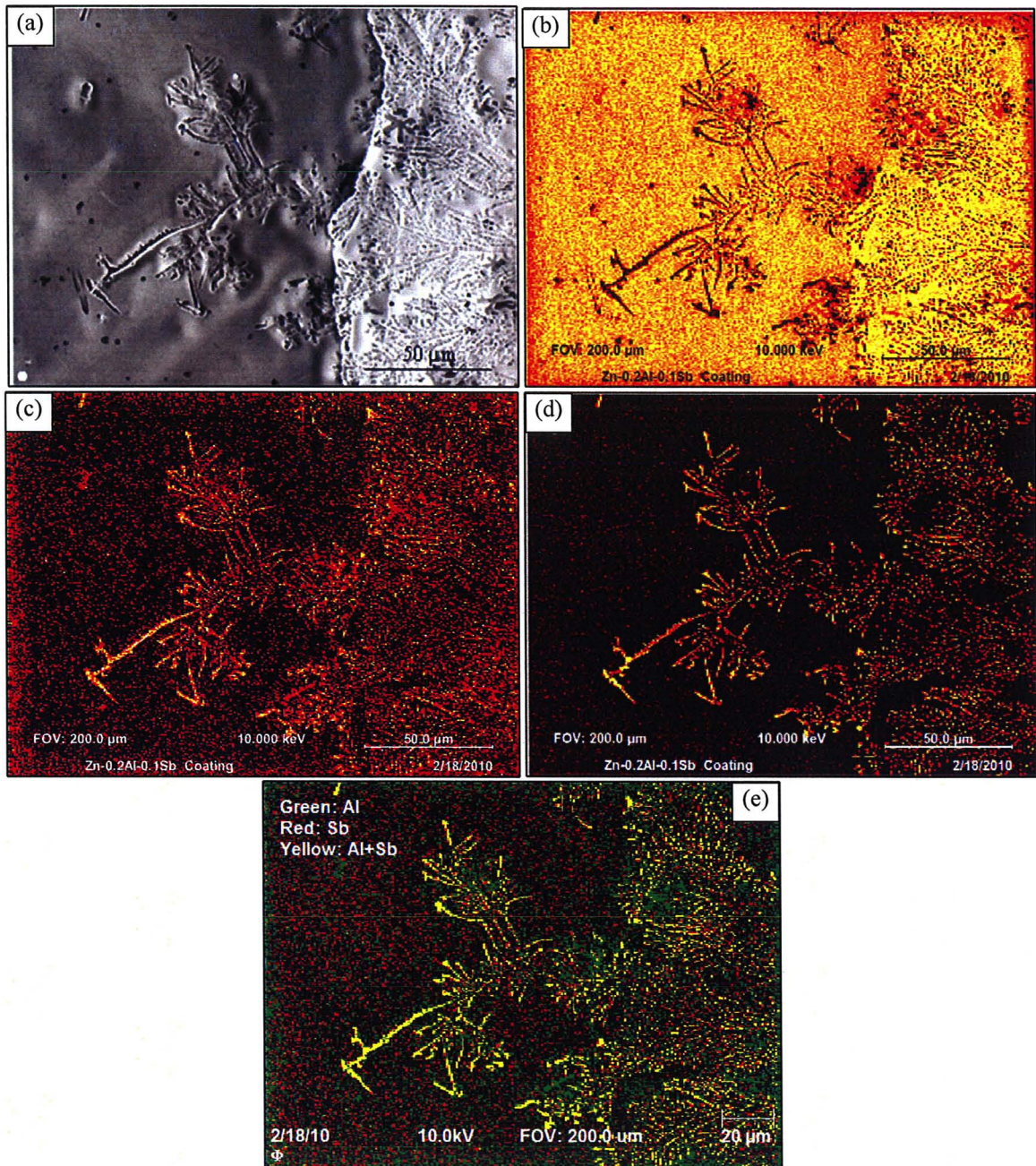


Figure 4-55. (a) SEM-SEI of the shiny and dull regions on a coated BR steel surface cooled at 0.1 °C/s and (b) Zn (c) Al (d) Sb SAM maps and (e) Auger colour overlay image

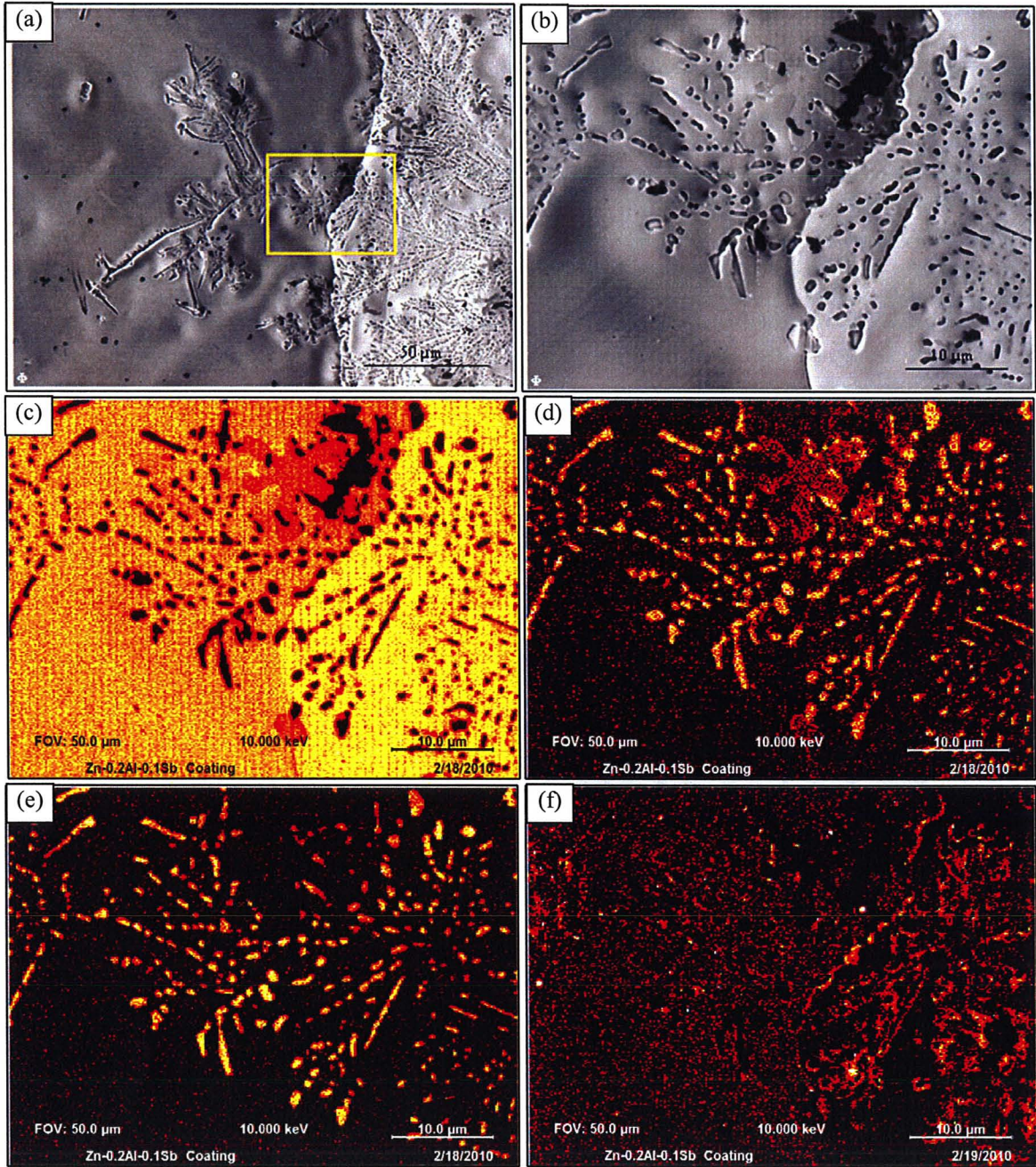


Figure 4-56. (a-b) SEM-SEI of the shiny and dull regions on the sputtered coated BR steel surface cooled at 0.1 °C/s (c) Zn (d) Al (e) Sb and (f) Sn SAM maps

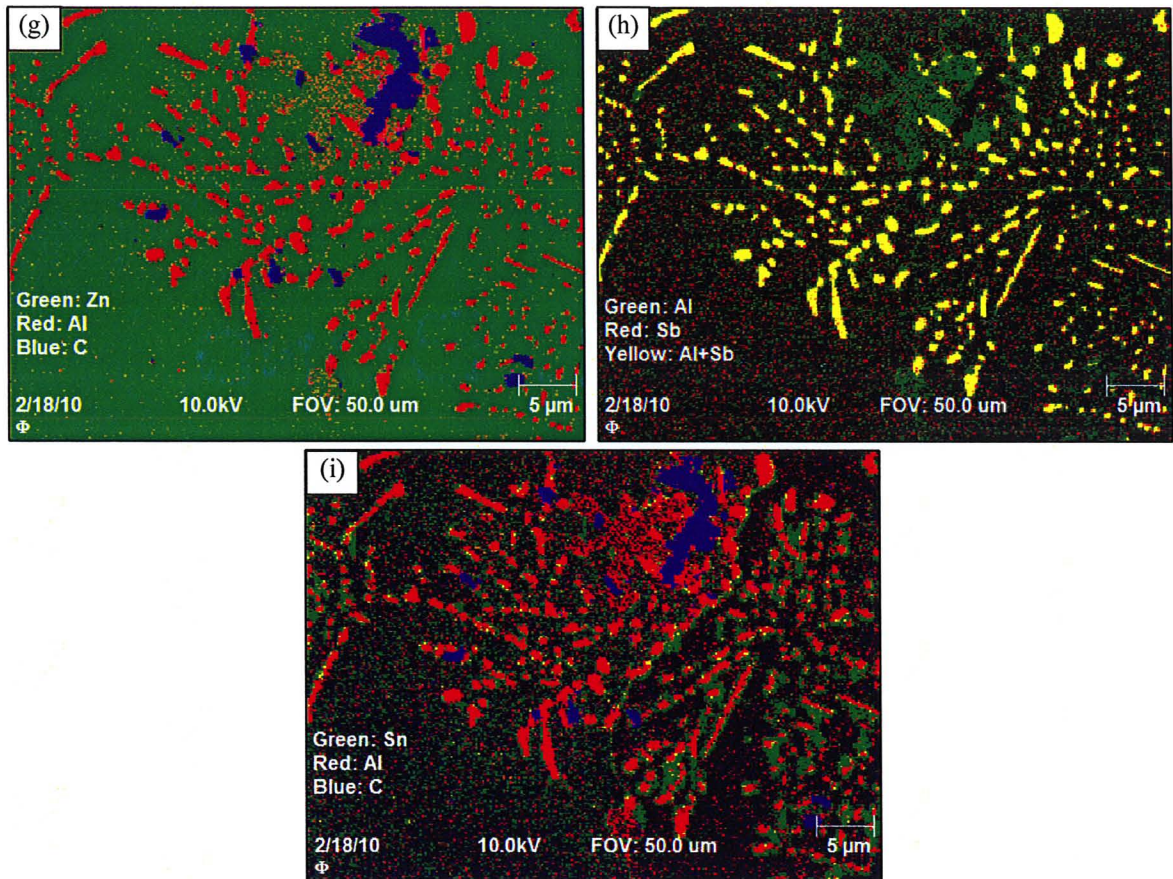


Figure 4-56. (Cont'd) (g-i) Auger colour overlay images

Figures 4-57(a-d) show the SEM-SEIs of an Al+Sb intermetallic particle which exhibited high concentrations of Sn. To study the distribution of Zn, Al, Sb and Sn in this particle, SAM elemental maps as well as SAM colour overlay images were collected and are shown in Figures 4-57(e-j). As expected, the examined intermetallic precipitate was mainly made up of Al and Sb. Also Sn was segregated in the form of small particle adjacent to the Al+Sb compound.

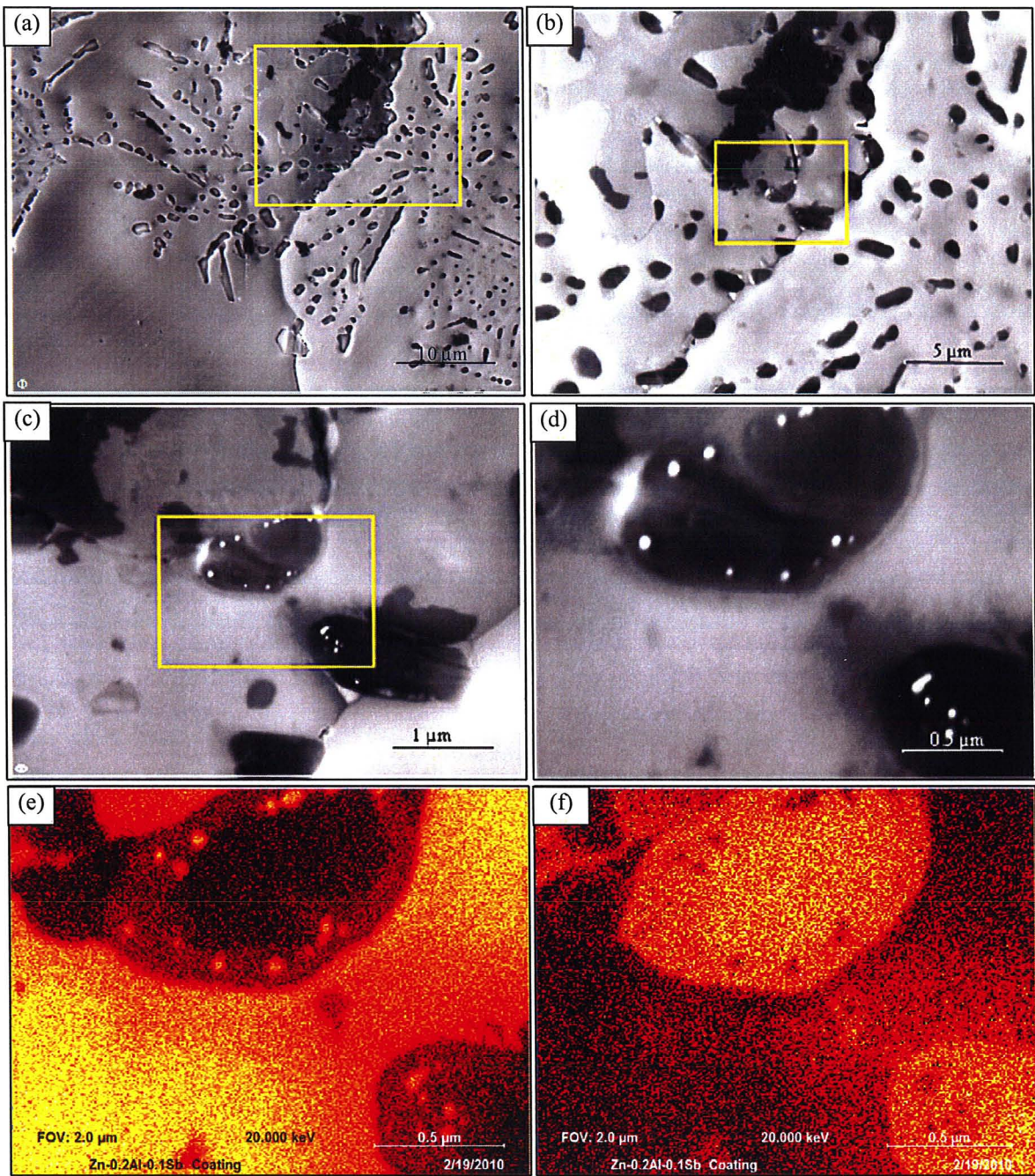


Figure 4-57. (a-d) SEM-SEIs of a precipitate (e) Zn and (f) Al SAM maps

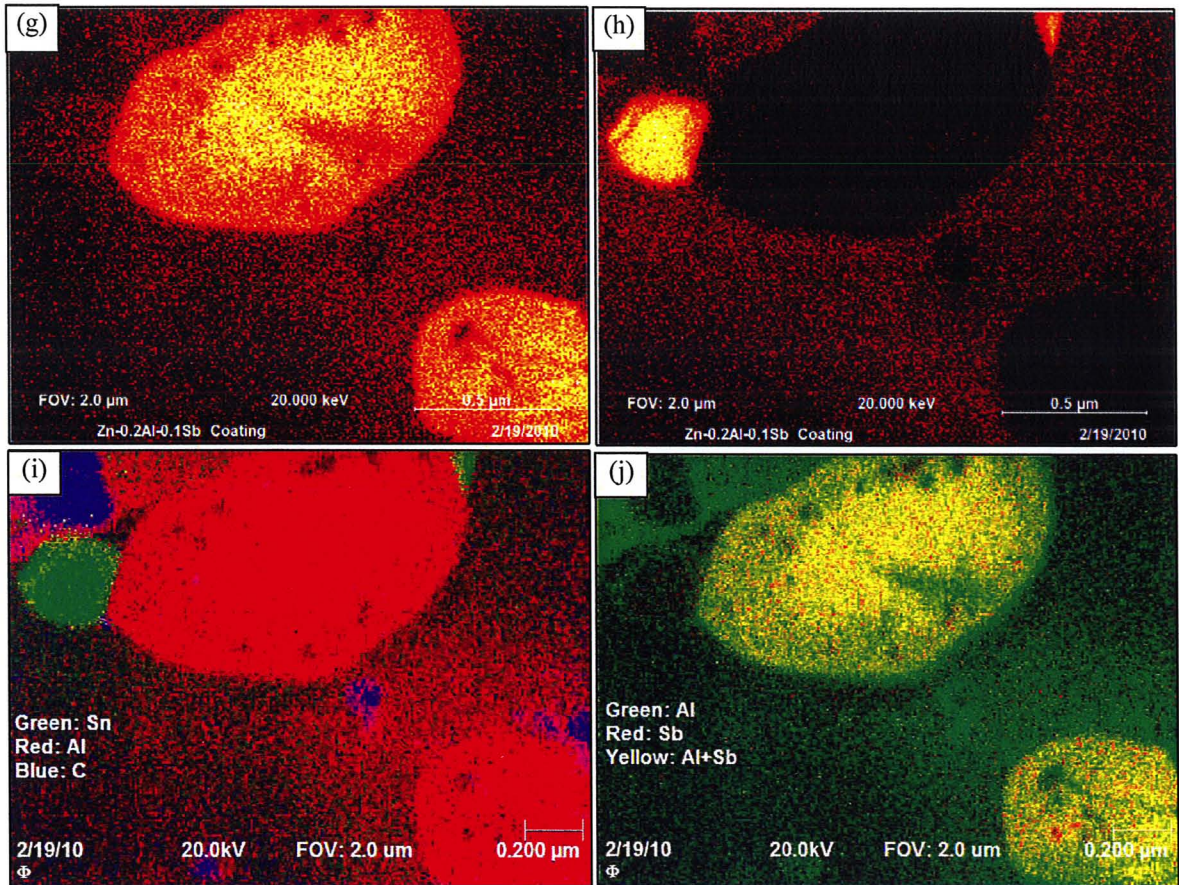


Figure 4-57. (Cont'd) (g) Sb (h) Sn SAM maps and (i-j) Auger colour overlay images

The last area of interest for Auger analysis was selected in a shiny region and is shown in Figures 4-58(a-b). The SAM thermal pseudo colour maps for Sn and Pb as well as Auger colour overlay images were obtained and shown in Figures 4-58(c-f). It was found that Pb and Sn were accumulated in areas around the AlSb particle.

Based on the above SAM results, it was concluded that in coatings containing 0.1 wt% Sb, the bath impurities such as Pb and Sn were mainly segregated in areas around the AlSb intermetallic phase.

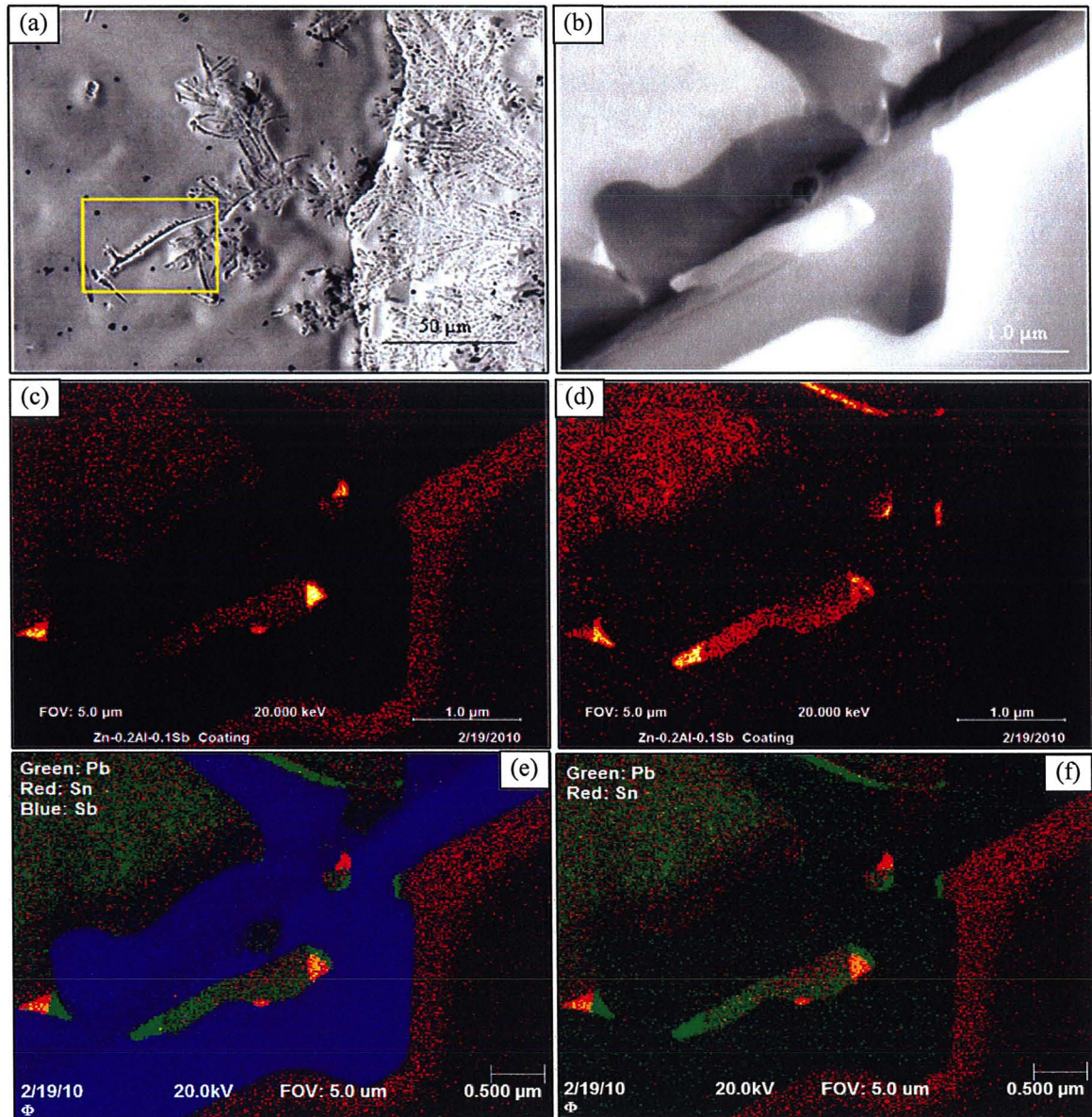


Figure 4-58. (a-b) SEM-SEIs of a particle in a shiny region (c) Sn (d) Pb SAM maps and (e-f) Auger colour overlay images

4.4.4. Coating Crystallographic Texture

The crystallographic texture of the coatings on BR and HR steels cooled at 10 °C/s and 0.1 °C/s were investigated using EBSD. Figures 4-59(a-d) and 4-60(a-d) show the microstructural maps, Euler orientation colour maps, pole figures and $\{0002\}$ pole

plots for coated BR steels cooled at 10 °C/s and 0.1 °C/s, respectively. As can be seen, both coatings exhibited strong basal crystallographic texture with {0002} basal planes inclined less than 10° with respect to the steel surface.

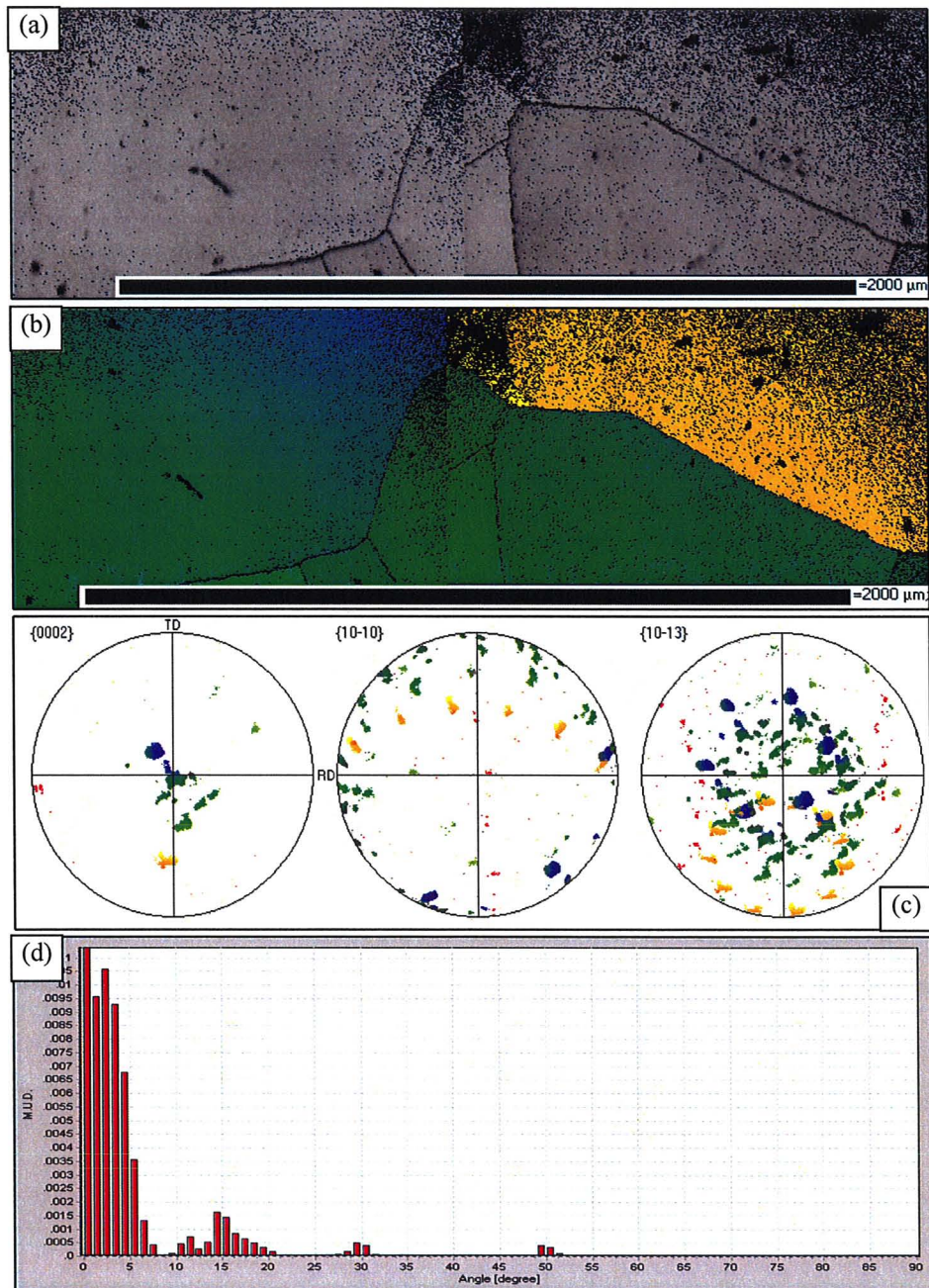


Figure 4-59. (a) Microstructural map (b) Euler orientation colour map (c) pole figures and (d) {0002} pole plot of a coating surface section on a BR steel cooled at 10 °C/s

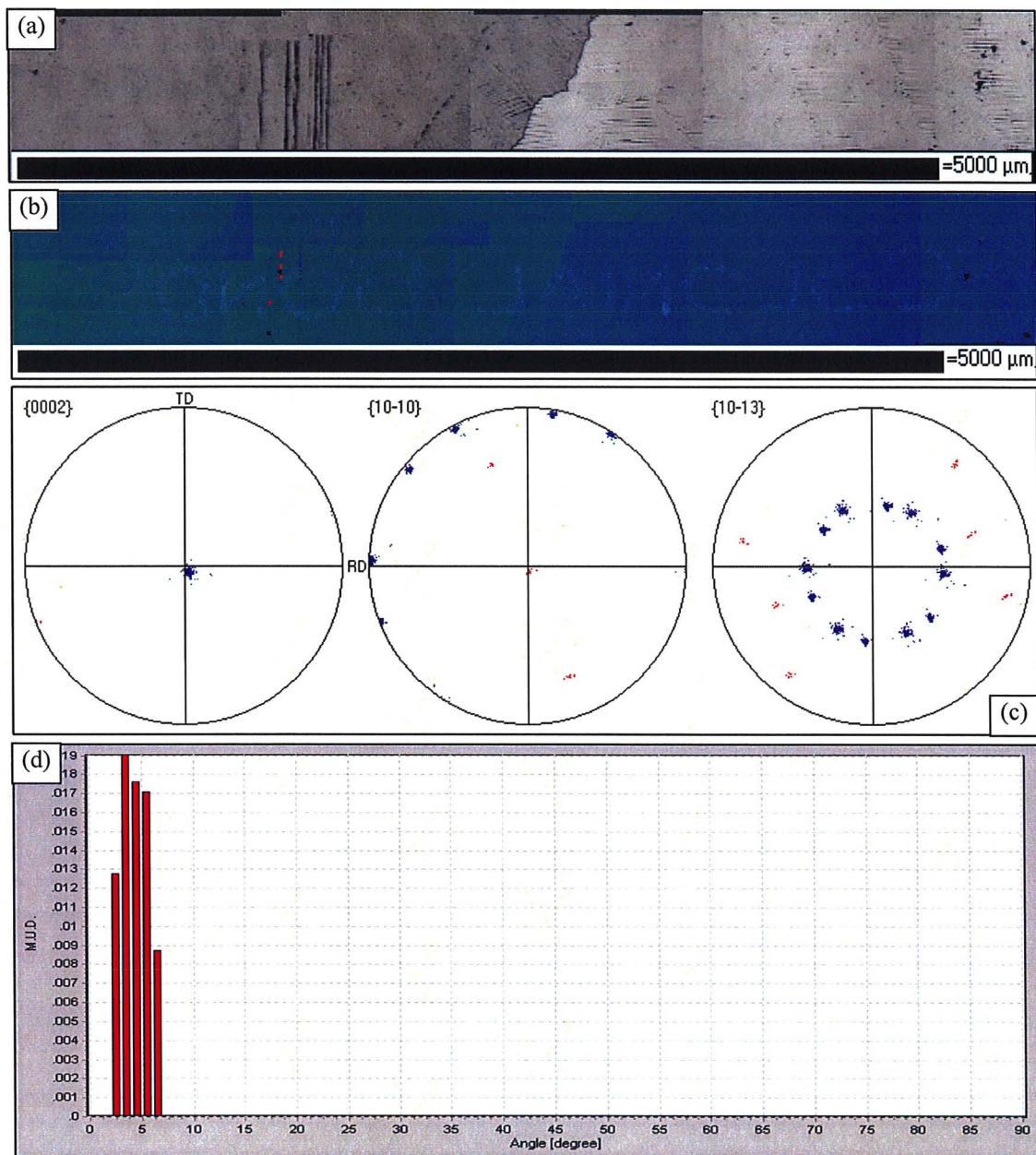


Figure 4-60. (a) Microstructural map (b) Euler orientation colour map (c) pole figures and (d) {0002} pole plot of a coating surface section on a BR steel cooled at 0.1 °C/s

Figures 4-61(a-d) and 4-62(a-d) represent the EBSD results for coatings on HR steels cooled at 10 °C/s and 0.1 °C/s, respectively. For both cases, coatings exhibited strong basal crystallographic texture with an average inclination angle of 5-15° relative to the steel surface. Table 4-7 shows the area percentage of basal zinc grains inclined for 0-15° relative to the steel sheet for the BR and HR steels at 10 °C/s and 0.1 °C/s cooling rates.

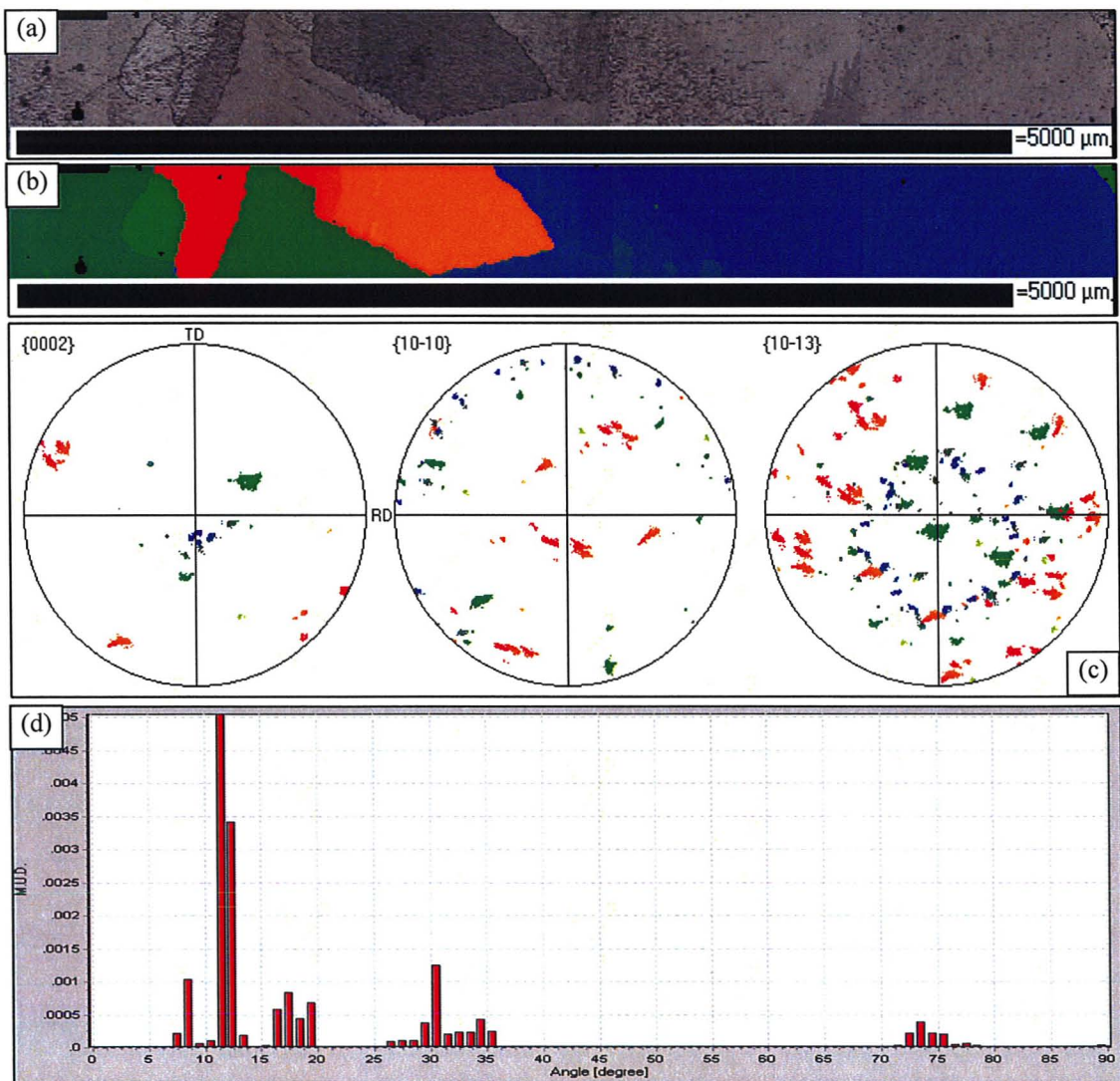


Figure 4-61. (a) Microstructural map (b) Euler orientation colour map (c) pole figures and (d) {0002} pole plot of a coating surface section on a HR steel cooled at 10 °C/s

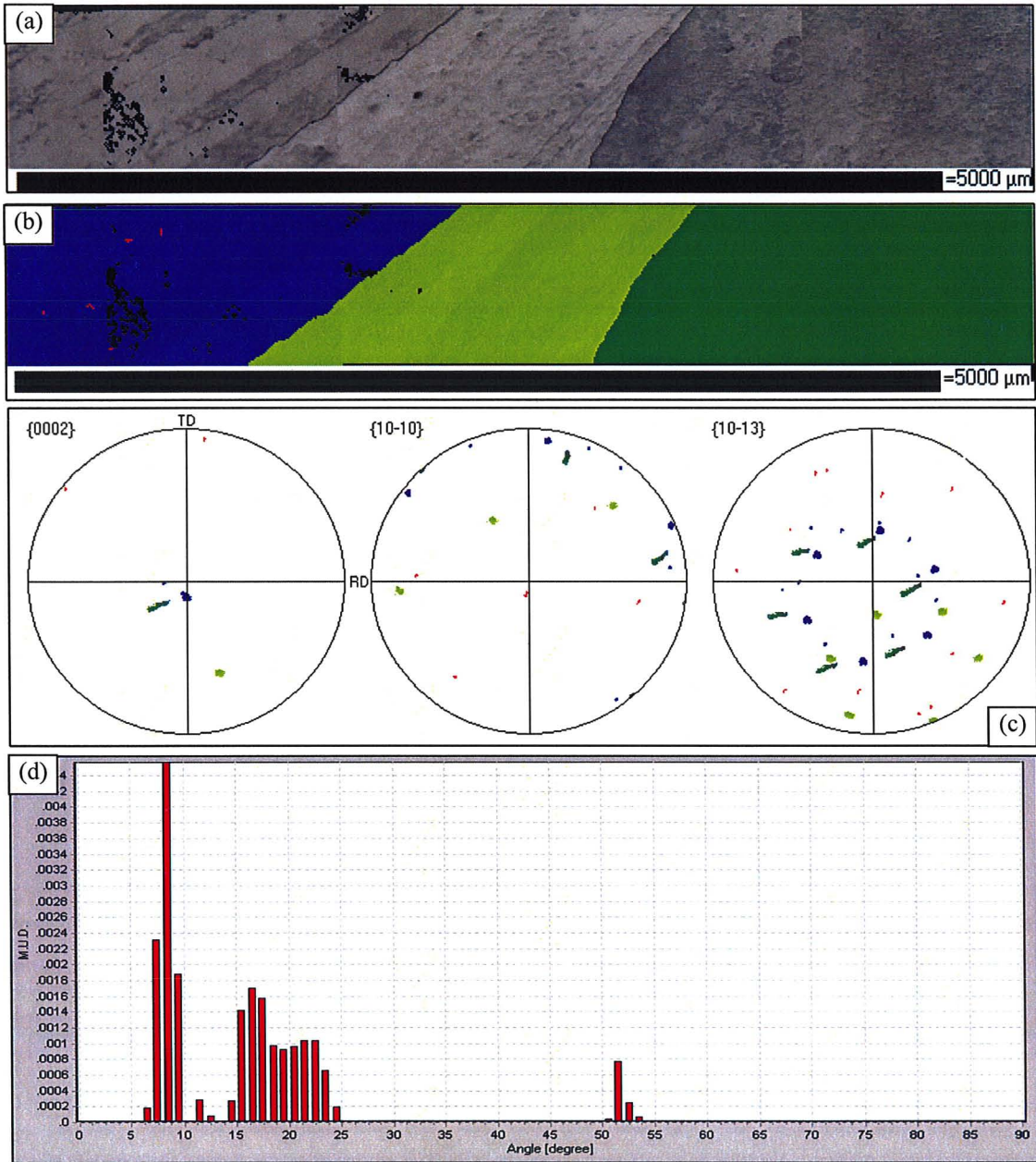


Figure 4-62. (a) Microstructural map (b) Euler orientation colour map (c) pole figures and (d) {0002} pole plot of a coating surface section on a HR steel cooled at 0.1 °C/s

Table 4-7. Area percentage of basal zinc grains inclined for 0-15° relative to the steel sheet (%)

	Cooling rate (°C/s)	
Steel substrate	10	0.1
BR	66.4	65.6
HR	26.6	24.7

4.5. 0.2 wt% Sb Alloy

4.5.1. Coating Surface Microstructure

Dipping experiments on the BR and HR steel substrates were carried out using a molten zinc bath containing 0.2 wt% Sb per Table 3-1. The as-cast coating microstructure on the BR and HR steel substrates at different cooling rates are shown in Figures 4-63(a-f).

As shown in Figures 4-63(a-c), the coating surface of the BR substrate exhibited flowery as well as asymmetrical zinc spangles with a variety of morphologies at 10 °C/s, 1 °C/s and 0.1 °C/s cooling rates, respectively. Accordingly, each zinc spangle is divided into alternate segments with a bright and dark appearance. Shiny, feathery, dimpled, ridged and orthogonal-dendritic morphologies were observed on the coating surface at different cooling conditions and are illustrated in Figures 4-64(a-e). The distribution of the intermetallic phases over the dendritic and non-dendritic surfaces is shown in Figures 4-65(a) and (b). In overall, the majority of the coating surface area was dark with a dominant dull morphology at all cooling rates.

The coating microstructures on the HR substrate were similar to those of the BR substrate (Figures 4-63(d-f)). The coating surface consisted of shiny, feathery, dimpled, ridged and orthogonal-dendritic morphologies at the 10 °C/s cooling rate. However, the coating surface only exhibited the dimpled morphology in the case of the coatings cooled at 1 °C/s and 0.1 °C/s. The coating surface had a significant topography and thus, the

dendritic structure of flowery spangles was not clear, particularly in the case of the slow cooled coating.

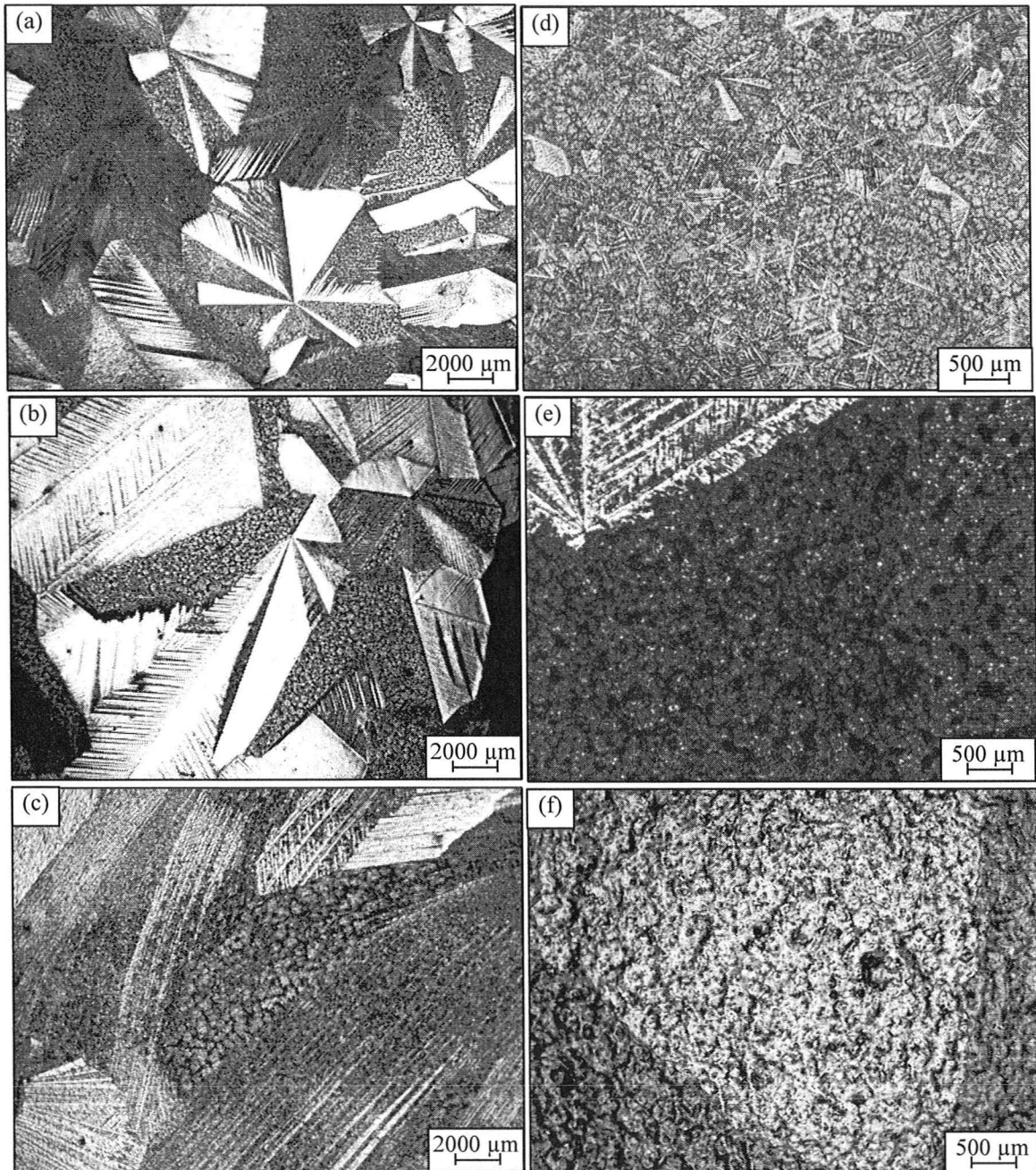


Figure 4-63. Low magnification optical micrographs of the as-cast coating surface containing 0.2 wt% Sb on a BR steel cooled at (a) 10 °C/s (b) 1 °C/s (c) 0.1 °C/s and on a HR steel cooled at (d) 10 °C/s (e) 1 °C/s (f) 0.1 °C/s

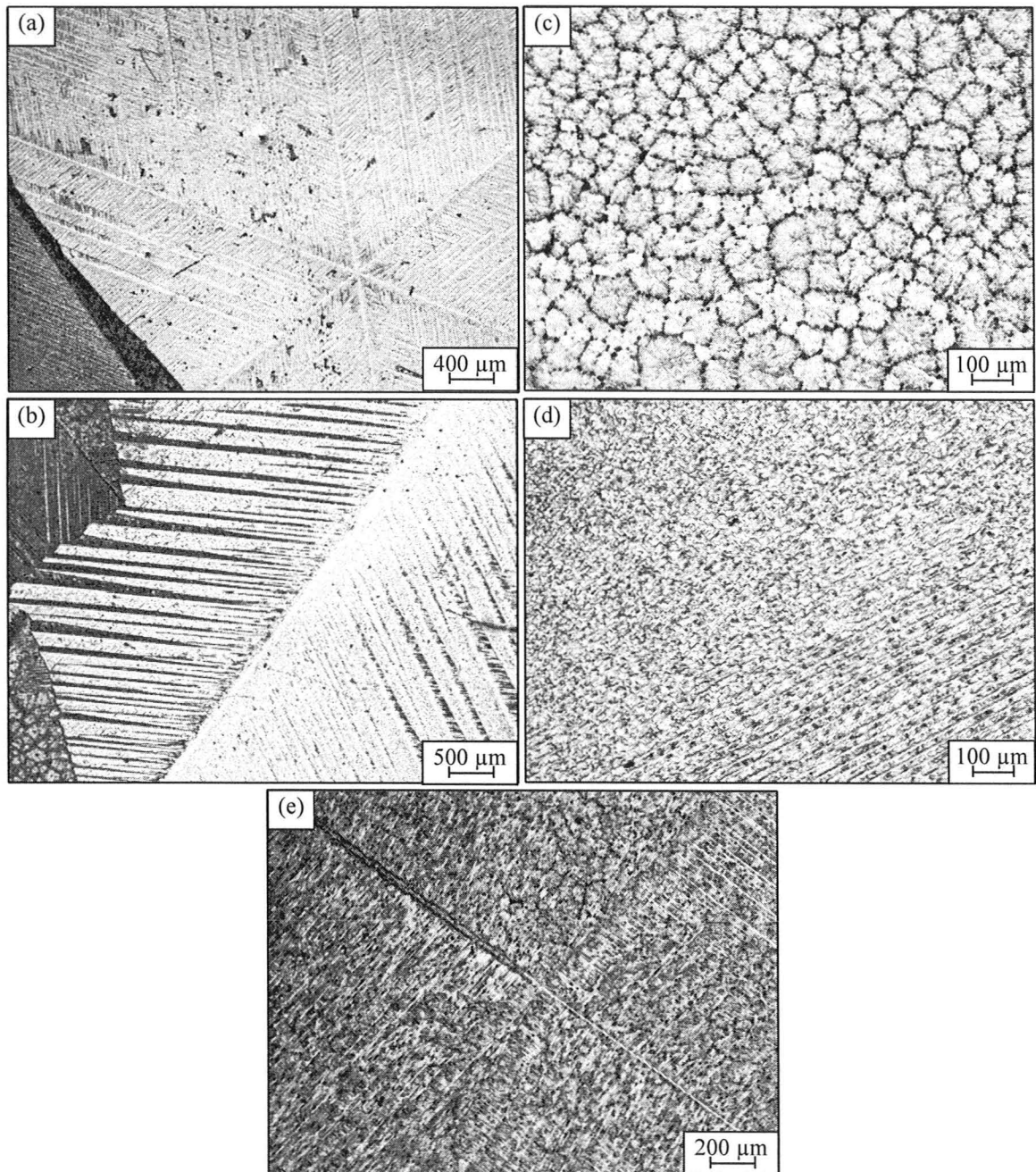


Figure 4-64. Optical micrographs of the (a) shiny (b) feathery (c) dimpled (d) ridged and (e) orthogonal-dendritic morphologies on a coated BR steel cooled at 10 °C/s

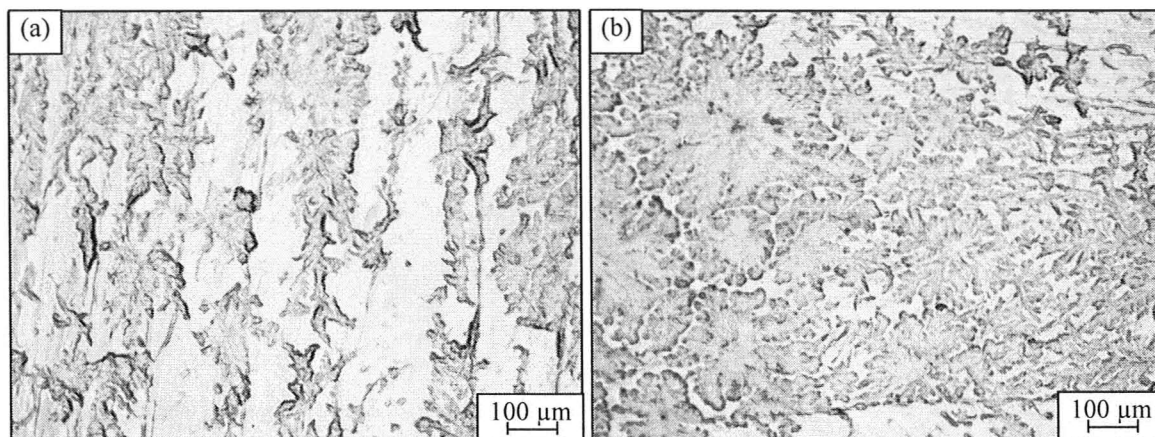


Figure 4-65. Optical micrographs of the (a) dendritic and (b) non-dendritic regions cooled at 10 °C/s on a coated BR steel

Grain size measurements were carried out on both substrates and at all cooling rates. As shown, zinc grains have about the same size on both substrates. Also, on both substrates, grains were smaller at high cooling rates.

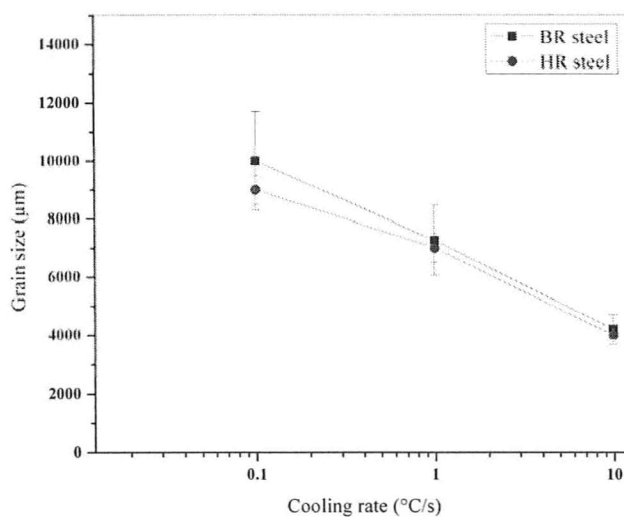


Figure 4-66. Grain size vs. cooling rate for the BR and HR steels

Furthermore, EBSD was performed on coated BR and HR steels for all the cooling conditions and the results were similar to those previously shown in Figures 4-59(a-d), 4-60(a-d), 4-61(a-d) and 4-62(a-d)

4.5.2. Coating Cross-section Microstructure

Similar to coatings containing 0.03 wt% and 0.1 wt% Sb, the coating containing 0.2 wt% Sb exhibited one layer of zinc spangles on BR and HR steel substrates cooled at 10 °C/s which were nucleated on the rough steel surface and grew two dimensionally until they covered the entire surface of the steel substrate. This single layer of zinc spangles continued to thicken along the normal direction of the steel substrate to reach the coating/air interface. Similar results were observed for the coatings cooled at 1 °C/s and 0.1 °C/s.

4.5.3. Coating Intermetallics

On both substrates and at all cooling conditions, all the intermetallic particles observed in coatings containing 0.2 wt% Sb were present in coatings with 0.01 and 0.03 wt% Sb, whose analysis was presented previously. The main intermetallic phase was the Al+Sb compound with the white contrast and irregular shape which covered the coating surface and can be seen along with black etching pits in Figure 4-67.

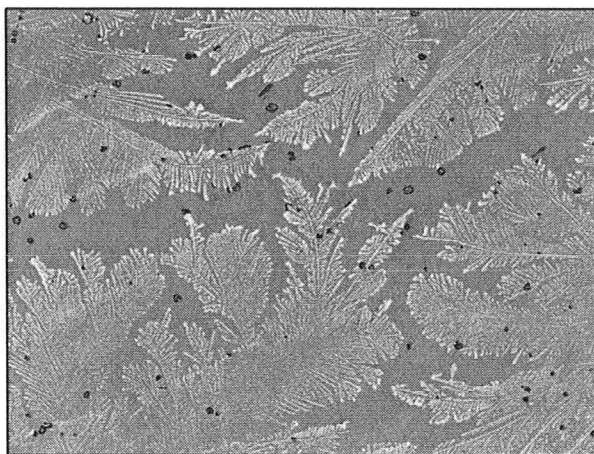


Figure 4-67. AlSb intermetallic particles on coated BR steel cooled at 0.1 °C/s

To confirm the composition of the intermetallic phases present, SAM mapping and point analysis were performed on several areas on the coated BR steel surface cooled at 10 °C/s. It should be mentioned that sputter etching was carried out for 30 s prior to all analysis. Figures 4-68(a-d) and 4-69(a-e) showed the SEM-SEI and the corresponding SAM maps of shiny and dull areas, respectively. As expected, the irregular particles were composed of Sb and Al. On the other hand, the star-like and Chinese-script particles contained Al, Fe and Zn. Quantitative SAM analysis showed the presence of higher concentrations of alloying elements in the dull region as compared to the shiny region as shown in Table 4-8.

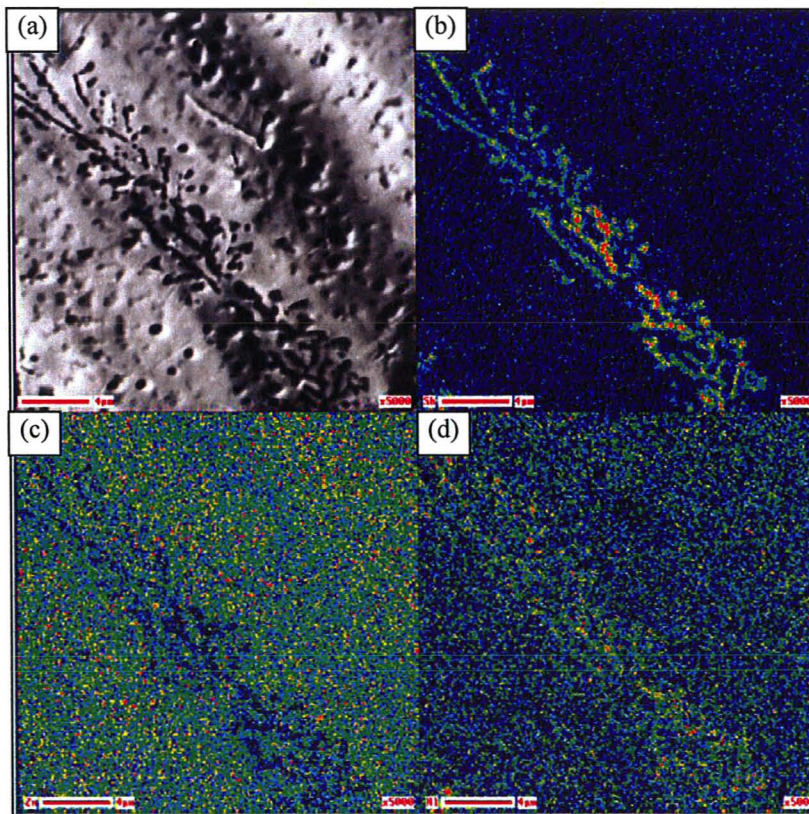


Figure 4-68. (a) SEM-SEI of a shiny region after sputtering on the coated BR steel surface cooled at 10 °C/s (b) Sb (c) Zn and (d) Al SAM maps

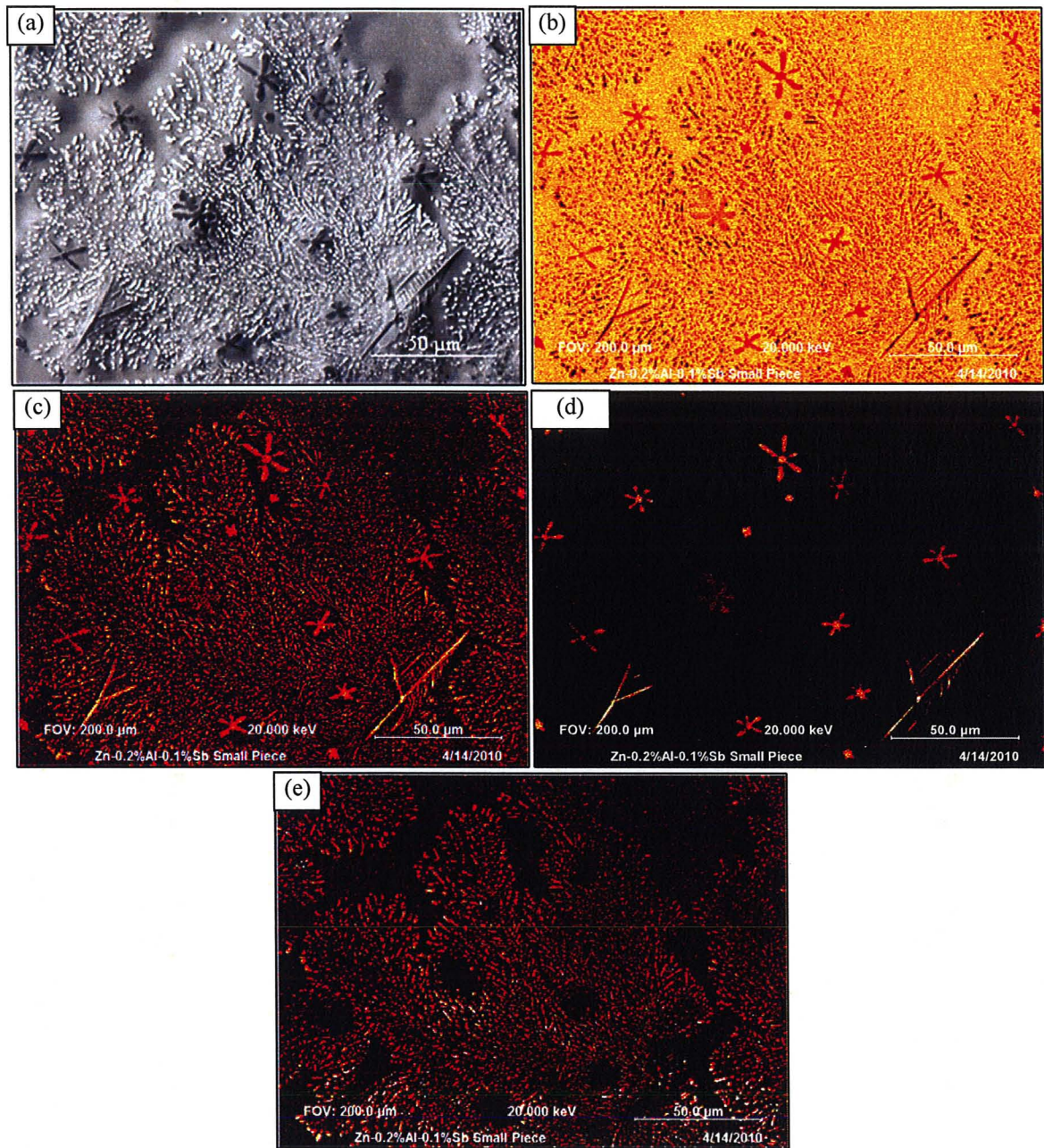


Figure 4-69. (a) SEM-SEIs of a dull region after sputtering on the coated BR steel surface cooled at 10 °C/s (b) Zn (c) Al (d) Fe and (e) Sb SAM maps

Table 4-8. SAM point analysis of the different phases on coated BR steel cooled at 0.1 °C/s (at%)

Region \ Element	Zn	Al	Sb
Dull	8.1	33.7	58.2
shiny	20.8	22.6	56.6

CHAPTER 5. DISCUSSION

5.1. Spangle Formation

It has been reported that the solidification of hot-dip galvanized coatings takes place in a few seconds during which the solid/liquid solidification front is essentially in a non-equilibrium state and is unstable. Nucleation of zinc grains can possibly occur on either the steel/molten zinc interface or the molten zinc/air interface, followed by rapid dendritic growth in sideways directions and subsequent slow thickening of grains along the normal to the steel substrate [Cameron 1965] [Dutta 2007].

Dendritic growth of zinc grains on steel substrates can be mathematically expressed using Equation 5-1 [Nash 1974].

$$V = 0.114 \left(\frac{\alpha_L \Delta S_f L}{\sigma_{SL} C_L} \right) \left(\frac{\Delta T C_L}{L} \right)^{2.65} \quad (\text{Equation 5-1})$$

Clearly, the dendrite growth velocity is proportional to the thermal gradient and inversely proportional to the surface energy at the solid/liquid interface. However, due to the small thermal gradient across the liquid zinc layer [Strutzenberger 1998], the growth of zinc grains is mainly governed by the surface tension at the steel/liquid zinc interface. Thus, the expansion of zinc grains starts on the steel surface two dimensionally and is followed by slow thickening along the direction of heat flow which is normal to the molten zinc/air interface.

For the coatings containing no Sb on the BR steel substrate, it was proposed that nucleation happened at both the $\text{Fe}_2\text{Al}_5\text{Zn}_x$ /liquid zinc and the liquid zinc/air interfaces followed by dendritic growth within the liquid layer. In the case of the HR steel, nucleation mainly occurred on the relatively rough $\text{Fe}_2\text{Al}_5\text{Zn}_x$ surface. Once Sb was added to the zinc bath, nucleation most likely occurred at the rough $\text{Fe}_2\text{Al}_5\text{Zn}_x$ /molten zinc interface on both substrates and subsequent dendritic growth was mainly two dimensional on the $\text{Fe}_2\text{Al}_5\text{Zn}_x$ surface. The same mechanisms were operative for all cooling conditions.

5.2. Spangle Morphology and Appearance

It was mentioned that spangles may exhibit a number of different morphologies. Depending on the crystallographic orientation of the hexagonal zinc crystal and the distribution of the alloying elements and impurities present in the molten zinc bath, shiny, feathery or dull areas can be found on the zinc coatings [Strutzenberger 1998]. Furthermore, coatings may have a bright or dark appearance depending on the coating surface roughness [Fasoyinu 1990].

For the 0.01 wt% Sb addition, shiny, feathery, dimpled, ridged and orthogonal dendritic structures were found on coated BR steel for all cooling conditions (Figures 4-19(a-e)). For the 0.03 wt% Sb alloy, the coatings exhibited a strong basal crystallographic texture on BR steels for all cooling conditions and, therefore, most of the spangles had a shiny, feathery or dimpled morphology where intermetallic particles precipitated (Figures 4-38(a-c)). In addition, coatings containing 0.01 and 0.03 wt% Sb exhibited spangles

which were half dendritic and half non-dendritic with a bright and dark appearance, respectively. The EBSD analysis proved that the entire spangle had a single orientation and, therefore, it is unlikely that the spangle reflectivity was a function of crystallographic orientation [Fasoyinu 1993]. Following the Strutzenberger and Faderl model, it is proposed that the portion of an inclined spangle which first reached the zinc liquid/air interface appeared bright and displayed clear dendritic structure whereas the residual zinc liquid accumulated on top of the remained portion of the spangle and gradually became enriched of solutes and impurities as shown in Figure 5-1(a-d) [Strutzenberger 1998]. Thus, the dendritic structures were covered with a solute rich zinc film which contained a number of intermetallic particles and had a dark appearance [Dutta 2004].

At the 0.1 and 0.2 wt% Sb concentrations, most of the coated BR and HR surface was covered with dimpled spangles which had a dark appearance due to the presence of Sb-containing intermetallic phases (Figures 4-50(a-f) and 4-63(a-f)). On both substrates, ridged and orthogonal dendritic morphologies were rarely detected since the existence of these morphologies is associated with the presence of inclined zinc spangles with respect to the steel plane.

Hence, for both of the steel substrates and all cooling conditions, coatings containing lower amounts of Sb mostly exhibited shiny and feathery morphologies with a relatively bright appearance due to the small amount of Sb containing intermetallics and the resultant smooth spangle surface. On the other hand, at higher Sb levels, greater quantities of Sb containing intermetallic phases were precipitated on the coating surface

which resulted in the formation of topographical dimpled morphologies on the coating surface with a dark appearance.

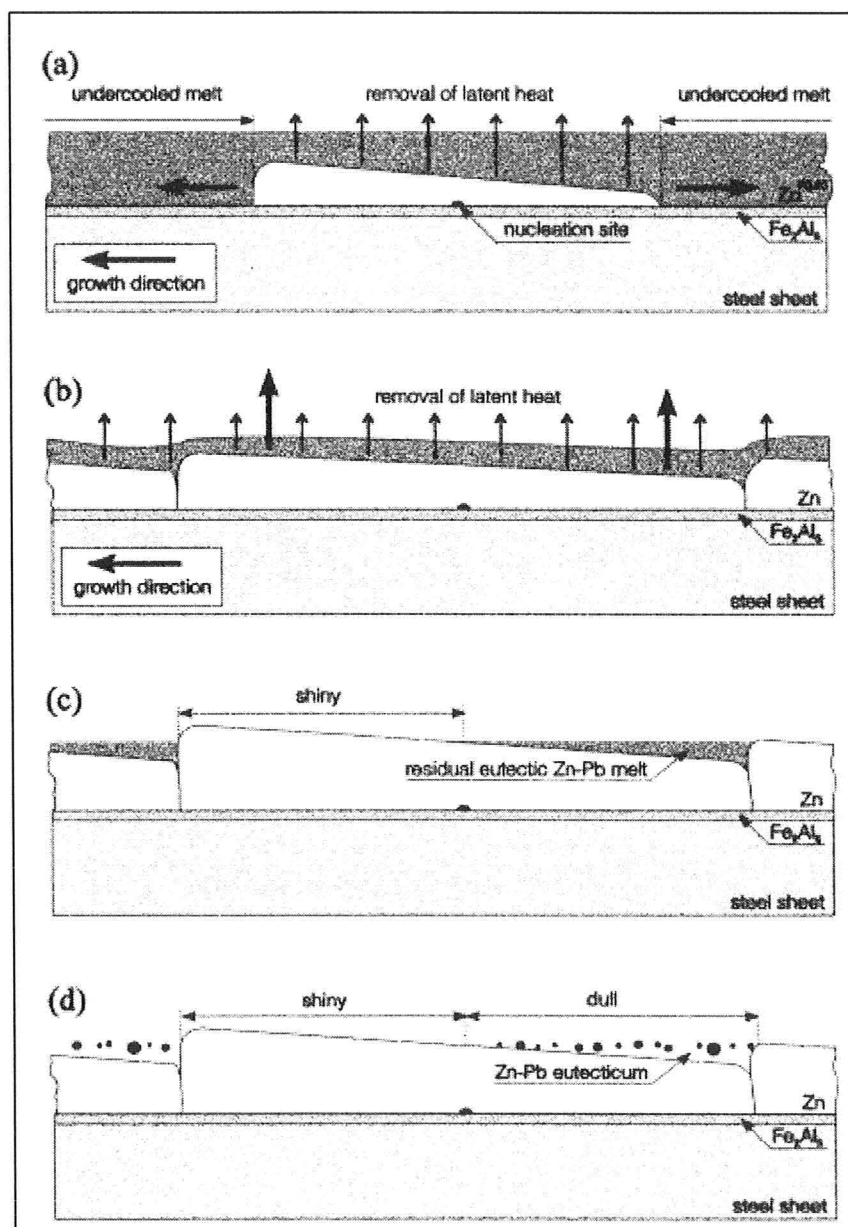


Figure 5-1. Schematic illustration of the solidification sequence for lead containing zinc spangles: (a) rapid lateral expansion, (b) slow thickening process, (c) emergence of shiny sectors, and (d) eutectic Zn-Pb solidification [Strutzenberger 1998]

5.3. Microstructural and Crystallographic Texture Evolution

The driving force for the heterogeneous nucleation of zinc on a steel substrate can be expressed using Equations 5-2 [Porter 1981].

$$\Delta G_r = -\frac{4}{3}\pi r^3 \frac{L_v \Delta T}{T_m} + 4\pi r^2 \sigma_{sl} \quad (\text{Equation 5-2})$$

According to Equations 5-1 and 5-2, both the driving force for heterogeneous nucleation of zinc grains and the dendrite growth velocity are functions of the surface energy at the steel/liquid zinc interface. Thus, nucleation and growth of the {0002} close-packed basal crystallographic planes of a hexagonal zinc crystal is favoured in a direction which is parallel to the steel/liquid interface due to the minimum surface energy at this interface. As a result, solidified coatings are expected to exhibit a strong basal crystallographic texture [Jordanovac 2004]. In addition, the thermal gradient across the liquid zinc layer can affect the crystallographic texture of the zinc coating such that the {0002} basal planes are forced to grow normal to the liquid zinc/air interface, particularly at high cooling rates [Chalmers 1964].

For the 0 wt% Sb addition to the liquid zinc bath, zinc grains exhibited dendritic structures and a strong basal crystallographic texture on the BR substrate whereas zinc grains exhibited non-dendritic structures and a much weaker basal crystallographic texture on the HR substrate (Figures 4-1(a-f), 4-13(a-d), 4-14(a-d), 4-15(a-d) and 4-16(a-d)). These observations were attributed to the difference in steel surface condition (Figures 5-2(a) and (b)). In the case of the BR substrate, the {0002} basal planes were

formed on the $\text{Fe}_2\text{Al}_5\text{Zn}_x$ crystals with small topography and as a result, dendritic structures were detected on the coating surface. However, in the case of the HR steel substrate, the $\{0002\}$ basal planes were formed on the $\text{Fe}_2\text{Al}_5\text{Zn}_x$ crystals with greater topographic variation and, therefore, the final zinc grains exhibited limited dendritic structures and non-dominant basal crystallographic texture. Thus, regardless of the steel substrate and cooling conditions, coatings containing 0 wt% Sb were composed of zinc grains with dendritic structures and the $\{0002\}$ basal planes formed parallel to the steel/liquid zinc interface.

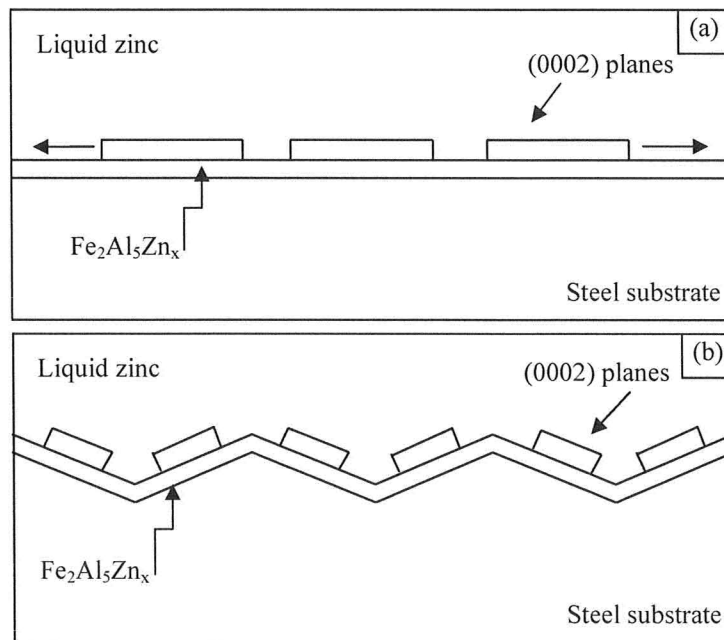


Figure 5-2. Schematic of the nucleation and growth conditions on (a) BR and (b) HR steel substrate at 0 wt% Sb

In coatings containing 0.01 and 0.03 wt% Sb, dendritic spangles with pronounced basal crystallographic orientation were observed on coated BR steels at all cooling conditions (Figures 4-17(a-c), 4-33(a-d), 4-34(a-d), 4-38(a-c), 46(a-d) and 4-47(a-d)). Also, the coated HR steel substrate cooled at 10 °C/s exhibited some dendritic structure and a preferred basal crystallographic texture (Figures 4-18(d), 4-35(a-d), 4-38(d) and 4-48(a-d)) while clear internal dendritic structures and pronounced preferred basal crystallographic texture were not observed on coated HR steels cooled at 1 °C/s and 0.1 °C/s (Figures 4-17(e-f), 4-36(a-d), 4-38(e-f) and 4-49(a-d)). On both substrates and at all cooling rates, the zinc spangles exhibited internal dendritic structures and clear basal crystallographic texture for the 0.1 and 0.2 wt% Sb additions to the zinc bath (Figures 4-50(a-f), 4-59(a-d), 4-60(a-d), 4-61(a-d), 4-62(a-d) and 4-63(a-f)).

Based on the thermodynamic calculations of Liu and Tang, the surface energy and solute segregation of the zinc melt as a function of the Sb addition have been assessed [Liu 2007]. According to Figure 5-3, the presence of small amounts of Sb results in considerable solute segregation on the melt free surface and in turn, decreases the surface energy of the liquid zinc. At high Sb concentrations, the cooling rate at the liquid zinc/air interface promotes the crystallographic orientation for a given surface tension value. Thus, regardless of the steel substrate, coatings containing 0.1 wt% and 0.2 wt% Sb exhibited dendritic structures and basal crystallographic texture.

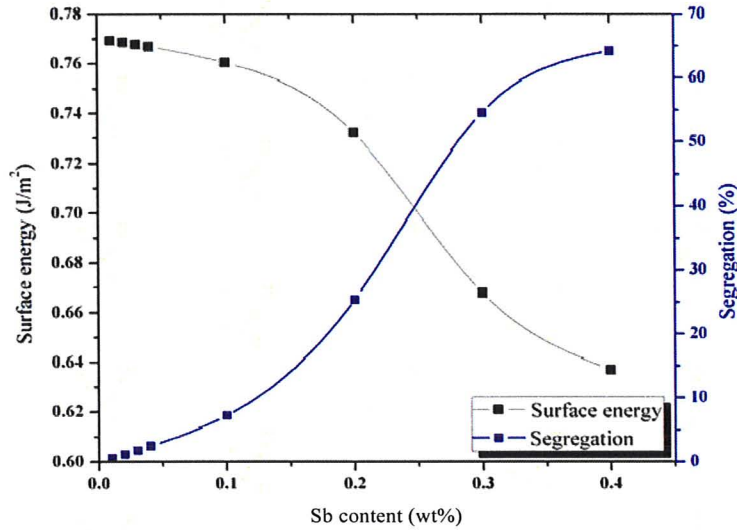


Figure 5-3. Melt surface energy and solute segregation vs. Sb content

Using equation 5-3, the strength of the basal crystallographic texture was defined as the area of zinc grains with an inclination angle of 0-15° with respect to the steel sheet divided by the total area of the coating.

$$f(\{0002\}) = \frac{\sum_0^{15} (\{0002\})}{\sum_0^{90} (\{0002\})} \times 100 \quad (\text{Equation 5-3})$$

Figures 5-4(a) and (b) show the strength of basal crystallographic texture ($f\{0002\}$) as a function of steel surface roughness and melt surface energy for coatings cooled at 10 °C/s and 0.1 °C/s, respectively. As shown, for both steel substrates and cooling rates, coatings exhibited strong basal crystallographic texture at low melt surface energy which corresponds to a high alloy Sb content. In addition, keeping the melt surface energy constant, the low Ra coated BR steel contained a higher percentage of basal zinc grains as compared to the coated HR steel at each cooling rate.

Figures 5-5(a) and (b) show $f(\{0002\})$ as a function of cooling rate and melt surface energy for the BR and HR steels, respectively. As can be seen, the basal crystallographic texture was promoted at high Sb levels and high cooling rates on both substrates. In addition, $f(\{0002\})$ was almost independent of the coating cooling rate on BR steel. On the other hand, at the same surface energy, grains exhibited strong basal crystallographic texture at high cooling rate on HR steel. It should be noted that the graphs were plotted in two different scales for the $f(\{0002\})$.

In summary, at high Sb levels in the liquid bath, the cooling rate at the liquid zinc/air interface defeated the crystallographic-based preferences for nucleation and growth of zinc grains and forced the $\{0002\}$ basal planes to grow normal to the liquid zinc/air interface. Consequently, addition of Sb to the zinc bath resulted in the formation of strong preferred basal crystallographic texture on both substrates and at all cooling conditions and, thus, internal dendritic structures of spangles could be observed.

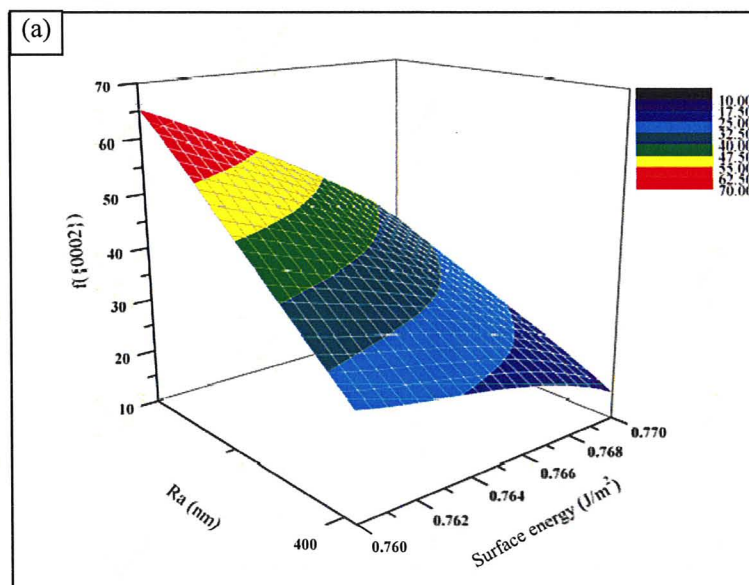


Figure 5-4(a). $f(\{0002\})$ vs. steel surface roughness and melt surface energy for 10 °C/s

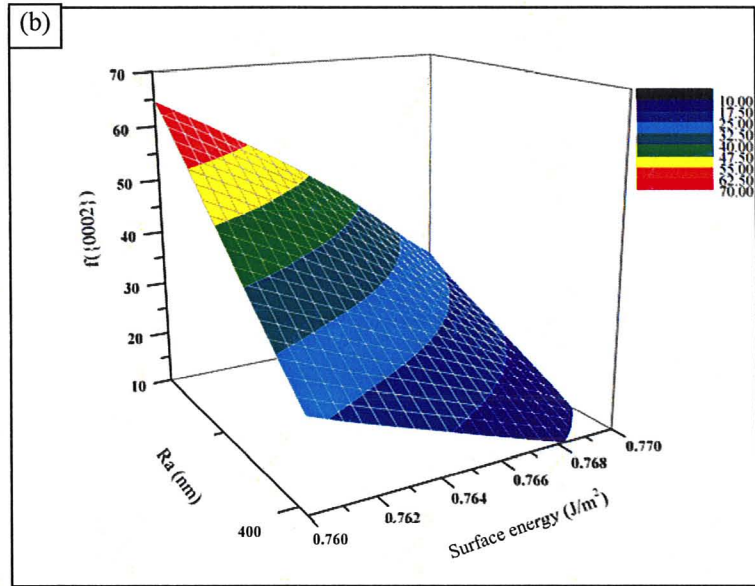


Figure 5-4 (b). (Cont'd) $f_{(0002)}$ vs. steel surface roughness and melt surface energy for 0.1 °C/s

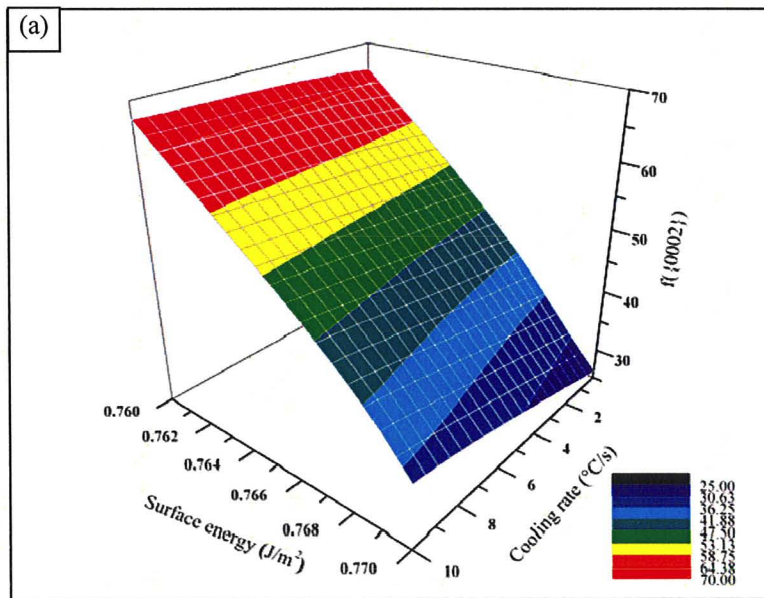


Figure 5-5(a). $f_{(0002)}$ vs. cooling rate and surface energy for BR Steel

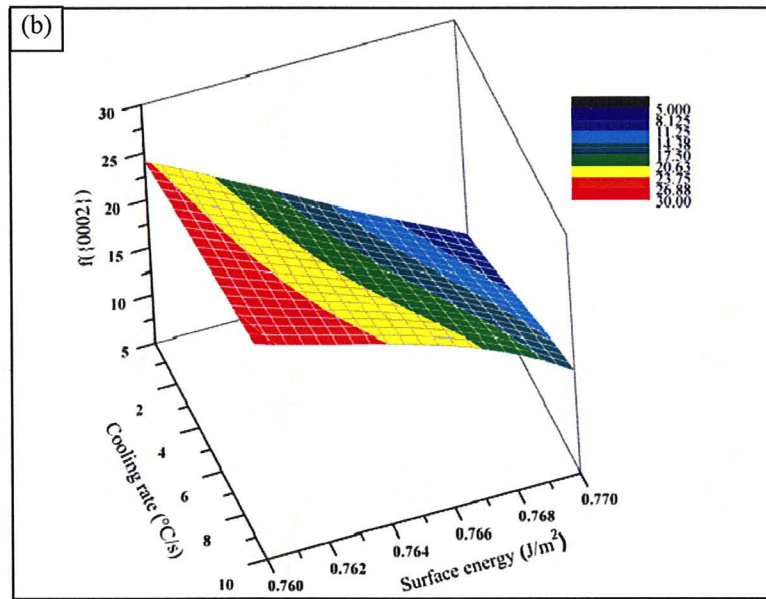


Figure 5-5(b). (Cont'd) $f(\{0002\})$ vs. cooling rate and surface energy for HR steel

5.4. Zinc Grain Size

As discussed previously, small Sb additions can result in considerable solute segregation and subsequent reduction of the melt surface tension. Assuming constant wetting angle, a smaller surface energy results in lower activation energy for heterogeneous nucleation and, therefore, the nucleation rate is decreased even though the number of available nucleation sites remains unchanged (Equations 5-4 (a) and (b)). Hence, the previously mentioned poisoning effect on the reduction of the number of available nucleation sites is considered to be invalid.

$$\Delta G_{het}^* = \left(\frac{16\pi\sigma_{SL}^3 T_m^2}{3L_V^2} \right) \left(\frac{1}{\Delta T^2} \right) \frac{(2 + \cos\theta)(1 - \cos\theta)^2}{4} \quad (\text{Equation 5-4 (a)})$$

$$n^* = n_1 \exp\left(-\frac{\Delta G_{het}^*}{kT}\right) \quad (\text{Equation 5-4 (b)})$$

In addition, a smaller surface energy at the solid/liquid interface decreases the dendrite tip radius and increases the dendrite growth rate (Equation 5-1). Hence, the resultant microstructure exhibits larger spangles at higher additions of Sb (i. e. Lower surface energy) [Fasoyinu 1990] [Liu 2004].

Grain size measurements were carried out on both substrates at all cooling conditions and the results are shown in Figures 5-6(a-c) and 5-7(a) and (b). Keeping all parameters constant, it was found that an increase in Sb content of the molten zinc bath resulted in the formation of larger zinc spangles, as expected. Furthermore, at each Sb addition, the coated HR steels exhibited slightly smaller grains as compared to the coated BR steels for the same cooling rate, particularly at high Sb contents (Figures 5-6(a-c)). It should be noted that the graphs were plotted in two different scales for the zinc grain size. Sere et al. reported that the steel surface condition can affect the zinc grain size. The rougher HR steel surface increased the driving force for the crystals nucleation and, therefore, the resultant coatings contained smaller zinc grains [Sere 1997]. Also, it has been mentioned that higher cooling rate during coating solidification results in higher nucleation rate and, therefore, smaller grain size as shown in Figures 5-7(a) and (b) [Cameron 1967] [Gutenberg 1990]. However, at high Sb levels in the zinc bath, zinc grain size was essentially independent of the cooling rate as shown in Figures 5-7(a) and (b).

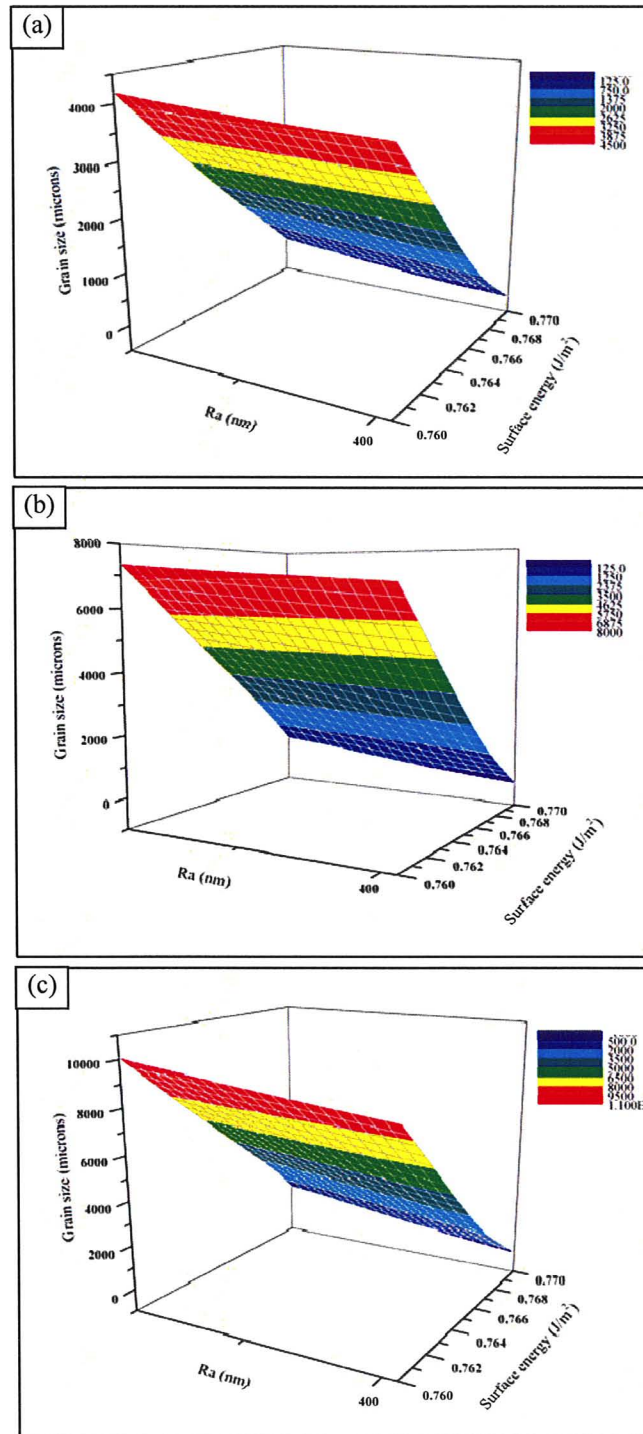


Figure 5-6. Zinc grain size vs. steel surface roughness and melt surface energy for coatings cooled at (a) 10 (b) 1 and (c) 0.1 °C/s

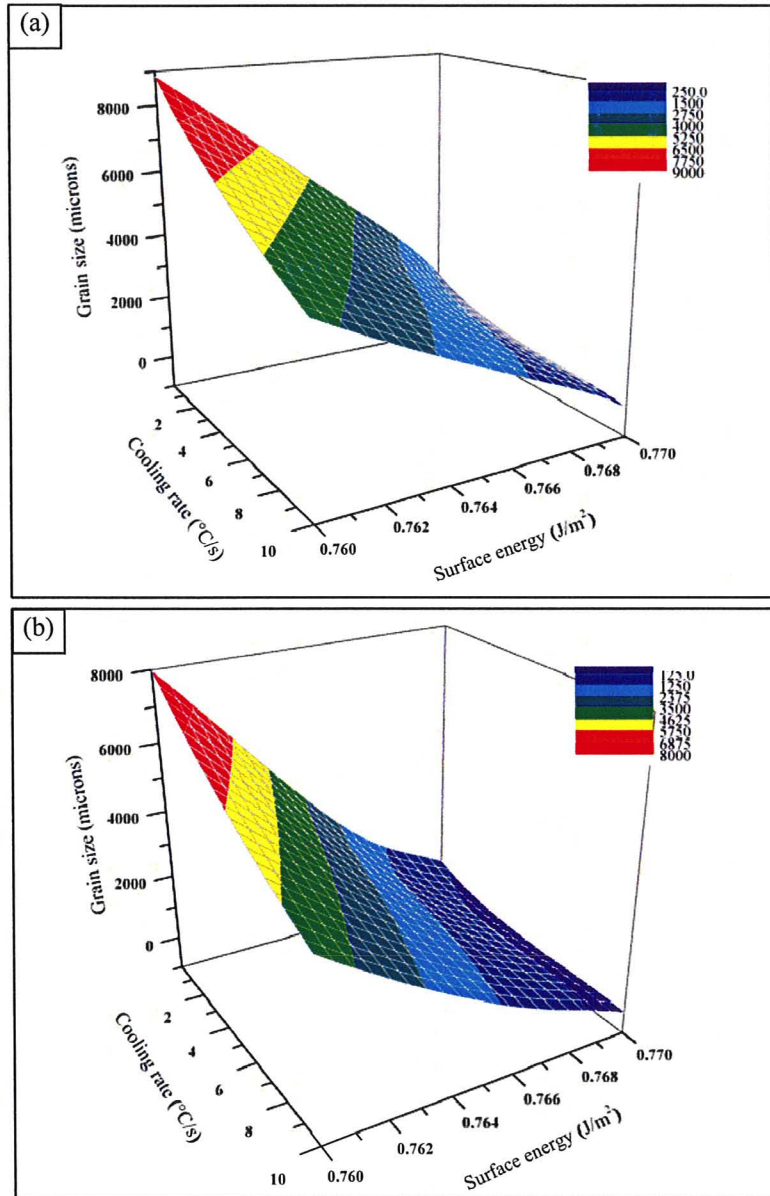


Figure 5-7. Zinc grain size vs. cooling rate and melt surface energy for coatings on (a) BR and (b) HR steels

5.5. Coating Intermetallic Phases

Al, Fe and Sb alloying additions were present in the liquid zinc baths (Table 3-3). In addition, small quantities of impurities such as Cr, Ni, Sn and Pb were detected in the solidified coatings (Tables 4-1, 4-3 and 4-5). Given a constant Al and Fe concentration, the Zn-Al-Fe-Sb phase diagram was assessed using FactSage 6.1 software (Figure 5-8). As can be seen, the AlSb compound was the main intermetallic phase which was formed during coating solidification over the range of 0.01-0.2 wt% Sb concentration. As the amount of Sb was increased in the liquid zinc bath, higher amounts of the AlSb phase were formed on the coating surface while the Al concentration was kept constant. It should be noted that this phase was found within the coating thickness as well as on the coating surface.

Based on the McDermid et al. solubility curves [McDermid 2007], the solubility of Al and Fe was reduced as the temperature of the liquid zinc was decreased and, therefore, the small round, star-like and Chinese-script particles were formed in coatings at all the explored conditions. According to the Zn-Al-Fe-Sb phase diagram, $\text{Al}_{13}\text{Fe}_4$ is the only equilibrium Al-Fe intermetallic phase in the experimental temperature range. Based on the quantitative SAM results shown in Tables 4-1 and 4-3, it is proposed that this compound corresponds to the observed dark grey Chinese-script particles. The other intermetallic particles could not be identified. In addition, the bath impurities rejected from the solid/liquid interface during coating solidification and segregated at the perimeter of the aforementioned intermetallic particles.

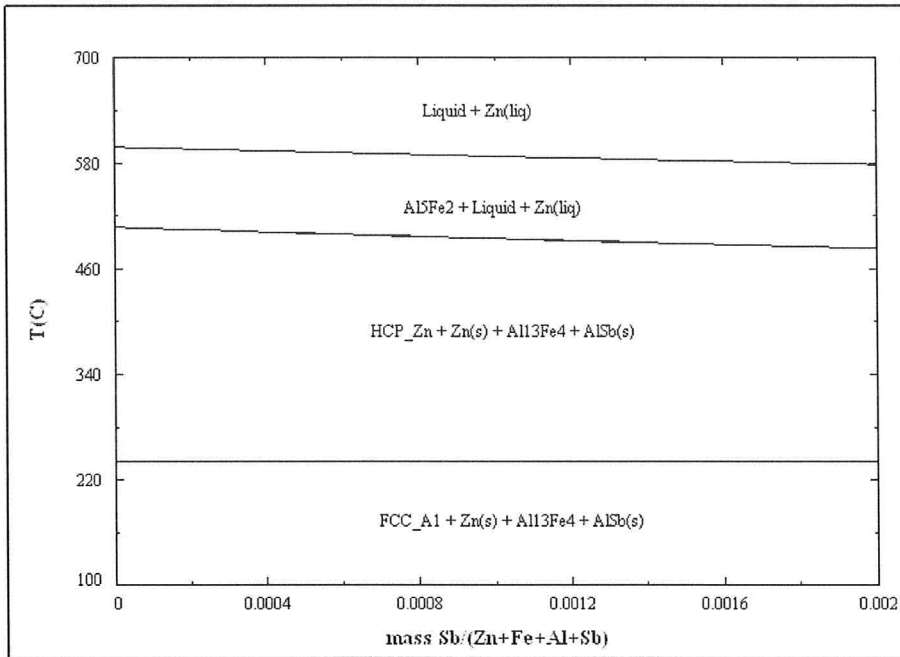


Figure 5-8. Zn-Al-Fe-Sb phase diagram

CHAPTER 6. CONCLUSIONS

1. Addition of small amounts of Sb to the galvanizing zinc bath altered the coating appearance, crystal morphology and crystallographic texture. Sb additions produced dark coatings which consisted of large spangles with a dull morphology and enhanced basal crystallographic texture. The presence of 0.01-0.2 wt% Sb in the zinc bath increased the coating grain size on the BR and HR substrates at 10 °C/s, 1 °C/s and 0.1 °C/s cooling rates. However, at high Sb concentrations, the zinc grain size was essentially independent of the initial steel surface roughness. Furthermore, on both substrates and at all cooling rates, the basal crystallographic texture was promoted with Sb additions.
2. Steel surface roughness affected the coating appearance, crystal morphology and crystallographic texture. Coatings exhibited a brighter appearance, larger grain size and stronger basal crystallographic texture on the smooth BR substrate as compared to the coatings on the rougher HR substrate. Regardless of the zinc bath composition, the coated BR steels exhibited basal crystallographic texture at all cooling rates. On the other hand, at 0 wt% Sb, the coated HR steels exhibited a weak basal crystallographic texture at all cooling rates. At 0.01-0.2 wt% Sb content, a strong basal crystallographic texture was detected on the coated HR steels, particularly at high cooling rate.
3. The coating cooling rate during solidification controlled the zinc grain size such that smaller zinc grains were formed on coatings cooled at the high cooling

rate. However, at high Sb concentrations, the zinc grains size was largely independent of the coating cooling rate.

4. AlSb was the main intermetallic phase which was precipitated on the coating surface as well as within the coating thickness. Keeping the bath Al content constant and increasing the Sb concentration in the liquid bath, more AlSb phase was detected on the coating surface. Furthermore, three types of Fe-Al intermetallic precipitates were formed on the coating surface. These phases were formed in round, star-like and Chinese script morphologies. The dark grey Chinese-script phase was most likely $Al_{13}Fe_4$ compound.
5. Zinc spangles with inclined basal crystallographic planes exhibited a dark appearance and dull morphology. Also, the presence of intermetallic phases on the coating surface resulted in the formation of dimpled morphology with a dark appearance on the coating surface.

REFERENCES

- Asgari H., Toroghinejad M. R., Golozar M. A., “*On Texture, Corrosion Resistance and Morphology of Hot-dip Galvanized Zinc Coatings*”, Applied Surface Science, Vol. 253, (2007), 6769-6777.
- ASM Handbook, Metallography and Microstructures, “*Metallography and Microstructures of Zinc and its Alloys*”, Vol. 9, 933-941.
- ASTM Standards, A 90/A 90M, “*Standard Test Method for Weight [mass] of Coating on Iron and Steel Articles with Zinc or Zinc-alloy Coatings*”, (2001).
- Biber H. E., “*Scanning Auger Microprobe Study of Hot-dipped Regular-spangle Galvanized Steel*”, Metallurgical Transactions A, Vol. 19, (1988), 1603-1608.
- Cameron D. I., Harvey G. J., “*Solidification and Spangle of Galvanized Coatings*”, Proceedings of 8th International Conference on Hot Dip Galvanizing, (1967), 86-97.
- Cameron D. I., Harvey G. H., Ormay M. K., “*The Spangle of Galvanized Iron*”, Journal of the Australian Institute of Metals, Vol. 10, No. 3, (1965), 255-264.
- Chalmers B., “*Principles of Solidification*”, J. Wiley and Sons, Inc. New York, (1964), p134.
- Chang S., Shin J. C., “*The Effect of Antimony Additions on Hot-dip Galvanized Coatings*”, Corrosion Science, Vol. 36, No. 8, (1994), 1425-1436.

Chang S., Shin J. C., “*Effect of the Zinc Bath Composition on Hot-dip Galvanized Steel Sheet*”, Galvatech’95 Conference Proceedings, (1995), 783-786.

Chattopadhyay A., Subramanya Sarma V., Murty B. S., Haldara A., Bhattacharjee D., “*Studies on Hot-rolled Galvanized Steel Sheets: Segregation of Alloying Elements at the Surface*”, Scripta Materialia, Vol. 59, (2008), 522-525.

Chidambaram P.R., Rangarajan V., Ooij W. J., “*Characterization of High Temperature Hot-dip Galvanized Coatings*”, Surface and Coatings Technology, Vol. 46, (1991), 245-253.

Culcasia J. D., Elsnerb C. I., Di Sarli A. R., “*Effect of Zinc Crystals Size on Galvanized Steel Deformation and Electrochemical Behavior*”, Materials Research, Vol. 12, No. 3, (2009), 273-279.

Culcasi J. D., Sere P. R., Elsner C. I., Di Sarli A. R., “*Control of the Growth of Zinc-iron Phases in the Hot-dip Galvanizing Process*”, Surface and Coatings Technology, Vol. 122, (1999), 21-23.

Dionne S., “*The Characterization of Continuous Hot-dip Galvanized and Galvannealed Steels*”, Journal of the Minerals, Metals and Materials Society, (2006), 32-40.

Dutta M., Ganguly S., Jha G., Singh A. K., Chakrabarti S., Rajesh N., “*Improvement in Surface Brightness and Prediction of Spangle Formation Time in a Continuous Galvanizing Line Through Heat Balance*”, ISIJ International, Vol. 45, No. 3, (2005), 366-372.

Dutta M., Mukhopadhyay A., Chakrabarti S., “*Effect of Galvanizing Parameters on Spangle Size Investigated by Data Mining Technique*”, ISIJ International, Vol. 44, No. 1, (2004), 129–138.

Faderl J., Maschek M., Strutzenberger J., “*Spangle Size and Aluminum Pick up for Hot-dip Zinc Coatings*”, Galvatech’95 Conference Proceedings, (1995), 675-685.

Fasoyinu F. A., “*The Solidification of Hot-dip Galvanized Coatings on Steel*”, Ph.D. dissertation, the University of British Columbia, Vancouver, BC, Canada, (1989).

Fasoyinu F. A., Weinberg F., “*Spangle Formation in Galvanized Sheet Steel Coatings*”, Metallurgical Transactions B, Vol. 21, (1990), 549-558.

Fasoyinu F. A., Weinberg F., “*The Surface Topography of Sheet Steel Galvanized Coatings*”, Canadian Metallurgical Quarterly, Vol. 32, No. 2, (1993), 185-192.

Franks L. F., Conduci B. L., Smith D. E., Proc. Galv. Comm., Zinc Inst. Inc., Vol. 68, (1976), 16-21.

Furdanowicz V., Ramadeva Shastry C., “*Distribution of Aluminum in Hot-Dip Galvanized Coatings*”, Metallurgical and Materials Transactions A, Vol. 30, (1999), 3031-3044.

Garza M., Guerrero M. P., Zambrano P., Colás R., Houbaert Y., “*Surface Characterization of Hot and Cold Rolled Low Carbon Steel Strips After Galvanizing and Galvannealing*”, Materials and Manufacturing processes, Vol. 22, (2007), 323-327.

Gutenberg R., Lait J., Weinberg F., “*Changing Al and Pb Bath Concentrations in Galvanized Sheet Steel*”, Canadian Metallurgical Quarterly, Vol. 29, No. 4, (1990), 307-312.

Hanna F., Nassif N., “*Factors Affecting the Quality of Hot-dip Galvanized Steel Sheets*”, Surface Technology, Vol. 21, (1984), 27-37.

Helwig L. E., Proc. of Galv. Comm., Zinc Inst. Inc., Vol. 73, (1981), 22-51.

Iordanova I., “*Analysis of Microstructure and its Anisotropy in Hot-dip Galvanized Coatings Applied on Low Carbon Cold Rolled Steel*”, Galvanotechnic, (2004), 1379-1389.

Jaffrey D., Browne J. D., Howard T. J., “*The Cracking of Zinc Spangles on Hot-dipped Galvanized Steel*”, Metallurgical Transactions B, Vol. 11, (1980), 631-635.

Jin-tang L., Xin-hua W., Chun-shan C., Gang K., Jin-hong C., Qiao-yu X., “*Crystallographic Research of Spangle on Hot-dip Galvanized Steel Sheets*”, Transactions of Nonferrous Metals Society of China, Vol. 17, (2007), 351-356.

Jordan C. E., Goggins K. M., Bencotter A. O., Marder A. R., “*Metallographic Preparation Technique for Hot-dip Galvanized and Galvannealed Coatings on Steel*”, Materials Characterization, Vol. 31, (1993), 107-114.

Kabeya M., Shindo Y., Journal of the Iron and Steel Institute of Japan, Vol. 3, (1990), 655.

Kilbane F. M., Proc. Galv. Comm., Zinc. Inst. Inc., Vol. 74, (1982), 1-45.

Kilpatrick J.R., “*A New Etching Technique for Galvanneal and Hot-dipped Galvanized Coatings*”, Practical Metallography, Vol. 28, (1991), 649.

Kim Y., Patil R., Proceedings of 1st International Conference on Coated Steel Sheet, (1985).

Konecny R. G., “*Effects of the Minor Elements in a Galvanizing Bath*”, Wire Journal, Vol. 5, (1972), 40-44.

Leidheiser Jr., Kim D. K., “*Crystallographic Factors Affecting the Adherence of Paint to Deformed Galvanized Steel*”, Journal of the Minerals, Metals and Materials Society, (1976), 19-25.

Leory V., Materials Science and Engineering, Vol. 42, (1980), 289-307.

Leory V., Schmitz B., “*Surface Chemistry of Zn and Zn/Al Hot-dipped Steels: Influence of Some Processing Parameters*”, Scandinavian Journal of Metallurgy, Vol. 17, (1988), 17-23.

Lindenmeyer C. S., Ph.D. Thesis, Harvard University, (1959).

Liu Y. H., Tang N. Y., “*Thermodynamic Explanation of Spangle Formation*”, Galvatech'04 Conference Proceedings, (2004), 941-950.

Mackowaik J., Short N. R., “*Metallurgy of Galvanized Coatings*”, International Metals Reviews, No. 1, (1979), 1-19.

Marder A. R., “*The Metallurgy of Zinc-coated Steel*”, Progress in Materials Science, Vol. 45, (2000), 191-271.

McDermid J. R., Hrymak A. N., Fourmentin R., Salari S. and Goodwin F. E., “*Effect of Steel Substrate Roughness on GA and GI Coating Roughness During the Gas-jet Wiping Process*”, AISTech 2009 Proceedings – Vol. 2, (2009)

McDermid J. R., Dewey C. E., “*Optimizing the GA to GI Transition at ProTec CGL#1*”, Proceedings of the 92nd Galvanizer’s Association Meeting, (2000).

McDermid J. R., Kaye M. H., Thompson W. T., “*Fe Solubility in the Zn-Rich Corner of the Zn-Al-Fe System for Use in Continuous Galvanizing and Galvannealing*”, Metallurgical and Material Transactions B, Vol. 38, (2007), 215-230.

Nash G. E. and Glicksman M. E., *Acta Metall.*, Vol. 22, (1974), 1291.

Payling R., Mercer P. D., Applied Surface Science, Vols. 22-23, (1985), 224-235.

Pistofidis N., Vourlias G., Konidaris S., Pavlidou E., Stergiou A., Stergioudis G., “*The Effect of Bismuth on the Structure of Zinc Hot-dip Galvanized Coatings*”, Materials Letters, Vol. 61, (2007), 994-997.

Porter D. A., K. E. Sterling, “*Phase Transformation in Metals and Alloys*”, Van Nostrand Reinhold, UK, (1981).

Poulon-Quintin A., Chirazi A., Reumont G., Foct J., Goodwin F., “*Solidification Morphology of Hot-dipped Galvanized Steel Coating*”, Galvatech'04 Conference Proceeding, (2004), 691-702.

Rodnyansky A., Warburton Y. J., Hanke L. D., “*Segregation in Hot-dipped Galvanized Steel*”, Surface and Interface Analysis, Vol. 29, (2000), 215-220.

Scully J. C., “*The Fundamentals of Corrosion*”, Pergamon Press Oxford, New York, (1990).

Semoroz A., “*Experimental Study and Modeling of Nucleation and Growth During Solidification of Al and Zn Coatings*”, Ph.D. dissertation, Ecole Polytechnique Federale de Lausanne, Switzerland, 2001.

Semoroz A., Durandet Y., Rappaz M., “*EBSD Characterization of Dendrite Growth Directions, Texture and Misorientations in Hot-dipped Zn-Al-Si*”, Acta Materialia, Vol. 49, (2001), 529-541.

Semoroz A., Henry S., Rappaz M., “*Application of the Phase-field Method to the Solidification of Hot-dipped Galvanized Coatings*”, Metallurgical and Materials Transactions A, Vol. 31, (2000), 487-495.

1. Semoroz A., Strezov L., Rappaz M., “*Orientation Domains and Texture in Hot-dipped Galvanized Coatings*”, Metallurgical and Materials Transactions A., Vol. 33, (2002), 2695-2701.

2. Semoroz A., Strezov L., Rappaz M., “*Numerical Simulation of Zn Coating Solidification*”, Metallurgical and Materials Transactions A, Vol. 33, (2002), 2685-2693.

Sere P. R., Culcasi J. D., Elsner C. I., Di Sarli A. R., “*Factors Affecting the Hot-dip Zinc Coatings Structure*”, Revista de Metalurgia, Vol. 33, (1997), 376-381.

Sere P. R., Culcasi J. D., Elsner C. I., Di Sarli A. R., “*Relationship Between Texture and Corrosion Resistance in Hot-dip Galvanized Steel Sheets*”, Surface and Coating Technology, Vol. 122, (1999), 143-149.

Shah S. R., Dilewijns J. A., Jones R. D., “*The Structure and Deformation Behaviour of Zinc-rich Coatings on Steel Sheet*”, ASM International, Vol. 5, (1996), 601-608.

Shindo Y., Timura T., Kabeya M., Nagahisa N., Asano H., Kitazawa Y., UK Patent, GB 2080340, (1982).

Singh A. K., Jha G., Chakrabarti S., “*Spangle Formation on Hot-dip Galvanized Steel Sheet and its Effects on Corrosion-resistant Properties*”, Corrosion Engineering Section, Vol. 50, No. 2, (2003), 189-196.

Spittle J. A., Brown S. G. R., Intergalva'91 Proceedings of the 3rd International Zinc Coated Sheet Conference, Barcelona, (1991).

Strutzenberger J., Faderl J., “*Solidification and Spangle Formation of Hot-dip Galvanized Zinc Coating*”, Metallurgical and Materials Transactions A, Vol. 29, (1998), 631-639.

Szabo A., Denes E., “*The Effect of the Bath’s Al Content and the Surface Roughness on the Zinc Coatings Properties*”, Materials Science Forum, Vols. 414-415, (2003), 45-50.

Umeda S., “*Continuous Galvanizing Line*”, Hitachi Review, Vol. 24, No. 5, (1975), 233-240.

Vourlias G., Pistofidis N., Stergioudis G., Tsipas D., “*The Effect of Alloying Elements on the Crystallization Behavior and on the Properties of Galvanized Coatings*”, Crystal Research and Technology, Vol. 39, No. 1, (2004), 23-29.

Waitlevertch M. E., Hurwitz J. K., Applied Spectroscopy, Vol. 30, (1976), 510-515.

White D. W. G., Journal Institute of Metals, Vol. 99, (1971), 287.

Yasuda H., Nagira T., Harada H., Sawai T., Sindoh H., Nishimura K., “*Solidification Structure Formation of Zn-Al Alloy in Hot-dip Galvanized Process*”, Galvatech’07 Conference Proceedings, 545-549.

Zapponi M., Quiroga A., Perez T., “*Segregation of Alloying Elements During the Hot-dip Coating Solidification Process*”, Surface and Coatings Technology, Vol. 122, (1999), 18-20.

Zervoudis J., Anderson G., “*A Review of Bath Alloy Additives and Their Impact on the Quality of the Galvanized Coating*”, 6th Asia Pacific General Galvanizing Conference, (2005), 1-17.

Zhang X. G., Goodwin F. E., Galvatech’01 Conference Proceedings, (2001), 311.

APPENDIX A. Detailed Procedure For Metallographic Preparation of Coating

Cross-Sections

(1) Sectioning and Mounting

The HR and BR coated samples were sectioned into 10 mm by 20 mm pieces using a silicon abrasive wheel with a 0.5 mm/s rotation speed. This rotation speed was chosen in order to minimize plastic flow and damage to the coating. Once the samples were cut, all surfaces were painted with the epoxy resin cold mount material. Five of these coated samples were then stacked and secured with a metal screw clamp in order to avoid the penetration of any polishing media or liquids into the spaces between the samples. After completion of the resin curing cycle, the clamp was removed from the stack and the assembly was cold mounted using carbon tape and a plastic clip to hold the samples in the cold mount media such that the RD was parallel to the longitudinal axis of the samples.

(2) Grinding

After the mount cured, the excess epoxy was ground off to expose the sample cross-sections. Grinding was started with 600 grit silicon carbide paper until about 2 mm of the mount was removed to ensure that the damaged zinc layer had been removed. Grinding was continued with 800, 1000 and 1200 grit silicon carbide papers. All silicon carbide papers were covered with a thin layer of paraffin to prevent embedding zinc particles in the paper. The grinding media was continuously flushed with water. Grinding

was performed on a low speed spinning platen to avoid any damage to the coating. For each grade of silicon carbide paper, the mount was rotated 90 degrees and thus, the new scratches were perpendicular to the scratches from last step. Between each grinding step, the sample was swabbed with cotton ball saturated with anhydrous ethyl alcohol to remove any residual material. The sample was then rinsed and ultrasonically cleaned in anhydrous ethyl alcohol for 60 seconds. After drying in a warm air stream, the sample surface was observed using an optical microscope. If all scratches from last step were removed and next scratches were appeared in only one direction, grinding would be continued on the new grade of silicon carbide paper. Final grinding was carried out on 4000 grit silicon carbide paper, flushing using anhydrous ethyl alcohol instead of water.

(3) Polishing

Water was avoided in all polishing steps. Polishing was conducted on a spinning platen using MD-MOL cloths using 9, 6, 3 and 1 micron diamond pastes. Anhydrous ethyl alcohol was used as a lubricant. Each polishing step was performed for 60 seconds. Between each step, the sample was flushed with anhydrous ethyl alcohol, ultrasonically cleaned in anhydrous ethyl alcohol for 30 seconds and dried by a warm air stream. The surface was inspected under the light optical microscope to ensure that all scratches from the previous polishing step were removed. Final polishing was carried out on a MD-MOL cloth charged with a 0.05 micron alumina slurry diluted with anhydrous ethyl alcohol.

(4) Etching

Samples were etched using a mixture of 6 g picric acid + 100 mL ethanol + 5 mL acetic acid + 10 mL water. The etchant was made prior to polishing so that the polished sample could be etched immediately after final polishing. Two to three drops of the etchant were placed on the polished surface for 5 seconds. The surface was then rinsed and ultrasonically cleaned using anhydrous ethyl alcohol. The sample was dried in a warm air stream and checked under the optical microscope, where the etching and inspection steps were repeated until the grain boundaries in the zinc overlay were visible.